Effect of W/C Ratio and Replacement Materials on Fracture Behavior of Concrete - Via Computed Tomography Method

Hamed Rajabpour

Submitted to the
Institute of Graduate Studies and Research
in partial fulfillment of the requirements for the Degree of

Master of Science
in
Civil Engineering

Eastern Mediterranean University
March 2015
Gazimağusa, North Cyprus

Approval of the Institute of Graduate Studies and Research

Prof. Dr. Serhan Çiftçioğlu
Acting Director

I certify that this thesis satisfies the requirements as a thesis for the degree of Master of Science in Civil Engineering.

Prof. Dr. Özgür Eren
Chair, Department of Civil Engineering

We certify that we have read this thesis and that in our opinion it is fully adequate in scope and quality as a thesis for the degree of Master of Science in Civil Engineering.

Asst. Prof. Dr. Tülin Akçaoğlu
Supervisor

Examining Committee

---

1. Prof. Dr. Özgür Eren ____________________

2. Asst. Prof. Dr. Tülin Akçaoğlu ____________________

3. Asst. Prof. Dr. Serhan Şensoy ____________________

ABSTRACT

Nowadays, with the advancements in all fields of science and technology, use new numerical and experimental methods are made possible in the construction industry. X-rays and CT (Computed Tomography) scans are two of the direct methods developed to evaluate the microcracking behavior of concrete.

The aim of this study was to evaluate the effect of water/cement ratio and mineral admixtures on microcracking behavior of concrete. For this purpose, total of 12 specimens were produced using three different w/c ratios and four different admixtures. To be able to determine the effects of these differences on both compressive strength and microcracking behavior, first the specimens were subjected to compressive stress loading and then to CT (Computed Tomography) scans to obtain 2D and 3D images. CT (Computed Tomography) scans were taken for different loading levels corresponding the ultimate strength.

It was found that out of all specimens, the one containing metakaolin admixture with low w/c ratio has a considerable influence on the microcracking behavior of concrete under compressive stress loading. Although the crack rate of propagation is slow up to 80% of the ultimate stress, cracking accelerates after 80% of loading of metakaolin specimens.

Keywords: Computed Tomography Method, Cracks propagation, Concrete cores, Compressive strength, Polypropylene, Metakaolin, Silica fume.

ÖZ

Günümüzde, bilim ve teknolojinin tüm alanlarındaki gelişmeler, inşaat endüstrisinde, yeni numerik ve deneysel metotların kullanımını mümkün kılmaktadır. X-ray ve tomografi metotları beton içerisindeki çatlak oluşum ve ilerlemesini direk inceleyip tanımlamak için günümüzde kullanılan en uygun metotlar arasındandır.

Bu çalışmanın amacı, su/çimento oranı ve de mineral katkıların basınç dayanımı, çatlak oluşumu ve ilerlemesi üzerindeki etkilerini araştırmaktır. Bu amaç için toplam 12 değişğik karışım hazırlanıp numunelerin, basınç dayanım, çatlak oluşum ve ilerleme davranışları incelenmiştir. Farklı su/çimento oranı ve katkıların etkilerinin araştırılması için, numuneler önce basınç dayanımına tabi tutulmuş daha sonra basınç dayanımına bağlı olarak farklı yükleme seviyelerinde çatlaklar incelenmiştir.

Bütün numuneler incelendiğinde metakaolin içeren numunelerin düşük su/çimento oranında çatlak oluşum ve ilerlemesi üzerinde hayli etkili olduğu anlaşılmıştır. Metakolin içeren numunelerde, çatlak ilerlemesi %80 yükleme seviyesine kadar yavaş ilerlese de bu seviyeden sonar ivme kazanmaktadır.

Anahtar Kelimeler: Tomografi Metot, Çatlak oluşumu ve ilerlemesi, Basınç Dayanımı, Mineral Katkı, Su/ Çimento oranı, Silis Dumanı, Polipropolen, Metakolin.

DEDICATION

To my spiritual father

SÜLEYMAN LEVENTOĞLU

My symbol of strength

Who offered me full support throughout these past 3 years.

ACKNOWLEDGMENT

I would like to express my gratitude to my supervisor Assistant Professor Dr. Tulin Akcaoglu for her useful comments, remarks and engagement through the learning process of this master thesis. Furthermore I would like to thank Professor Dr. Ozgur Eren, Chair of the Civil Engineering Department at the Eastern Mediterranean University for his effective and powerful role on corrections and Re-writing of this thesis. He kindly spends his time and helped me step by steps during writing of this thesis. Last by not least, I would like to give special thanks to Assistant Professor Dr. Serhan Sensoy for his continuous support and friendship throughout my master's program and thesis writing process.

TABLE OF CONTENTS

LIST OF TABLES

LIST OF FIGURES

Chapter 1

INTRODUCTION

1.1 General

In general, mechanical behavior of concrete is analysed considering the effect of initial cracks on microcracking behavior of concrete. It is well known that hydration shrinkage cracks have a great influence on microcracking behavior of concrete particularly after a critical stress level of loading [1,2].

In most cases cracks occur in concrete. The causes of crack formation can be identified by making an analysis. Extensive studies on microcracking concluded that concrete cracks can be attributed to the following reasons [3]:

1. Construction and supervision mistakes - approximately 36%.
2. Design flaws - approximately 27%.
3. Ambient conditions (temperature, humidity, etc.) - approximately 21%.
4. Quality of materials - approximately 17%.

In addition, all cracks can be grouped into two major groups:

1. Cracks occurring before and during hardening.
2. Cracks occurring after hardening of concrete.

There are many types of concrete, designed to suit a variety of purposes coupled with a range of compositions, finishes and performance characteristics. Properly proportioned concrete mix should possess these qualities [4, 5]:

1. Acceptable workability of the freshly mixed concrete.
2. Durability, strength, and uniform appearance of the hardened concrete.
3. Economy.

1.2 Objectives of this study

The objectives of this experimental work are as follows:

1. Investigation and evaluation of fracture behavior of concrete by means of computed tomography method.
2. Evaluation of the effect of w/c ratio both on concrete compressive strength and microcracking behavior before and after hardening of concrete and/or before and after loading the concrete.
3. Determining the effect of w/c ratio on the amount of air voids in hardened concrete.
4. Identifying the effects of mineral admixtures (polypropylene, silica fume and metakaolin) both on concrete compressive strength and microcracking behavior.

1.3 Works Done

The following experiments were performed to be able to achieve our objectives.

1. Effects of three different water/cement ratios (0.55, 0.45, and 0.35) with three different additives of different ratio specimens on compressive strength and microcracking behavior of concrete were investigated by using compressive strength test.
2. Effects of 10% of silica fume as replacement material with 3 different water/cement ratios (0.55, 0.45, and 0.35) on compressive strength and microcracking behavior of concrete were investigated by both CT method and compressive strength test.

3. Effects of 10% of metakaolin as replacement material with 3 different water/cement ratios (0.55, 0.45, and 0.35) on compressive strength and microcracking behavior of concrete were investigated investigated by both CT method and compressive strength test.
4. Effects of 1.7 kg/m³ of polypropylene fiber as additive material with 3 different water/cement ratios (0.55, 0.45, and 0.35) on compressive strength and microcracking behavior of concrete were tested by both CT method and compressive strength test.
5. Internal cracks under different loading levels (50%, 65% and 80% of ultimate strength) were investigated by means of computed tomography method for all specimens. This was done by using the pictorial representation of the internal cross-section of the specimen.
6. After CT method, for each specimen, using AutoCAD, the perimeter and area sizes were calculated and the location of each crack was determined.

1.5 Guide to Thesis

Chapter 2 is the literature review which looked into numerous previous experiments on concrete deterioration under compressive loading and propagation model of inner cracks. Chapter also explains the importance of using computed tomography method in construction industry and provides examples on successful studies on scanning and imaging of concrete samples.

Chapter 3 describes the methodology of the experiments, and the characteristics of the materials used. In chapter 4 the experimental outcomes were presented and discussed in great detail and finally chapter 5 outlines the conclusion of the experiment and suggests further recommendations.

Chapter 2

LITERATURE REVIEW

2.1 Introduction

Hydration shrinkage cracks have a great influence on microcracking behavior and therefore durability of concrete structures. The change in volume due to shrinkage, results in cracks which are called as initial defects and they exist prior to loading of the material. It is known that the density and location of these initial defects have a considerable influence on microcracking behavior of concrete, particularly after the critical stress level.

Distributions of cracks affect concrete damages. Behavior of concrete specimens under unconfined compressive loading is associated with the generation of microcracks. These kinds of microcracks gradually accumulate until final fracture, which severely reduces the load-bearing capacity [7].

2.2 Microcracking of Concrete Structures under Compressive Loading

Concrete is a heterogeneous material with pores and voids of various sizes and cracks. A number of flaws or crack-like voids can exist in concrete even prior to loading. Most of these initial defects are interfacial cracks and other critical fracture process zones.

Some of these interfacial cracks are caused by the settlement of coarse aggregates during the concrete casting process and bleeding. Water accumulates on the undersides of the aggregate particles, forming a gap, or at least a partial loss of bond, between the mortar and the aggregate which makes it one of weakest zones in concrete. As a result, physical and mechanical properties are not identical at each point within a concrete. As it is concluded in [8], shrinkage of mortar during hardening results in bond cracks at the mortar-aggregate interface. When concrete is subjected to mechanical loading, micro-cracks are generally initiated from these weak zones.

2.2.1 Fracture Mechanics under Load

There is extensive literature on studies investigating the concrete behavior under axial compressive loading. It is found that the fracture process of concrete can be characterized as strain softening and fracture toughening due to the formation and branching of micro-cracks [9, 10, 11, 12 and 13]. Some physical observations can be summarized as the follows:

- Micro-cracking initiates at the weakest point, where the tensile stress concentration is the highest, and it will propagate and may interlock as load increases. However aggregates act like barriers to those propagating microcracks. With increasing stress, propagating cracks increase in width and length and combine to form macro-cracks. After load reaches the critical stress level, those macrocracks show accelerated propagation which cause failure of the concrete structure. [10].

- As discussed in [11], crack deflections occur when the path of the least resistance is around a relatively strong particle or along a weak interface. Grain bridging occurs when the crack has advanced beyond an aggregate that continues to transmit stresses across the cracks, until it ruptures which causes energy dissipation through. Another mechanism in the fracture process is crack-branching. The crack may propagate into several branches due to heterogeneity of concrete. More energy should be consumed to form new crack branches.

- Generally, the crack surface is tortuous due to the toughening mechanism, in which crack generally branches around aggregates, causing random propagation in concrete. The roughness of the crack surface depends on the toughness and the size of the aggregates and the properties of the matrix and interface.

Under compressive load, two types of cracks may occur; simple bond cracks and combined cracks as shown in Figure 2.1. Simple bond cracks refer to cracking at mortar-aggregate interface. These cracks occur at the early stage of loading as a result of debonding, and they are isolated and stable under constant load. As the load increases, cracks may initiate and propagate within mortar, and eventually connect to the bond cracks, forming combined cracks. Combined cracks can be grouped as Type I and Type II [14], where Type I cracks consist of one bond crack and a mortar crack, or the combination of two bond cracks connected by a mortar crack. These types of cracks extend in a relatively stable manner, which means that if the applied load is held constant, crack propagating slows down. Type II cracks contain two bond cracks and two mortar cracks. These types of cracks propagate spontaneously even under constant load, leading to failure.

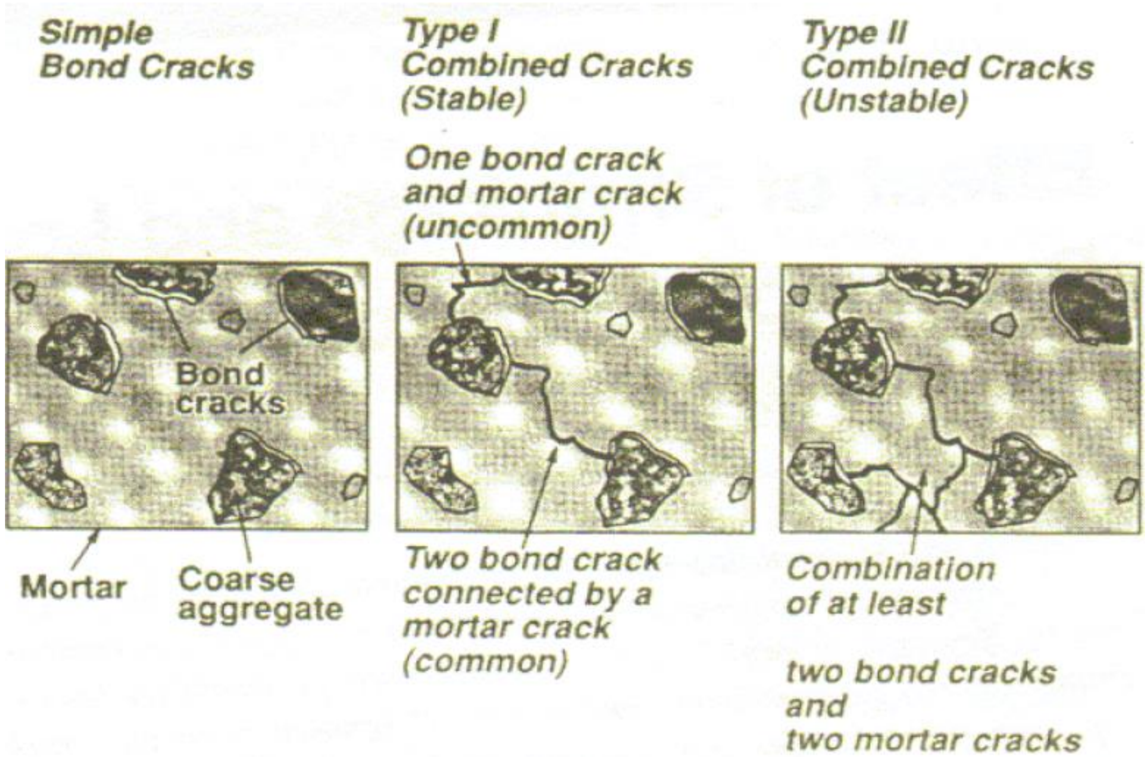

Figure 2.1. Types of cracks under compressive loading [14].

2.2.1.1 Microcracking of Concrete under Compressive Loading

Microcracks created by compressive loading are varied in shape and length. This is due to the heterogeneity of the material. Under a microscope, it is observed that when compressive stress increases up to 85% of the ultimate stress, micro cracks primarily occur at the interface between the coarse aggregates and the mortar and are uniformly distributed in both transversal and longitudinal directions [15]. When stress reaches 95% of the ultimate stress, bond cracks are connected by cracks through the mortar and combined cracks propagate parallel to the loading direction. In another research [16], similarly, microcracking behavior under compressive loading is defined as, in bond cracks at the interface between the coarse aggregates and the paste increases at 30% of the ultimate load, and mortar cracks initiate at the stress level between 70 to 90 percent of the ultimate stress.

In another similar study, micro-cracks at coarse aggregate and paste interfaces initiate at 30% of the ultimate stress level. When stress increases from 30% to 50%, micro-cracks propagate around the interfaces, which are simple cracks on the order of 0.1mm in length. Between 50% and 70% stress levels, they extend to the paste where they remain very short with some branches. Above 70% stress level, new micro-cracks start initiating around fine aggregates and connect with the previous microcracks, leading to the failure of specimens.

2.3 Direct Detection of Microcracks - Computed Tomography Method

Computer Tomography (CT), also known as Computerized Radioactive Tomography, is the sectional imaging method used in construction to process cross-sectional images of critical points of concrete specimens. In other words, scans provide pictorial section of the inner part of the objects. Mathematical formulation of CT was performed by Radon in 1917. The first use of a CT scanner was after the invention of the X-ray by Hounsfield as a diagnostic tool in medicine in 1972. A schematic figure of scanning samples is shown below [Figure 2.2].

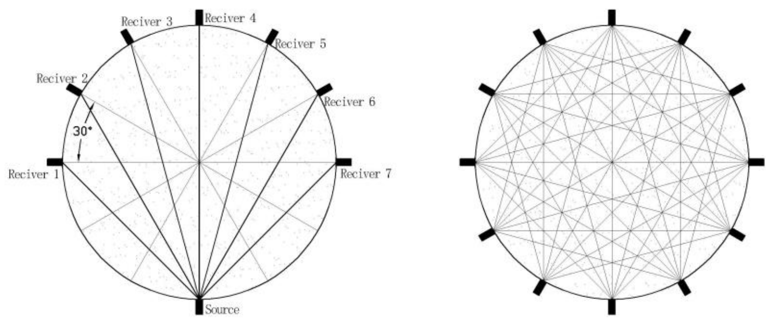

Figure 2.2. Schematic figure of scanning samples.

Computerized tomography is capable of producing highly accurate images at millimeter or sub-millimeter resolution. However, application of computerized tomography to concrete is generally limited to laboratory studies since the scanners are expensive, measurements take a long time and due to limitations such as use of only small specimen sizes, and restrained accessibility to both sides of the object. Image reconstruction from limited views has been the subject of several studies but further research is needed before the technique can be applied in the construction field.

The imaging of engineering systems using non-destructive evaluation techniques is becoming more popular, not only in the scientific community but also in their engineering applications. Techniques such as X-ray, tomography, electromagnetic methods, electrical resistivity tomography and sonic and ultrasonic-based testing are being used to locate defects, monitor processes and to estimate engineering properties of structural and geotechnical engineering systems [42, 43, 44, 45, 46, 47, and 48]. 3D Micro Computed Tomography is a novel nondestructive method to analyze spatial changes of microstructures in different cementitious building materials [49].

These types of techniques are very promising, as they may change the way we obtain design parameters for engineering purposes. Researchers in civil engineering have been widely using these methods to identify the characteristics of cement paste and concrete, asphalt concrete, soil-water systems, rock, and reinforced concrete structures [18, 19, 20, 21, 22, 23, 24 and 25].

2.4 Properties and Effects of Mineral Additives

2.4.1 Polypropylene Fiber

According to ACI 544 IR.82 [26], fiber reinforced concrete is defined as concrete made with hydraulic cement, containing fine or fine and coarse aggregate and discontinues discrete fiber that also containing pozzolans and additives. The fibers can be made from natural materials (e.g. asbestos, sisal, cellulose) or can be manufactured products such as glass, steel carbon and polymer [27].

Fibers act as crack arrestors that can restrict the development of cracks, therefore transforming an inherently brittle matrix (i.e. Portland cement) with its low tensile and impact resistances, to a strong composite with superior crack resistance, improved ductility and distinctive post cracking behavior prior to failure [28].

2.4.1.1 Types of Polypropylene Fibers

Polypropylene is a synthetic hydrocarbon polymer material, first introduced in 1957[29]. It is among synthetic, polymeric fibers, (including but not limited to nylon, polyester, and polyethylene) that are adapted from the textile industry, and when added to PCC, it is known to improve performance. Currently polypropylene is the most widely used synthetic fiber for paving applications [30] and is available in two forms: monofilament fibers and film fibers.

2.4.1.2 Physical Properties

Polypropylene has a melting point of 165 degrees Celsius and can withstand temperatures over 100 degrees Celsius for short periods of time before softening. It is chemically inert and any chemical that can harm these fibers will probably be much more detrimental to the concrete matrix. The fiber is susceptible to degradation by UV radiation (sunlight) and oxygen; however, in the concrete matrix this problem is eliminated. Monofilament fibers were the first type of polypropylene fiber introduced as an additive in PFRC (Polypropylene Fiber Reinforced Concrete) and are available in 6, 12 and 19 mm lengths (Figure 2.3).

Figure 2.3. Polypropylene Fiber

Table 2.1. Typical properties of fiber [27]

Type of Fiber	Specific Gravity	Tensile strength MPa	Tensile strength Psi	Modulus of elasticity Gpa	Modulus of elasticity 10^6 Psi	Elongation at failure , Percent	Poisson ratio
Crysotile Asbestos	2.55	3.0 to 4.5	435 to 650	164	23.8	3.0	0.30
Alkali-resistance glass	2.71	2.0 to 2.8	290 to 410	80	11.6	2.0 to 3.0	0.22
Fibrillated polypropylene	0.91	0.65	95	8	1.2	8.0	0.29 to 0.46
Steel	7.84	1.0 to 3.2	145 to 465	200	29.0	3.0 to 4.0	0.30
Carbon	1.74 – 1.99	1.4 to 3.2	200 to 465	250 to 450	36.2 to 65.3	0.4 to 1.0	0.2 to 0.4
Kevlar	1.45	3.6	520	65 to 130	94.3 to 18.8	2.0 to 4.0	0.32

2.4.2 Silica Fume

Silica fume, also known as micro silica, is a byproduct of the reduction of high-purity quartz with coal in electric furnaces in the production of silicon and ferrosilicon alloys. Because of its extreme fineness and high silica content, Silica Fume is a highly effective pozzolanic material and affects various concrete properties such as compressive strength, bond strength and water absorption resistance with reducing permeability (helps in protecting reinforcing steel from corrosion) [31].

2.4.2.1 Physical Properties of Silica Fume

Silica fume is either premium white or grey in color and (Figure 2.4) it's particles are extremely small, with more than 95% of the particles finer than 1 μm. Typical physical properties of silica fume are given in Table 2.2 [32].

Table 2.2. Typical physical properties of silica fume [32].

Property	Value
Particle size (typical)	< 1 μm
Bulk density	
As-produced	130 - 430 kg/m³
Slurry	1,320 - 1,440 kg/m³
Densified	480 - 720 kg/m³
Specific gravity	2.22
Surface area (BET)	13,000 - 30,000 m²/kg

Figure 2.4. Silica fume

2.4.2.2 Chemical Composition of Silica Fume

Silica fume is composed primarily of pure silica in non-crystalline form. X-ray diffraction analysis of different silica fumes reveals that the material is essentially vitreous silica, mainly of cristobalite form. Silica fume has a very high content of amorphous silicon dioxide and consists of very fine spherical particles. Silica fume generally contains more than 90% SiO_2 and small amounts of iron, magnesium, and alkali oxides are also found. Oxides analyses of silica fume as reported by various researchers are given in Table 2.3.

Table 2.3. Chemical composition of silica fume samples

Oxides	Sandvik and Gjorv [33]	Hooton and Titherington [34]	Yazici [35]
SiO2	92.1	96.65	92.26
Al2O3	0.5	0.23	0.89
Fe2O3	1.4	0.07	1.97
CaO	0.5	0.31	0.49
MgO	0.3	0.04	0.96
K2O	0.7	0.56	1.31
Na2O	0.3	0.15	0.42
SO3	–	0.17	0.33
LOI	2.8	2.27	–

2.4.3 Metakaolin

Kaolin is one of the most abundant natural clay minerals, and metakaolin is produced by heating kaolin to 650-900°C. This heat treatment or calcination is used to break down the structure of kaolin. Bound hydroxyl ions are removed and resulting disorder among alumina and silica layers yields a highly reactive, amorphous material with pozzolanic and latent hydraulic reactivity, suitable for use in cementing applications [36, 37].

Metakaolin can be used as a partial replacement for Portland cement and may improve both the mechanical properties and the durability of concrete. In general, metakaolin offers a set of advantages similar to those imparted by silica fume, including comparable strengths, permeability, chemical resistance, and drying shrinkage resistance. It also contributes to higher compaction, which increases flow ability of mastic cement, enhances mechanical bond and improves adhesion between the cement paste and aggregates [40].

Addition of metakaolin decreases workability of fresh concrete mix however this side effect can be reduced by using superplasticizers whose types have an influence on rheological properties of fresh concrete mix. Generally, polycarboxylate based superplasticizers gives better workability than poly naphthalene/melamine sulfonates. Addition of flyash can also adjust the low workability caused by metakaolin.

2.4.3.1 Physical Properties of Metakaolin

Metakaolin particles measure approximately one-half to five micrometers, placing them above cement grains and below silica fume particles when categorized by size.

Metakaolin is white in color (Figure 2.5) which makes it particularly attractive for color matching and other architectural applications. For these reasons, metakaolin is increasingly used in the production of high-performance concrete [38, 39].

Table 2.4. Typical physical properties of metakaolin [41]

Property	Value
Particle size (typical)	< 2.54 μm
Bulk density	800 - 880 kg/m³
Specific gravity	2.5
Surface area (BET)	150000-180000 m²/kg

Figure 2.5. Metakaolin.

2.4.3.2 Chemical Composition of Metakaolin

Chemical properties of metakaolin are presented in Table 2.5.

Table 2.5. Chemical composition of silica fume samples [40]

Oxides	(%)
SiO2	60 – 65
Al2O3	30 – 34
Fe2O3	1.00
CaO	63.61
MgO	4.56
K2O	0.51
Na2O	0.08

Chapter 3

EXPERIMENTAL WORK

3.1 Introduction

In this thesis, the effect of water/cement ratio and mineral admixtures on microcracking behavior of concrete was studied. For this purpose, total of 12 specimens were produced using three different w/c ratios and three different admixtures. To be able to determine the effects of these differences on both compressive strength and microcracking behavior, first the specimens were subjected to compressive stress loading and then to CT (Computed Tomography) scans to obtain 2D and 3D images. CT scans were taken for different loading levels corresponding the ultimate strength. Figure 3.1 demonstrates CT picturing instrument and the specimen.

Figure 3.1. CT picturing instrument and the specimen.

3.2 Materials Used

3.2.1 Aggregates

A mixture of fine and coarse aggregates with maximum diameter size of 25mm was used after being washed twice. Natural aggregates were provided from Marand Kizil Kum standard sand mine. Sieve analysis showed that, all aggregates satisfied the ASTM C33 standards and were within specified limits. Table 3.1 represents the grading requirements for coarse aggregates. Physical and mechanical properties of the aggregates and grading curves are specified in Table 3.2 and Figure 3.2, respectively.

Table 3.1. ASTM C 33 , Grading Requirements for Coarse Aggregates.

Size Number	Nominal Size (Sieves with Square Openings)	Amounts Finer than Each Laboratory Sieve (Square-Openings), Mass Percent													
		100 mm (4 in.)	90 mm (3 1/2 in.)	75 mm (3 in.)	63 mm (2 1/2 in.)	50 mm (2 in.)	37.5 mm (1 1/2 in.)	25.0 mm (1 in.)	19.0 mm (3/4 in.)	12.5 mm (1/2 in.)	9.5 mm (3/8 in.)	4.75 mm (No. 4)	2.36 mm (No. 8)	1.18 mm (No. 16)	300 μm (No.50)
1	90 to 37.5 mm (3 1/2 to 1 1/2 in.)	100	90 to 100	...	25 to 60	...	0 to 15	...	0 to 5	...	...	...	...	...	...
2	63 to 37.5 mm (2 1/2 to 1 1/2 in.)	...	...	100	90 to 100	35 to 70	0 to 15	...	0 to 5	...	...	...	...	...	...
3	50 to 25.0 mm (2 to 1 in.)	...	...	...	100	90 to 100	35 to 70	0 to 15	...	0 to 5	...	...	...	...	...
357	50 to 4.75 mm (2 in. to No. 4)	...	...	...	100	95 to 100	...	35 to 70	...	10 to 30	...	0 to 5	...	...	...
4	37.5 to 19.0 mm (1 1/2 to 3/4 in.)	...	...	...	...	100	90 to 100	20 to 55	0 to 15	...	0 to 5	...	...	...	...
467	37.5 to 4.75 mm (1 1/2 in. to No. 4)	...	...	...	...	100	95 to 100	...	35 to 70	...	10 to 30	0 to 5	...	...	...
5	25.0 to 12.5 mm (1 to 1/2 in.)	...	...	...	...	...	100	90 to 100	20 to 55	0 to 10	0 to 5	...	...	...	...
56	25.0 to 9.5 mm (1 to 3/8 in.)	...	...	...	...	...	100	90 to 100	40 to 85	10 to 40	0 to 15	0 to 5	...	...	...
57	25.0 to 4.75 mm (1 in. to No. 4)	...	...	...	...	...	100	95 to 100	...	25 to 60	...	0 to 10	0 to 5	...	...
6	19.0 to 9.5 mm (3/4 to 3/8 in.)	...	...	...	...	...	...	100	90 to 100	20 to 55	0 to 15	0 to 5	...	...	...
67	19.0 to 4.75 mm (3/4 in. to No. 4)	...	...	...	...	...	...	100	90 to 100	...	20 to 55	0 to 10	0 to 5	...	...
7	12.5 to 4.75 mm (1/2 in. to No. 4)	...	...	...	...	...	...	...	100	90 to 100	40 to 70	0 to 15	0 to 5	...	...
8	9.5 to 2.36 mm (3/8 in. to No. 8)	...	...	...	...	...	...	...	...	100	85 to 100	10 to 30	0 to 10	0 to 5	...
89	9.5 to 1.18 mm (3/8 in. to No. 16)	...	...	...	...	...	...	...	...	100	90 to 100	20 to 55	5 to 30	0 to 10	0 to 5
9[A]	4.75 to 1.18 mm (No. 4 to No. 16)	...	...	...	...	...	...	...	...	...	100	85 to 100	10 to 40	0 to 10	0 to 5

[A] Size number 9 aggregate is defined in Terminology C125 as a fine aggregate. It is included as a coarse aggregate when it is combined with a size number 8 material to create a size number 89, which is a coarse aggregate as defined by Terminology C125.

Table 3.2. Properties of fine and coarse aggregate

Property of Aggregate	Fine (g/cm³)	Coarse (g/cm³)
Relative Density(SSD)	2.66	2.68
Absorption(% of dry mass)	2.56	1.2

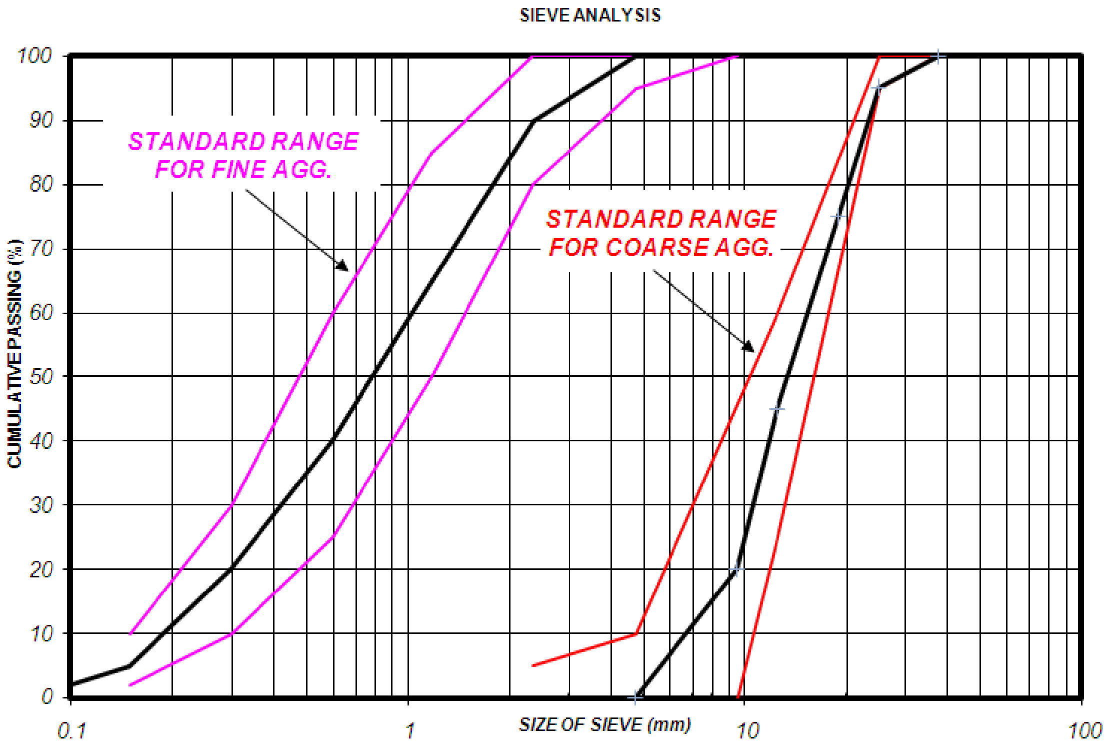

Figure 3.2. Grading results of coarse and fine aggregates.

3.2.2 Cement

Type II Portland cement (PC) obtained from Soufian Cement Co. was used in this experimental work. It’s chemical and physical properties are listed in Table 3.3.

Table 3.3. Chemical and Physical Properties of Cement Used

Chemical Composition		Physical Properties	
K_2O	0.75	Fineness-Blaine(cm²/gr)	2900
SiO_2	20.03		
Al_2O_3	4.53		
Fe_2O_3	3.63		
CaO	60.25	Setting time (minutes)	
MgO	3.42	Initial	145
SO_3	2.23	Final	210
Na_2O	0.25		
C_2S	23.5	Compressive strength (MPa)	
C_3S	49. 9	3 Days	180
C_3A	6.6	7 Days	290
C_4AF	10/9	28 Days	410

3.2.3 Water

Drinkable water was used for all concrete mixtures and for the curing process.

3.2.4 Superplasticizer

The superplasticizer was obtained from Vand Constuction Chemicals Co. was used in the concrete mixed.

Properties of the used superplasticizer are as follows:

- Form: liquid
- Color: brown
- Density: 1.03 Kg/Lt
- Dosage range 0.2 to 1.2 %
- pH: 7
- Shelf life: 2 year

In this experimental work, for mixtures with 0.55 w/c ratio, the amount of superplasticizers was 0.2% of the cement amount in control specimens. For 0.45 w/c ratio it was the 0.7% of the cement and for 0.35 W/C ratio, it was 1.2% of the cement amount.

3.2.5 Metakaolin

Metakaolin used in this experimental work was obtained from Maryland China Clay Co. and it was used as a replacement material. The amount was 10% of the cement weight in each specimen.

3.2.6 Silica Fume

Similar to Metakaolin, silica fume was also used at 10% of cement weight as a replacement material. The product was produced by Vand Construction Chemicals Co.

3.2.7 Polypropylene Fibers

1.7 kg/m³ Polypropylene fibers of 12mm length were used as additives, (Figure 3.3), supplied from Vand Construction Chemicals Co. This kind of fiber is effective in prevention of thermal cracking, shrinkage and enhanced compressive strength.

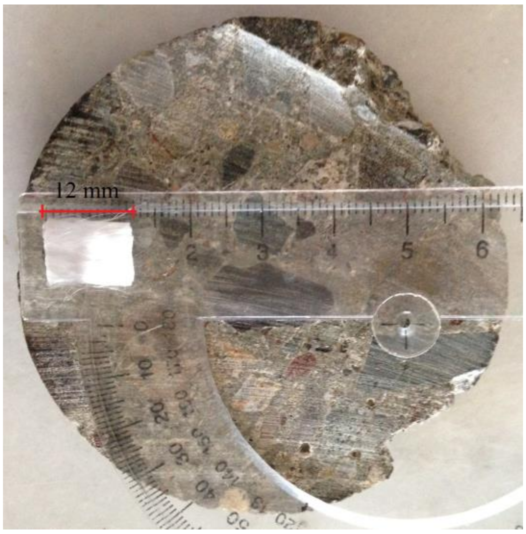

Figure 3.3. Polypropylene fibers, with 12 mm length.

3.3 Methodology

In this section, twelve different mix designs were performed, considering three different w/c ratios and four different admixtures.

3.3.1 Mix Design Proportions

Mix design proportioning was performed by using weight-batching method. Twelve types of different concrete mix designs according to Table 3.4 were used in this experimental work.

Table 3.4. Proportioning of concrete mix design for 1 m^3

Samples	W/C Ratio	Super Plasticizer (Kg)	Cement (Kg)	Coarse Agg (Kg)	Fine Agg (Kg)	Silica Fume (Kg)	Meta Kaolin (kg)	Poly Propylene (Kg)
A-Control	0.55	0.60	300	970	1050	-	-	-
B	0.55	0.60	270	970	1050	30	-	-
C	0.55	0.60	270	970	1050	-	30	-
D	0.55	0.60	300	970	1050	-	-	1.7
E-Control	0.45	2.10	300	970	1050	-	-	-
F	0.45	2.10	270	970	1050	30	-	-
G	0.45	2.10	270	970	1050	-	30	-
H	0.45	2.10	300	970	1050	-	-	1.7
I-Control	0.35	3.60	300	970	1050	-	-	-
J	0.35	3.60	270	970	1050	30	-	-
K	0.35	3.60	270	970	1050	-	30	-
L	0.35	3.60	300	970	1050	-	-	1.7

3.3.2 Mixing, Compacting and Curing of Concrete Specimens

All concrete mixtures were mixed in a 0.25 m^3 capacity mixer. The materials were added in the following order: coarse aggregates, fine aggregates, and cement-additive mixture or replacement materials. These were mixed for 30 seconds, and then water and superplasticizer were added and mixed for another 150 seconds, reaching a total mixture time of 3 minutes.

12 wooden (50*50*50) cm molds were used for molding of different concrete mixtures (Figure 3.4). The slump of concrete mixtures determined using Abrams cone, following ASTM C143 standards. The size of specimens (50*50*50) cm allowed the use of a vibrator for compaction during molding (Figure 3.5)

After molding, the specimens were covered with plastic sheet for 24 hours to prevent evaporation of water from the surface. Then, for the next 28 days, each specimen was sprayed with drinkable water and covered again with the plastic sheet.

Figure 3.4. (50*50*50) cm wooden molds.

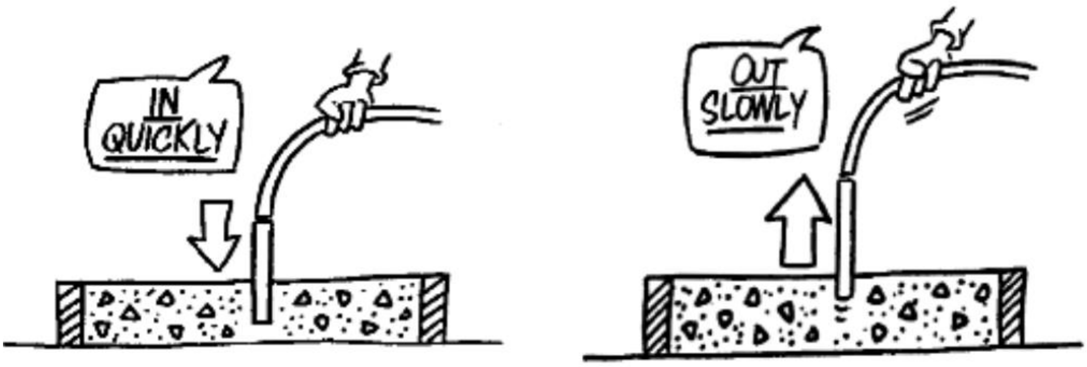

Figure 3.5. Vibration model of concrete.

3.3.3 Core Sampling and Preparation for Testing

7.5 cm cylinder cores were taken with core drilling machine, perpendicular to the surface, from the middle of hardened concrete after 28 days of curing under site conditions according to ASTM C42 standards (Figure 3.6). Upon taking out of the cores, both sides of the samples were cut with cutting machine to obtain length/ diameter ratio of 2, According ASTM C42/C42M –13 (Figure 3.7).Then, capping was performed with sulfur mortar in 130°C temperature, following ASTM C617 (Figure 3.8).

Figure 3.6. Drilling method of (50*50*50) cm specimens.

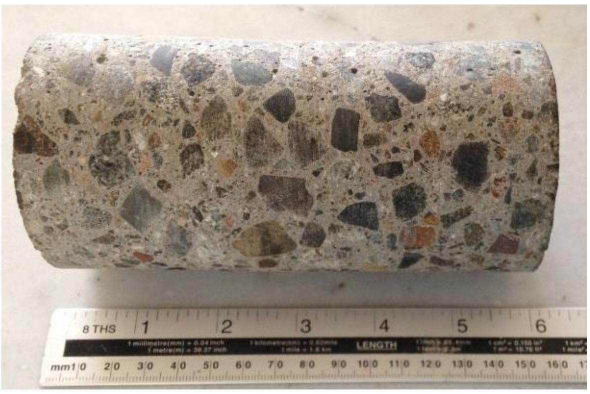

Figure 3.7. 7.5 cm concrete cylinder cores.

Figure 3.8. Capping of cylinder cores.

3.3.4 Compressive Strength and Computed Tomography Tests

Following the ASTM C39 regulations, compressive strength of 28-day-old cylinder cores were, at a loading rate of 2.46 kg/cm² per second. The testing machine is shown in Figure 3.9.

Prior to scanning, all samples were dried and labelled according to their w/c ratio and admixtures. Samples underwent high-resolution 2D and 3D CT Scanning at Marand Medical Imaging Centre. Settings used for helical CT scan was according Table 3.5.

Schematic view of concrete core scanning is shown in Figure 3.10.

Figure 3.9. Compressive strength testing machine.

Table 3.5. Setting used for helical CT scan

Helical pitch	15.0
Slice thickness	1.0 mm
Speed	7.5 mm/rotation
Exposure	120 Kw and 250 mA
Recon matrix	512*512
Field of view	100-200 mm

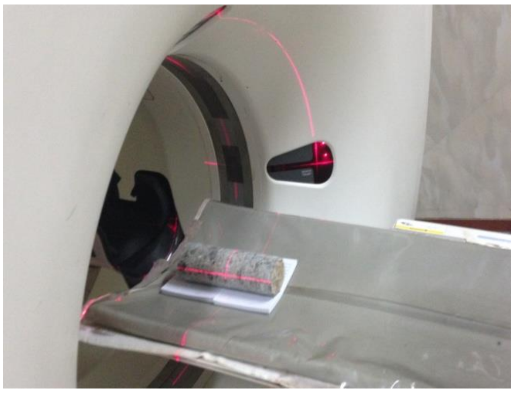

Figure 3.10. Schematic view of concrete core scanning.

Schematic model of sectional images obtained from scanning of concrete cores are shown in Figure 3.11.

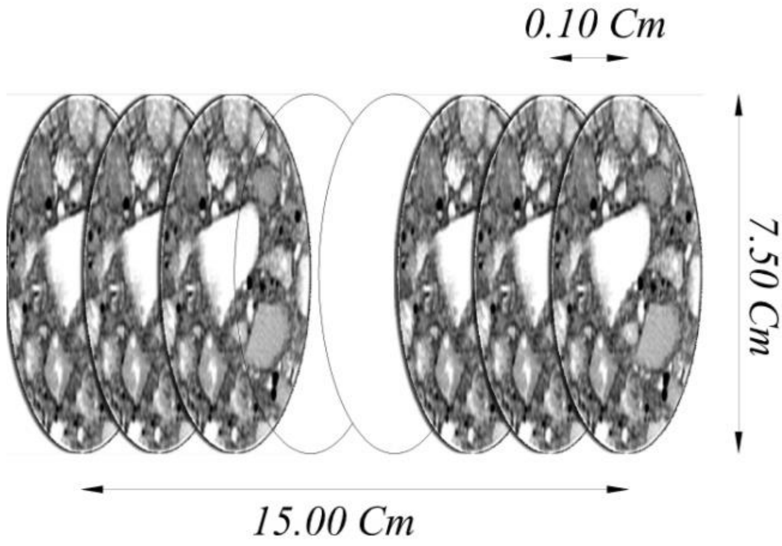

Figure 3.11. Sectional images of concrete core specimen.

Chapter 4

RESULTS AND DISCUSSIONS

4.1 Introduction

In this chapter, the results of all performed experiments are plotted in table, chart of figure format. The data from AutoCAD in measuring the sizes and the locations of the cracks in 12 mixes made from 3 various w/c ratios and three different admixtures are given in Appendix A, but the related graphs are shown and discussed in this chapter. The effects of these variations are discussed according to the obtained compressive strength graphs and Computed Tomography results from 2D and 3D imaging.

4.2 Compressive Strength Test Results

28-day Compressive strength test results of twelve different concrete core samples produced by using three different admixtures and w/c are presented in Figure 4.1.

1. As shown in Figure 4.1, for all w/c ratios, the compressive strength of the mixes with replacements and admixtures were slightly higher than that of the control specimen.
2. The positive effect of metakaolin was found to increase with decreasing w/c ratio. Although same conclusion can be made for all three admixtures, the highest rate of increase in strength was in Metakaolin and the polypropylene had the lowest increment rate.

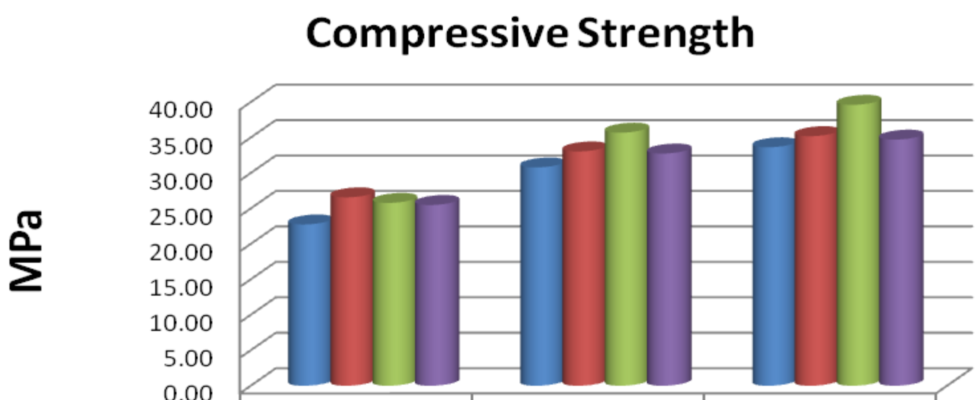

	0.55 Water/ Cement Ratio	0.45 Water/ Cement Ratio	0.35 Water/ Cement Ratio
Control Concrete	22.75	30.79	33.64
Slica Fume	26.58	33.05	35.21
Meta kaolin	25.79	35.70	39.62
Poly Propilen	25.50	32.75	34.72

Figure 4.1. 28-days Compressive Strength Test Results of 12 Different Mixes.

3. When the w/c ratios are considered separately, 0.55 ratio stands out in terms of the additive-strength relationship. While in 0.45 and 0.35 w/c ratios the strength increases with the order of silica fume, polypropylene and metakaolin added mixtures, this order changes to metakaolin, polypropylene and silica fume in 0.55 w/c ratio specimens.

4.3 Effect of W/C Ratio on Compressive Strength

In figure 4.2, it is shown more clearly that the specimens without any admixtures have the lowest compressive strength, and that the strength and water/cement ratio are inversely proportional. Compressive strength showed sharp increment for low w/c ratio metakaolin specimens.

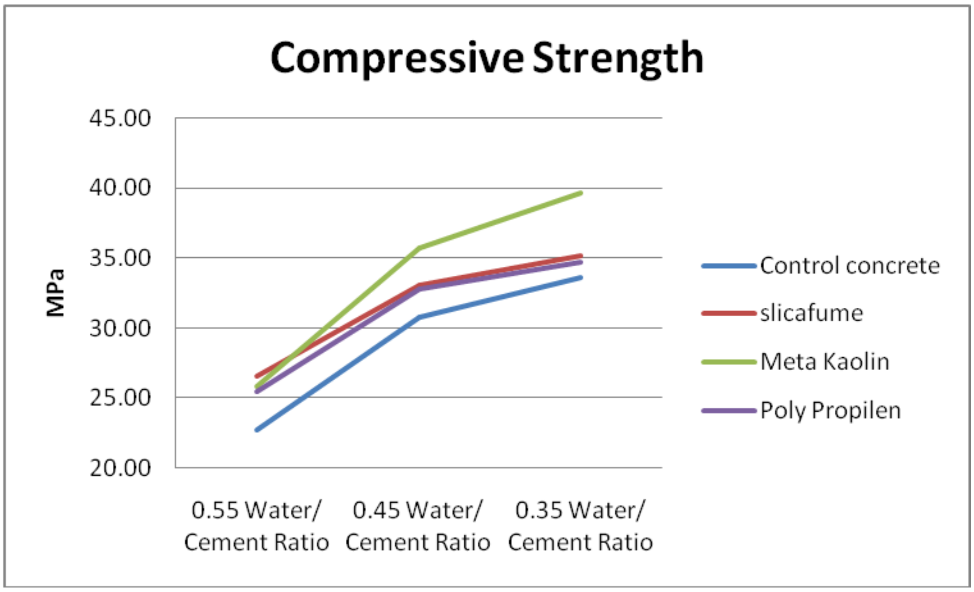

Figure 4.2. Effect of w/c ratio on compressive strength of all concrete mixtures.

4.4 Analysis and Discussion of Results Obtained from Computed Tomography Method

The experimental data for this method are the results obtained from the CT scans for all different kinds of concrete mixes. In order to accurately count the number and identify the size of pores and cracks, an extensive AutoCAD study was also done. As it was previously explained, each concrete mix is loaded at different compressive strength levels and the crack images were taken at each applied load. Below, the points at which a CT image was taken are given:

1. Imaging before loading of cylindrical cores.
2. Imaging after loading of 50 percent of ultimate load.
3. Imaging after loading of 65 percent of ultimate load.
4. Imaging after loading of 80 percent of ultimate load.
5. Imaging after critical loading (Fracture of concrete samples).

4.4.1 CT Results of 0.55 w/c Control Concrete Mixes

In Figure 4.3 the images obtained at various loading for the control sample (without any additives) of 0.55 w/c ratio is demonstrated. According to the setting of this equipment (computed tomography) all porosities, cracks and air voids were shown with black (due to low density), and materials with high density were shown with white, and the color darkens as the density decreases.

Below, in figure 4.3, CT scans for 0.55 w/c ratio, control specimen at different loading levels are given.

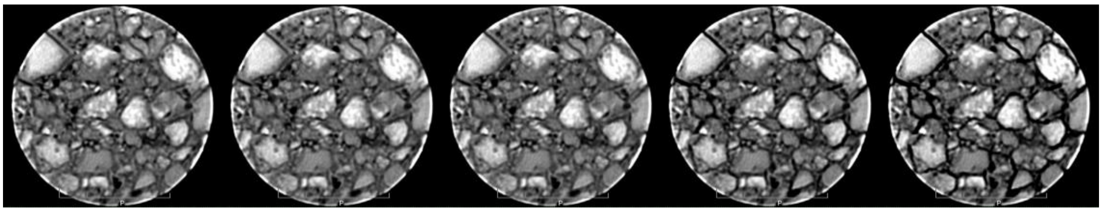

0% σ_c 50% σ_c 65% σ_c 80% σ_c 100% σ_c

Figure 4.3. CT scans for 0.55 w/c ratio, control specimen at different loading levels

Upon scanning all 0.55 w/c ratio samples, these 2D CT images were transferred to AutoCAD software to identify the sizes of the black parts which represent porosities, cracks and air voids within the specimen. These measured areas and perimeters are available in a tabular form in the Appendix. Figure 4.4 represents the AutoCAD models for 0.55 w/c ratio, control specimen.

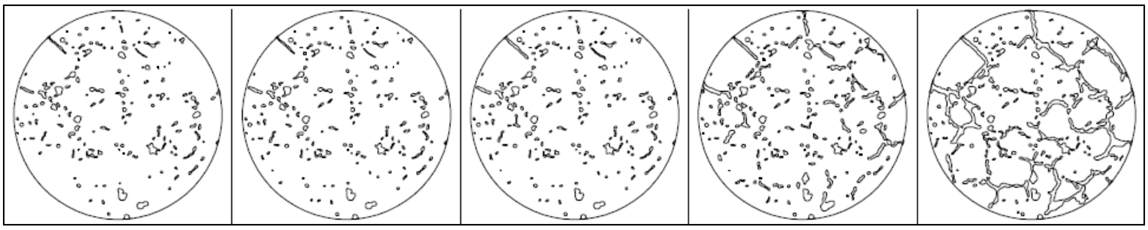

0% σ_c 50% σ_c 65% σ_c 80% σ_c 100% σ_c

Figure 4.4. AutoCAD models obtained from 2D CT Scans for 0.55 w/c ratio, control specimen at different loading levels.

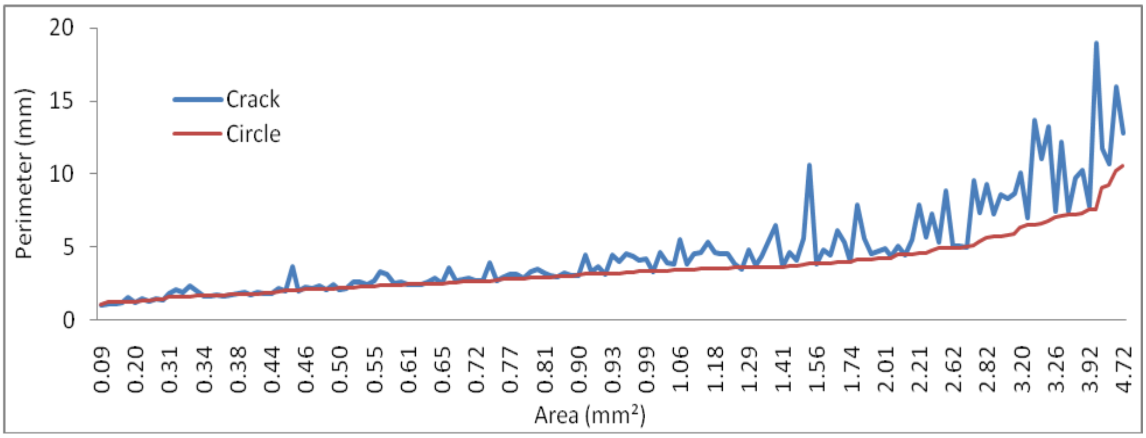

Figure 4.5. Sizes of Pores and Cracks of 0.55 w/c Control Specimens before Loading.

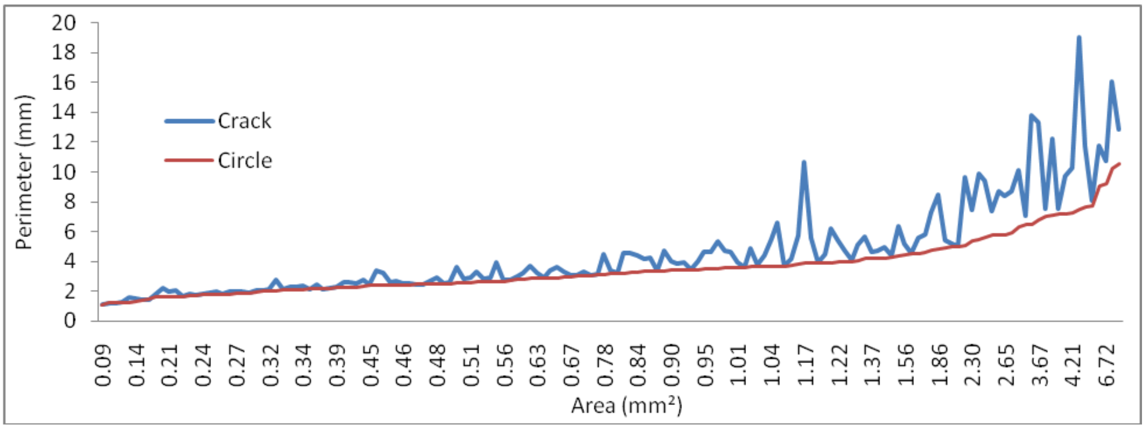

Figure 4.6. Sizes of Pores and Cracks of 0.55 w/c Control Specimens at 50%σ_c Loading Level.

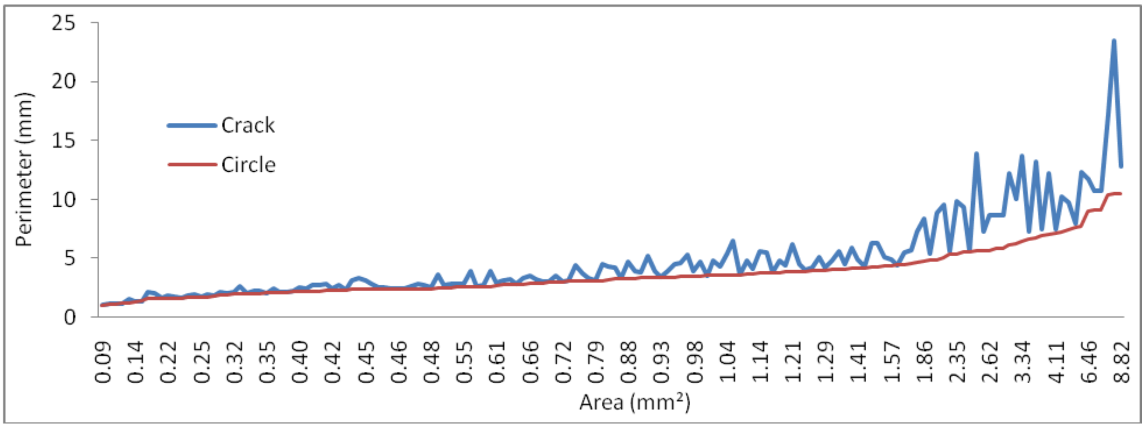

Figure 4.7. Sizes of Pores and Cracks of 0.55 w/c Control Specimens at 65%σ_c Loading Level.

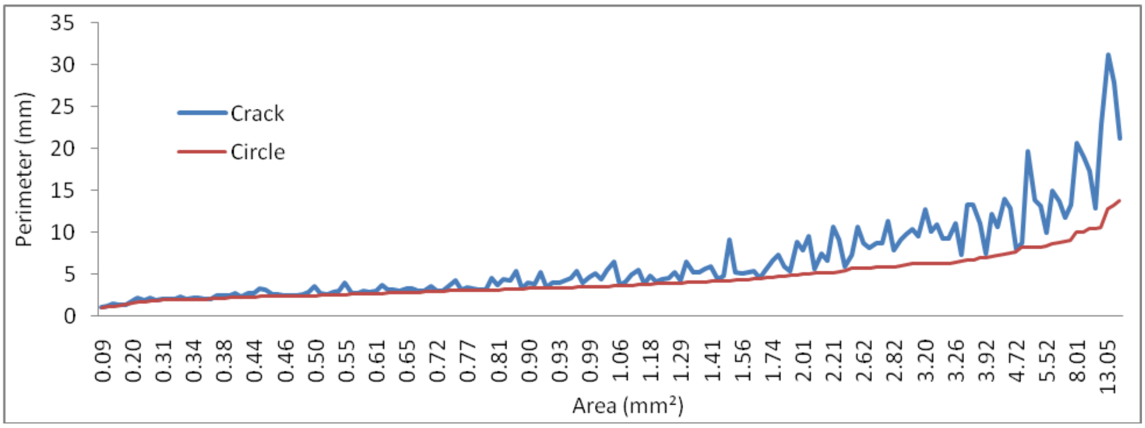

Figure 4.8. Sizes of Pores and Cracks of 0.55 w/c Control Specimens at 80%σ_c Loading Level.

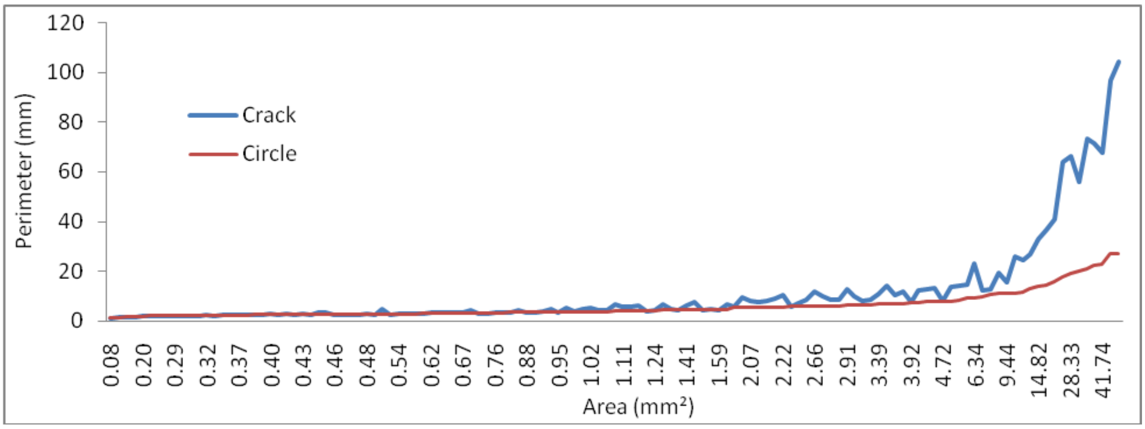

Figure 4.9. Sizes of Pores and Cracks of 0.55 w/c Control Specimens at 100%σ_c Loading Level.

4.4.1.1 Crack Size Detection from CT Scans and AutoCAD Images

Upon scanning the samples, these 2D CT images were transferred to AutoCAD software to identify the sizes of the black parts which represent porosities, cracks and air voids within the specimen. These measured areas and perimeters are available in a tabular form in below.

The increasing the percentage of the crack area can be attributed to crack propagation.

Table 4.1. Cracks and Air Voids Data Table for 0.55 w/c Control Specimens

Percentage of loading	Loading level (MPa)	Total cracks area (mm^2)	Percentage of cracks area	Total perimeter (mm)
0	0	188.41	4.26	692.93
50	11.38	191.26	4.33	696.87
65	14.79	214.15	4.85	752.62
80	18.20	341.77	7.74	1067.08
100	22.75	596.47	13.50	1439.77

Using the data provided in table 4.1, the following diagrams were constructed, representing the loading levels and crack areas and/or perimeter lengths.

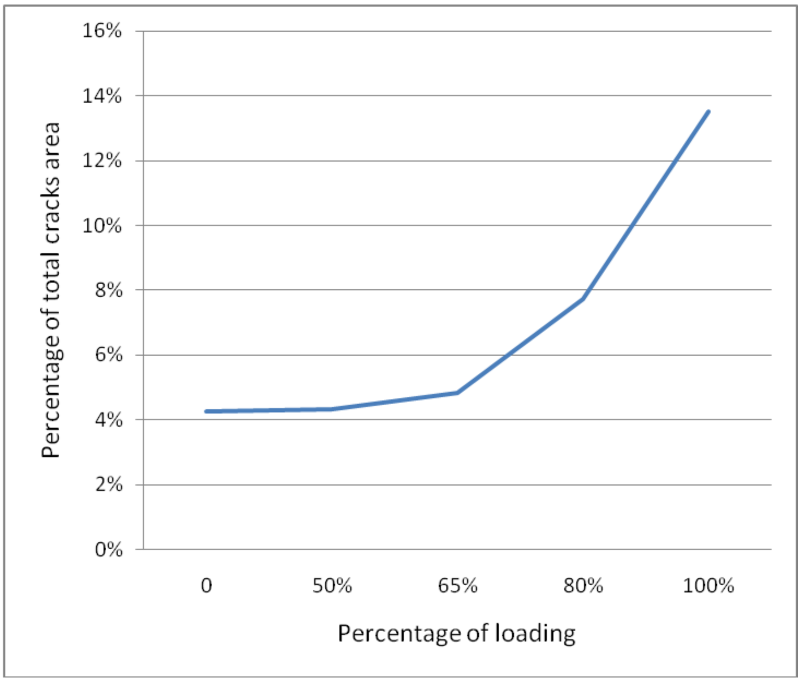

Figure 4.10. Cracks and Voids Area for 0.55 w/c Control Specimens under Different Loading Levels.

4.4.2 CT Results of 0.55 w/c Silica Fume Containing Concrete Mixes

In Figure 4.11 the images obtained at various loading for the Silica Fume containing concrete specimens of 0.55 w/c ratio is demonstrated. According to the setting of this equipment (computed tomography) all porosities, cracks and air voids were shown with black (due to low density), and materials with high density were shown with white, and the color darkens as the density decreases.

Below, in figure 4.11, CT scans for 0.55 w/c ratio, Silica Fume containing concrete specimen at different loading levels are given.

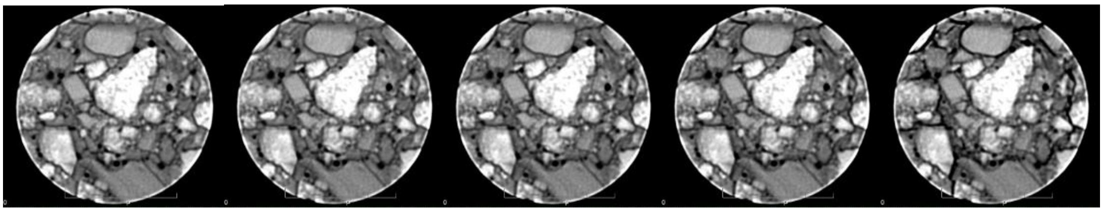

0% σ_c 50% σ_c 65% σ_c 80% σ_c 100% σ_c

Figure 4.11. CT scans for 0.55 w/c ratio, Silica Fume Containing Specimen at different loading levels.

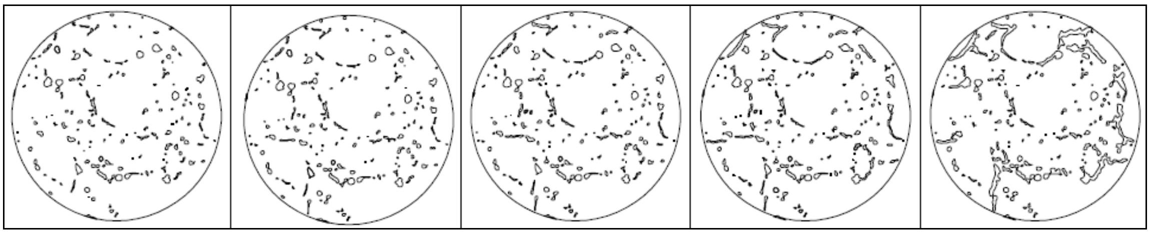

0% σ_c 50% σ_c 65% σ_c 80% σ_c 100% σ_c

Figure 4.12. AutoCAD Models obtained from 2D CT Scans for 0.55 w/c ratio, Silica Fume Containing Specimen at different loading levels.

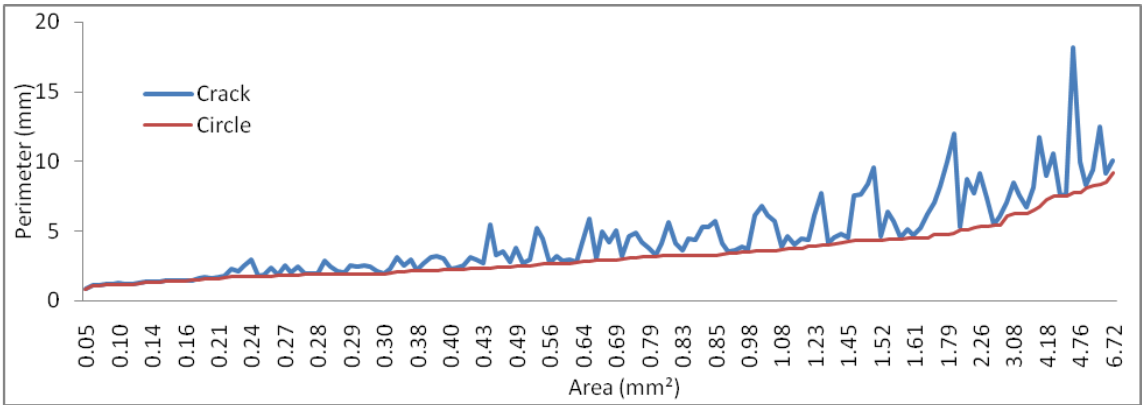

Figure 4.13. Sizes of Pores and Cracks of 0.55 w/c Silica Fume Specimens Before Loading.

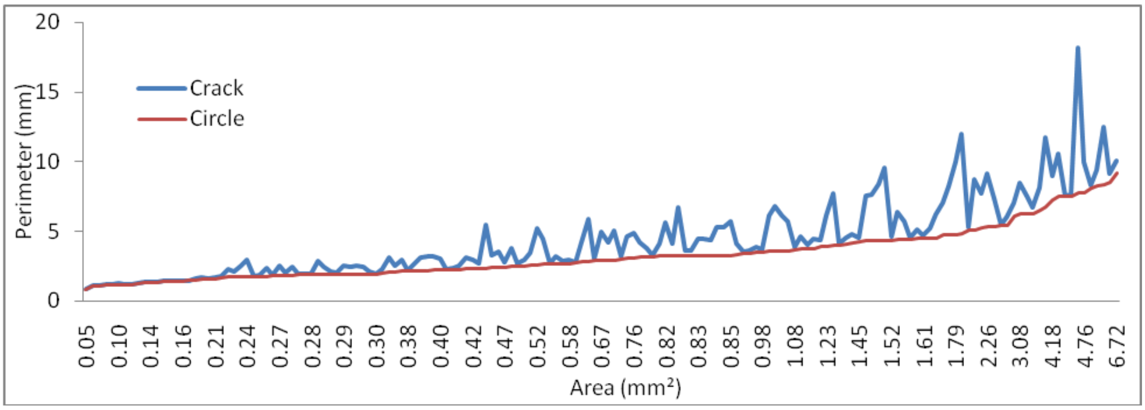

Figure 4.14. Sizes of Pores and Cracks of 0.55 w/c Silica Fume Specimens at 50%σc Loading Level.

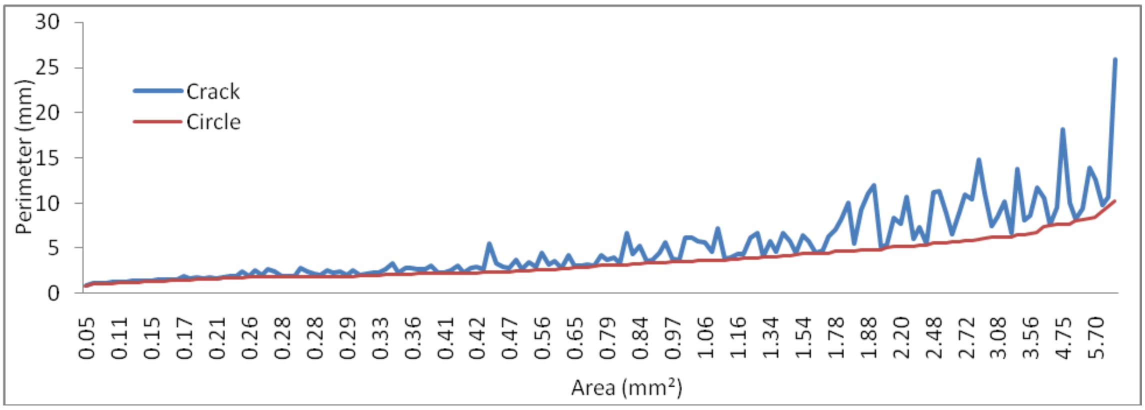

Figure 4.15. Sizes of Pores and Cracks of 0.55 w/c Silica Fume Specimens at 65%σ_c Loading Level.

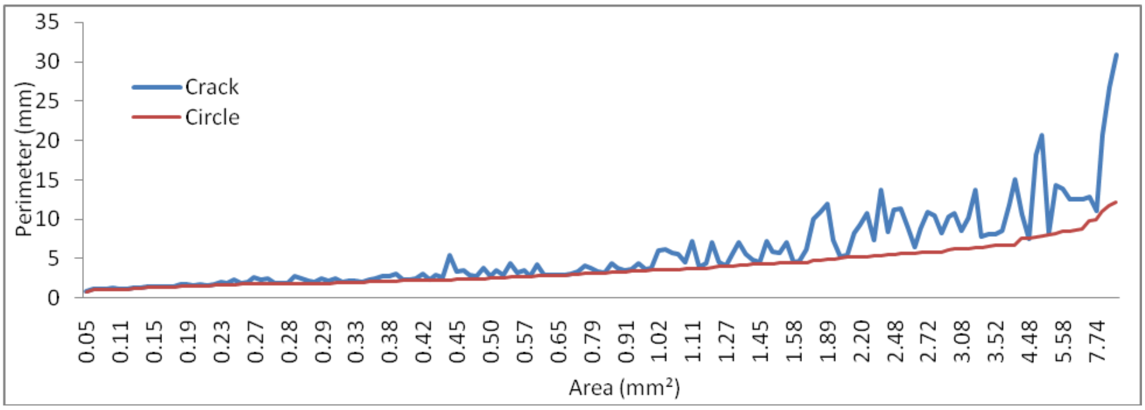

Figure 4.16. Sizes of Pores and Cracks of 0.55 w/c Silica Fume Specimens at 80%σ_c Loading Level.

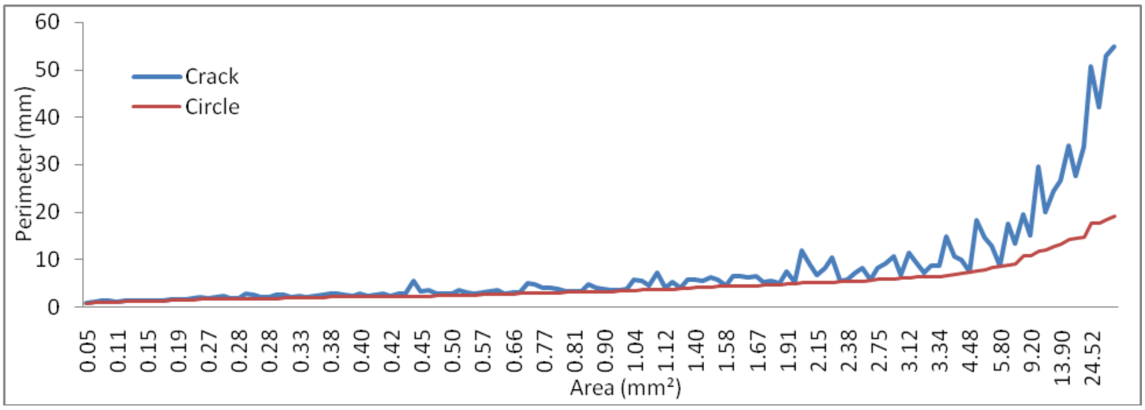

Figure 4.17. Sizes of Pores and Cracks of 0.55 w/c Silica Fume Specimens at 100%σ_c Loading Level.

4.4.2.1Crack Size Detection from CT Scans and AutoCAD Images

Upon scanning the samples, these 2D CT images were transferred to AutoCAD software to identify the sizes of the black parts which represent porosities, cracks and air voids within the specimen. These measured areas and perimeters are available in a tabular form in below.

The increasing the percentage of the crack area can be attributed to crack propagation.

Table 4.2. Cracks and Air Voids Data Table for 0.55 w/c Silica Fume Specimens

Percentage of loading	Loading level (MPa)	Total cracks area (mm²)	Percentage of cracks area	Total perimeter (mm)
0	0	177.47	4.02	684.76
50	13.29	180.86	4.09	706.08
65	17.28	214.68	4.86	796.57
80	21.26	247.50	5.60	873.27
100	26.58	387.20	8.76	1031.99

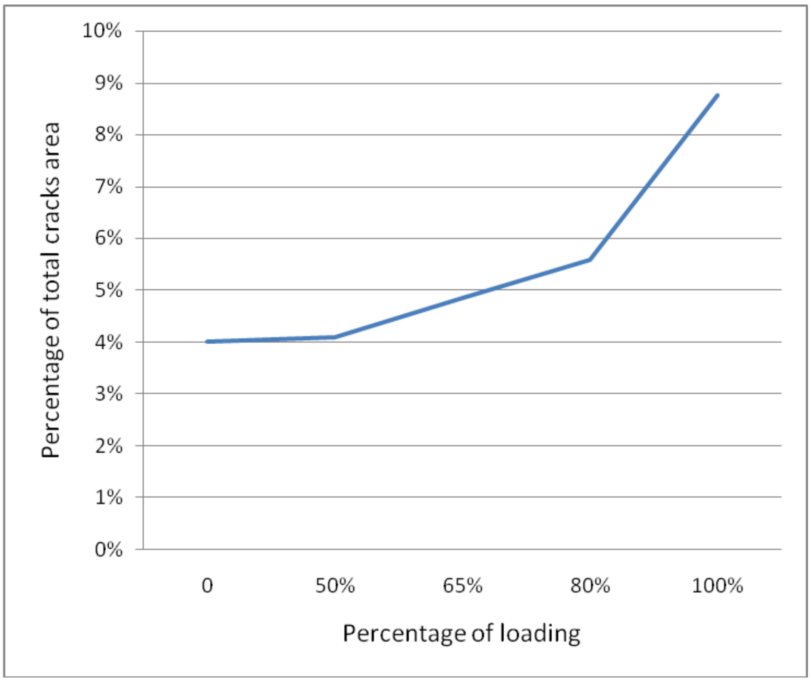

Figure 4.18. Cracks and Voids Area for 0.55 w/c Silica Fume Specimens under Different Loading Levels.

4.4.3 CT Results of 0.55 w/c Metakaolin Containing Concrete Mixes

In Figure 4.19 the images obtained at various loading for the Metakaolin containing concrete specimens of 0.55 w/c ratio is demonstrated. Below, in figure 4.19, CT scans for 0.55 w/c ratio, Metakaolin containing concrete specimen at different loading levels are given.

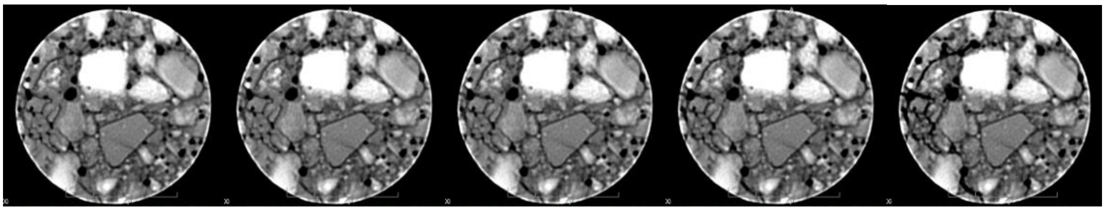

0% σ_c 50% σ_c 65% σ_c 80% σ_c 100% σ_c

Figure 4.19. CT scans for 0.55 w/c ratio, Metakaolin Containing Specimen at different loading levels.

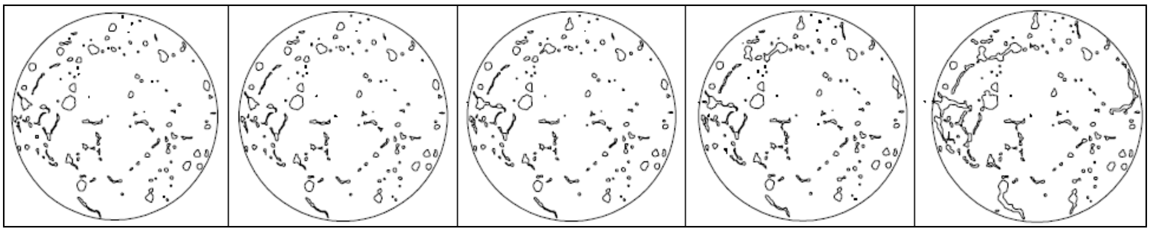

0% σ c 50% σ c 65% σ c 80% σ c 100% σ c

Figure 4.20. AutoCAD Models obtained from 2D CT Scans for 0.55 w/c ratio, Metakaolin Containing Specimen at different loading levels.

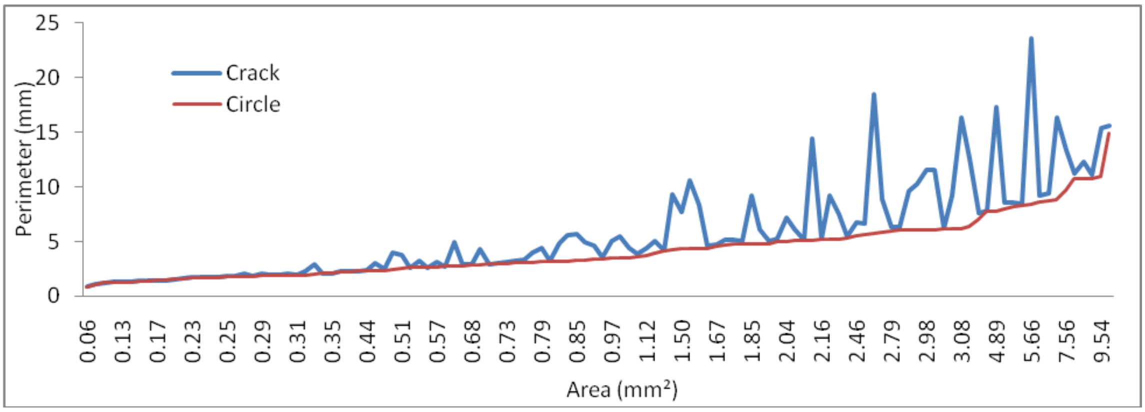

Figure 4.21. Sizes of Pores and Cracks of 0.55 w/c Metakaolin Specimens Before Loading.

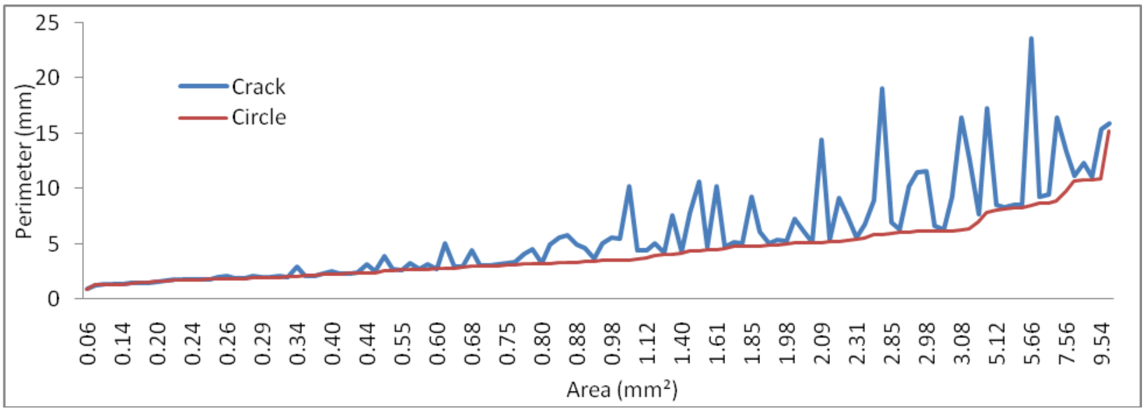

Figure 4.22. Sizes of Pores and Cracks of 0.55 w/c Metakaolin Specimens at 50%σc Loading Level.

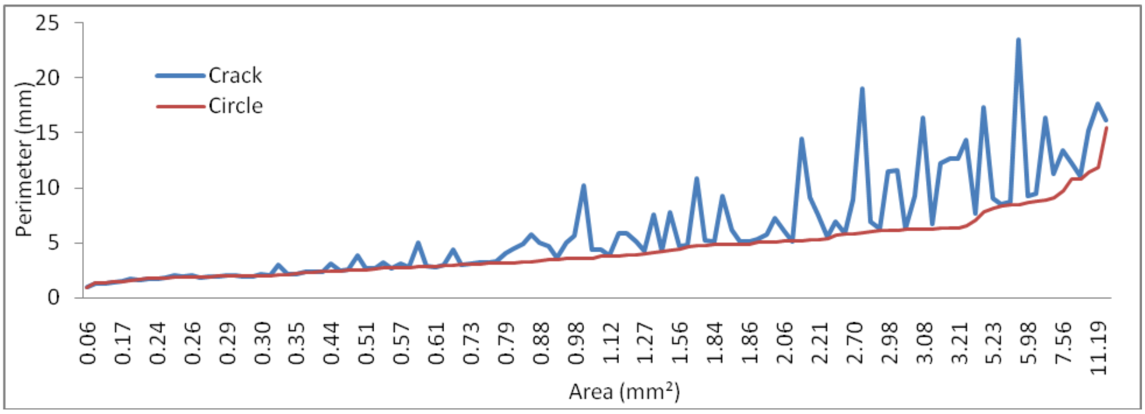

Figure 4. 23. Sizes of Pores and Cracks of 0.55 w/c Metakaolin Specimens at 65%σc Loading Level.

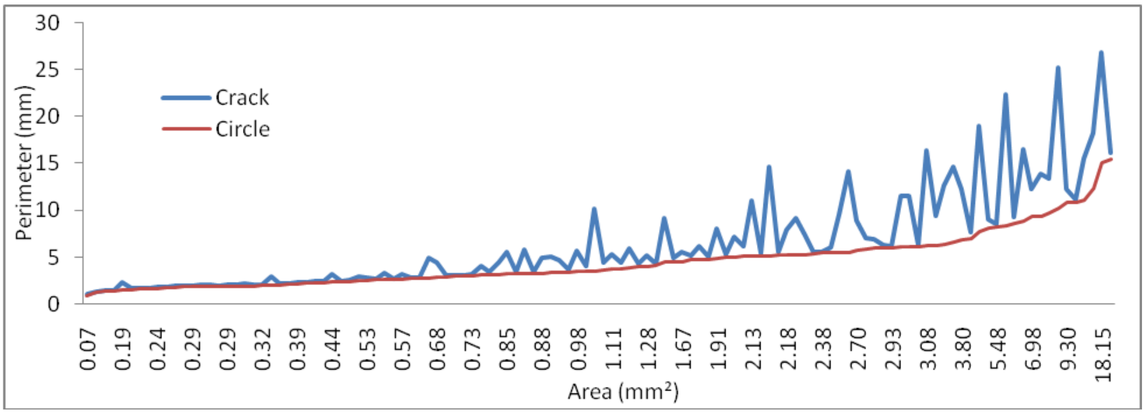

Figure 4.24. Sizes of Pores and Cracks of 0.55 w/c Metakaolin Specimens at 80%σc Loading Level.

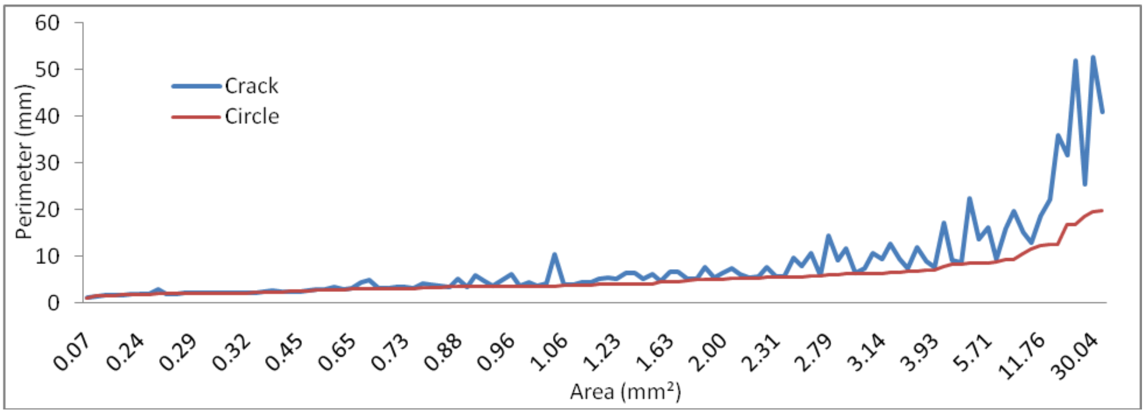

Figure 4.25. Sizes of Pores and Cracks of 0.55 w/c Metakaolin Specimens at 100%σc Loading Level.

4.4.3.1 Crack Size Detection from CT Scans and AutoCAD Images

Upon scanning the samples, these 2D CT images were transferred to AutoCAD software to identify the sizes of the black parts which represent porosities, cracks and air voids within the specimen. These measured areas and perimeters are available in a tabular form in below.

The increasing the percentage of the crack area can be attributed to crack propagation.

Table 4.3. Cracks and Air Voids Data Table for 0.55 w/c Metakaolin Specimens

Percentage of loading	Loading level (MPa)	Total cracks area (mm^2)	Percentage of cracks area	Total perimeter (mm)
0	0	230.29	5.21	674.68
50	12.90	231.64	5.24	681.28
65	16.76	245.88	5.57	716.62
80	20.63	268.99	6.09	758.12
100	25.79	364.85	8.26	905.88

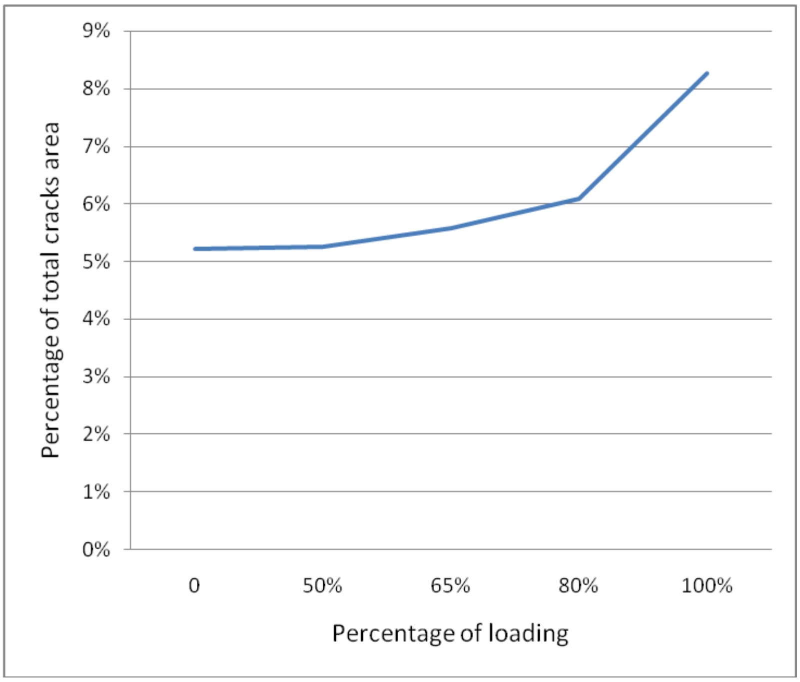

Figure 4.26. Cracks and Voids Area for 0.55 w/c Metakaolin Specimens under Different Loading Levels.

4.4.4 CT Results of 0.55 w/c Ratio Polypropylene Containing Concrete Mixes

In Figure 4.27 the images obtained at various loading for the Silica Fume containing concrete specimens of 0.55 w/c ratio is demonstrated. Below, in figure 4.27, CT scans for 0.55 w/c ratio, silica fume containing concrete specimen at different loading levels are given.

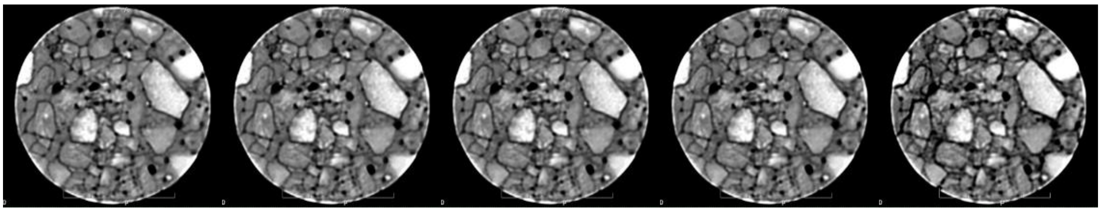

0% σ_c 50% σ_c 65% σ_c 80% σ_c 100% σ_c

Figure 4.27. CT scans for 0.55 w/c ratio, Polypropylene Containing Specimen at different loading levels.

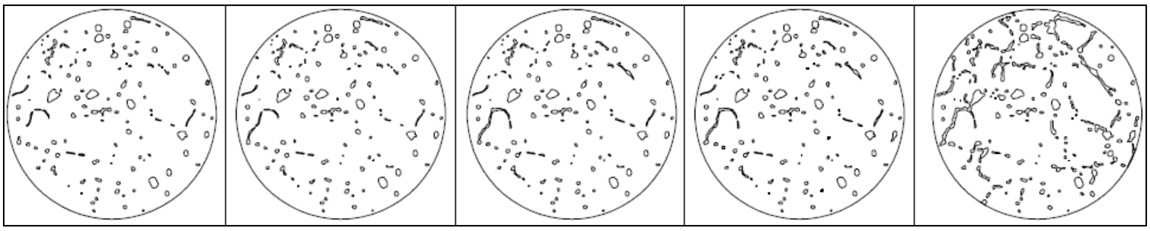

0% σ c 50% σ c 65% σ c 80% σ c 100% σ c

Figure 4.28. AutoCAD Models obtained from 2D CT Scans for 0.55 w/c ratio, Polypropylene Containing Specimen at different loading levels.

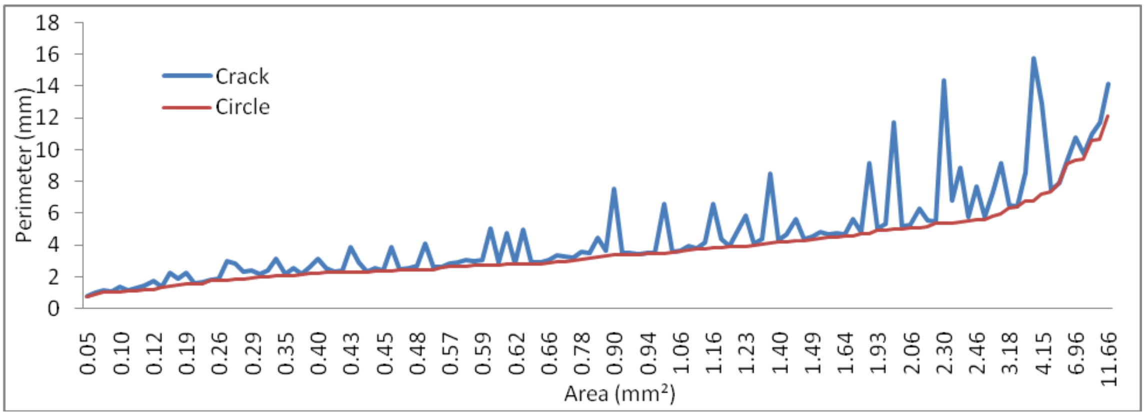

Figure 4.29. Sizes of Pores and Cracks of 0.55 w/c Polypropylene Specimens Before Loading.

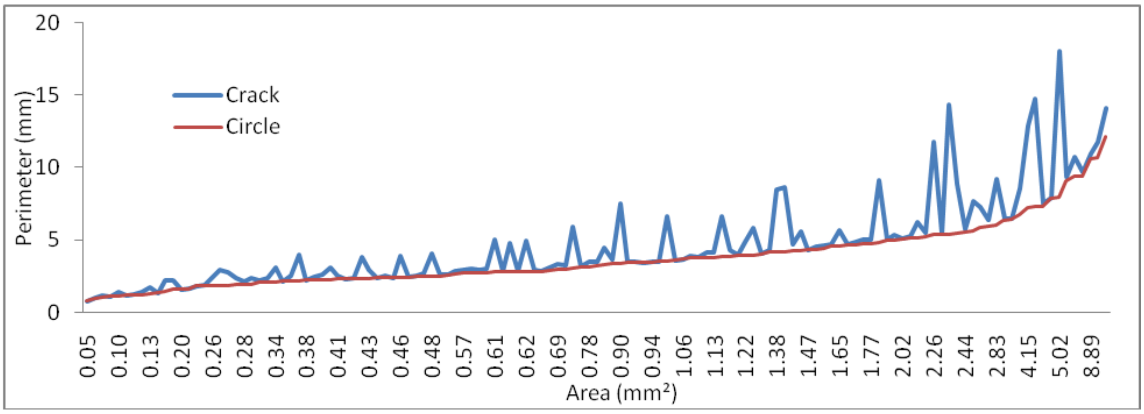

Figure 4.30. Sizes of Pores and Cracks of 0.55 w/c Polypropylene Specimens at 50%σc Loading Level.

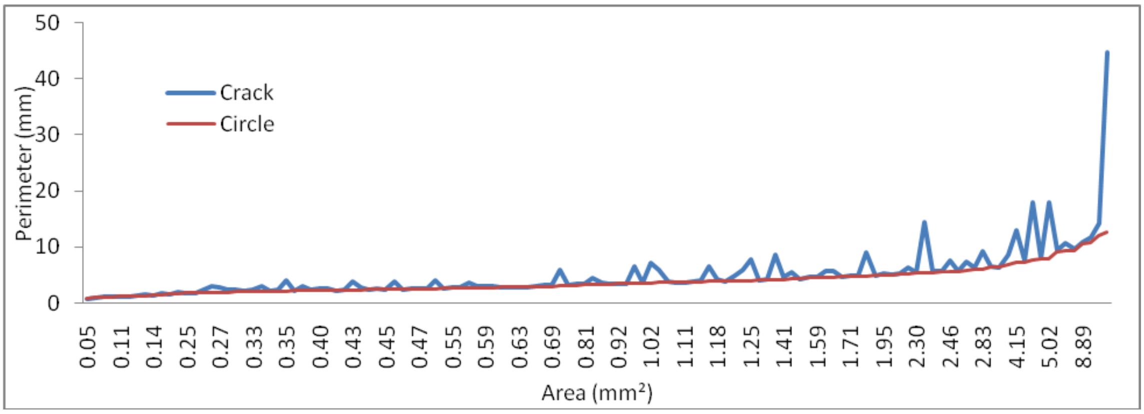

Figure 4.31. Sizes of Pores and Cracks of 0.55 w/c Polypropylene Specimens at 65%σc Loading Level.

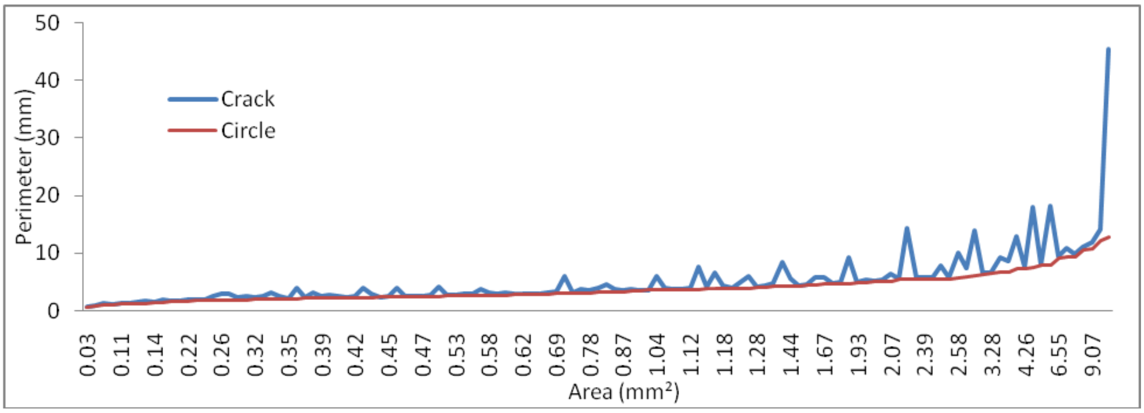

Figure 4. 32. Sizes of Pores and Cracks of 0.55 w/c Polypropylene Specimens at 80%σc Loading Level.

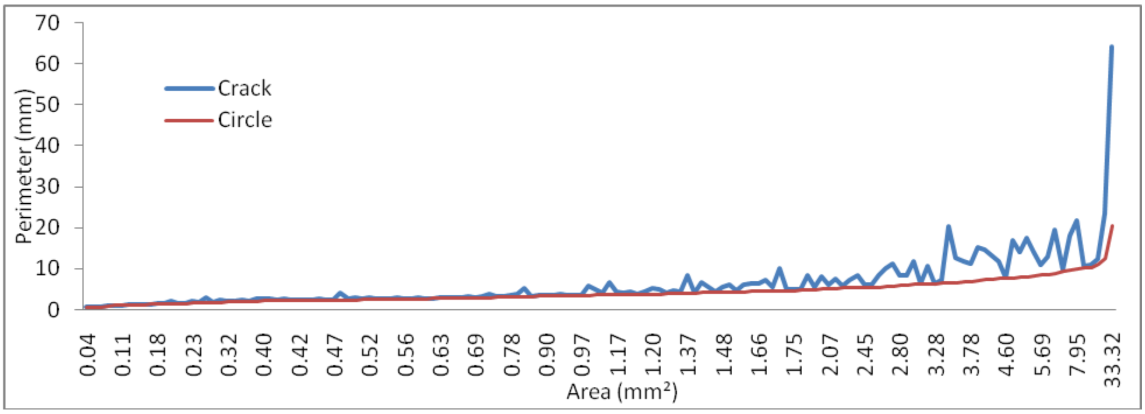

Figure 4. 33. Sizes of Pores and Cracks of 0.55 w/c Polypropylene Specimens at 100%σc Loading Level.

4.4.4.1 Crack Size Detection from CT Scans and AutoCAD Images

Upon scanning the samples, these 2D CT images were transferred to AutoCAD software to identify the sizes of the black parts which represent porosities, cracks and air voids within the specimen. These measured areas and perimeters are available in a tabular form in below.

The increasing the percentage of the crack area can be attributed to crack propagation.

Table 4.4. Cracks and Air Voids Data Table for 0.55 w/c Polypropylene Specimens

Percentage of loading	Loading level (MPa)	Total cracks area (mm^2)	Percentage of cracks area	Total perimeter (mm)
0	0	180.8706	4.09	570.65
50	12.74	189.62	4.29	610.23
65	16.57	196.41	4.44	620.11
80	21.67	197.12	4.46	622.14
100	25.50	299.24	6.77	908.21

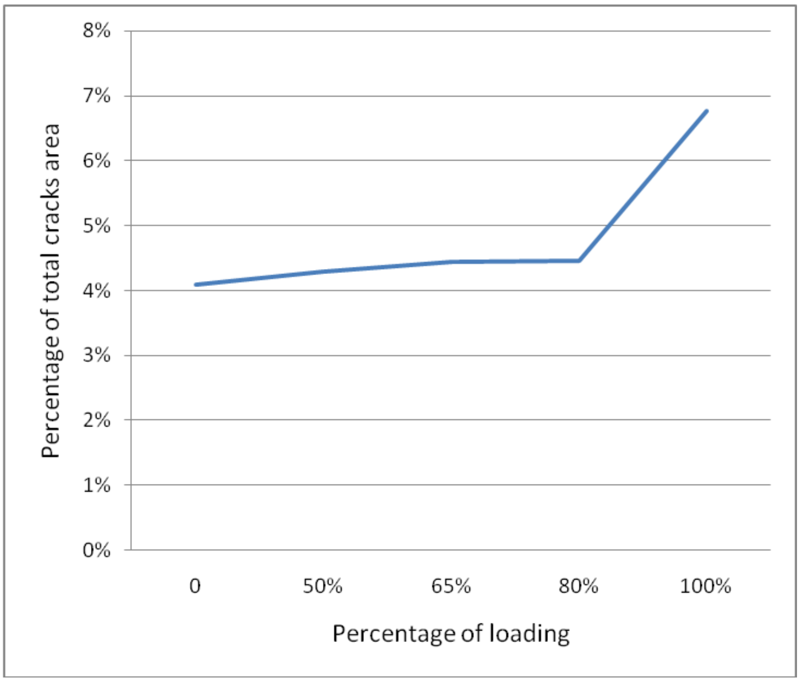

Figure 4.34. Cracks and Voids Area for 0.55 w/c Polypropylene Specimens under Different Loading Levels.

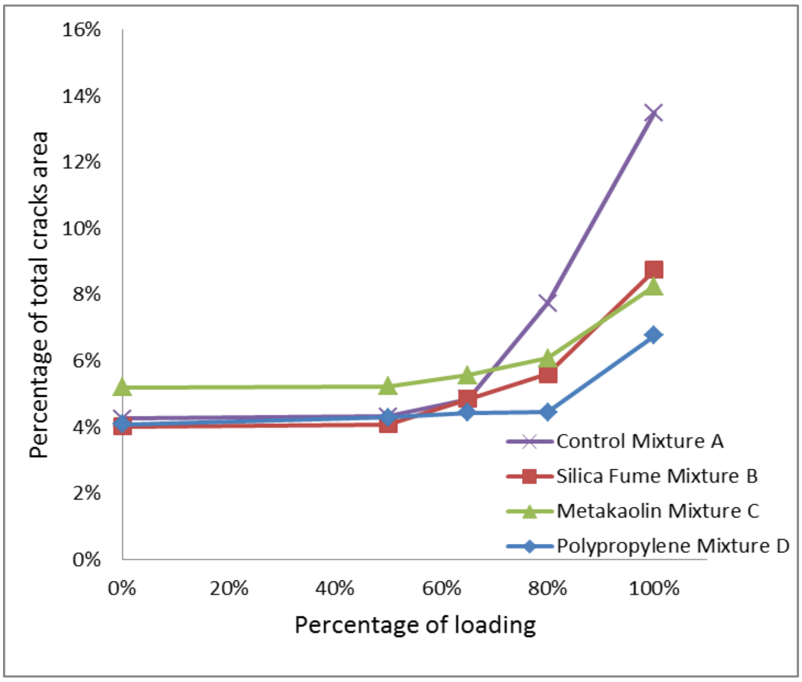

Figure 4.35. % Area of Cracks and Voids w.r.t total X-Sectional Area for 0.55 w/c Mixes under Different Loading Levels.

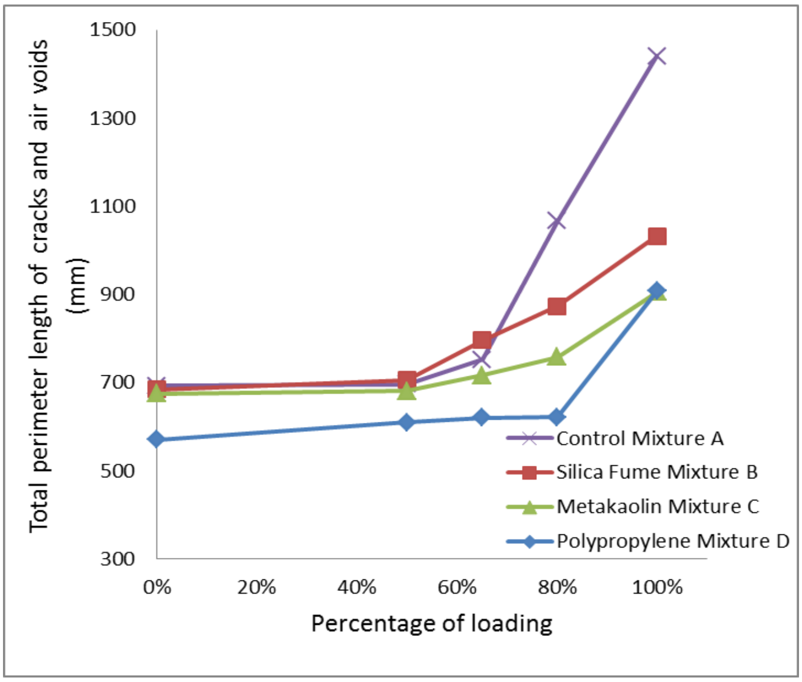

Figure 4. 36. Total perimeter lengths of Cracks and Voids of 0.55 w/c Mixes under Different Loading Levels.

4.5 Analysis and Discussion of CT results for 0.55 W/C Ratio Mixes

The total percent voids and cracks with respect to the cross-sectional area relative to the percent of loading are represented in Figure 4.35. As it can be seen from the graph, at zero percent loading, control specimen, mixture with silica fume and the mixture with polypropylene has the same percentage of cracks (4%) while metakaolin mixture shows slightly higher rate of 5% up to about 60% of loading. The critical turning point for rapid crack propagation is 60% of loading for the control specimen and 80% of loading for the other mixes. Beyond this point, control shows a sharp increment and reaches approximately 14% crack area, followed by silica fume at 9%, metakaolin at 8% and finally polypropylene at 7% when the specimens are loaded at 100%. From these results it can be inferred that for 0.55 w/c ratio, polypropylene has the most quality to prevent crack propagation. In addition, the sharp increment in control specimen indicates that mixtures with mineral additives decrease the crack propagation rate past 60% of loading, despite the initial similarities in crack areas up until that point. This means that mineral additives increase the tensile strength capacity of the material, particularly at the interfacial transition zones.

When the total perimeter length for cracks and air voids are concerned (Figure 4.36), the largest crack perimeter belongs to the control specimen, followed by silica fume, and metakaolin and polypropylene have the same perimeter at 100% loading. When compared with the % area of cracks, the critical turning point for total perimeter is 50% for silica fume and metakaolin, 65% for the control specimen and 80% for polypropylene. Polypropylene also shows the shortest perimeter of 600mm at no load point, while all other three samples start at approximately 700mm length.

The data on cracks and air voids, related with the area and perimeter length given for each void or crack is tabulated on Figure 4.5 to 4.9, 4.13 to 4.17, 4.21 to 4.25 and 4.29 to 4.33. When we look at the change in perimeter length with changing pore or crack areas, it highly correlates with the conclusions made earlier in this section.

4.6.1 Results of 0.45 w/c Control Concrete Mixes

In Figure 4.36 the images obtained at various loading for the control sample (without any additives) of 0.45 w/c ratio is demonstrated. According to the setting of this equipment (computed tomography) all porosities, cracks and air voids were shown with black (due to low density), and materials with high density were shown with white, and the color darkens as the density decreases. Below, in figure 4.37, CT scans for 0.45 w/c ratio, control specimen at different loading levels are given.

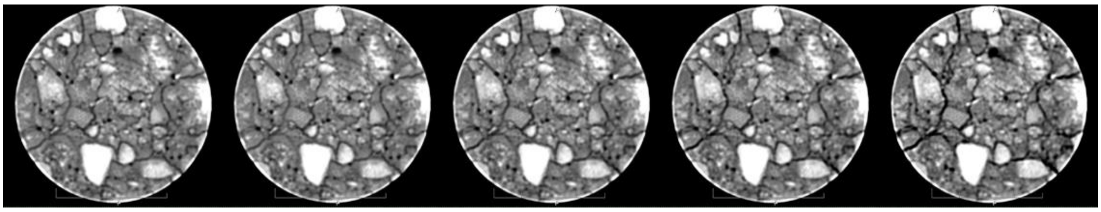

0% σ_c 50% σ_c 65% σ_c 80% σ_c 100% σ_c

Figure 4.37. CT scans for 0.45 w/c ratio, control specimen at different loading levels.

Upon scanning all 0.45 w/c ratio samples, these 2D CT images were transferred to AutoCAD software to identify the sizes of the black parts which represent porosities, cracks and air voids within the specimen. These measured areas and perimeters are available in a tabular form in the Appendix.

Figure 4.38 represents the AutoCAD models for 0.45 w/c ratio, control specimen.

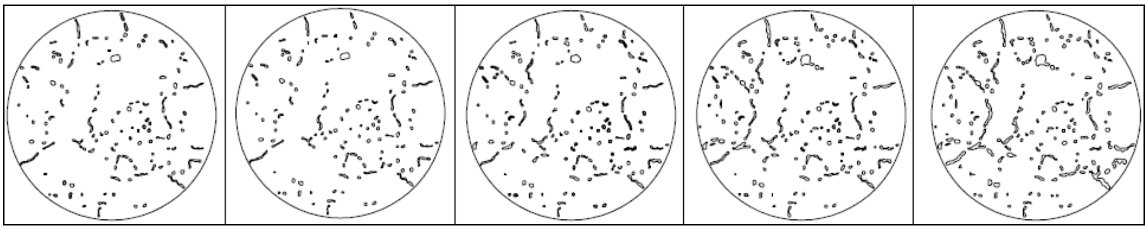

0% σ_c 50% σ_c 65% σ_c 80% σ_c 100% σ_c

Figure 4.38. AutoCAD models obtained from 2D CT Scans for 0.45 w/c ratio, control specimen at different loading levels.

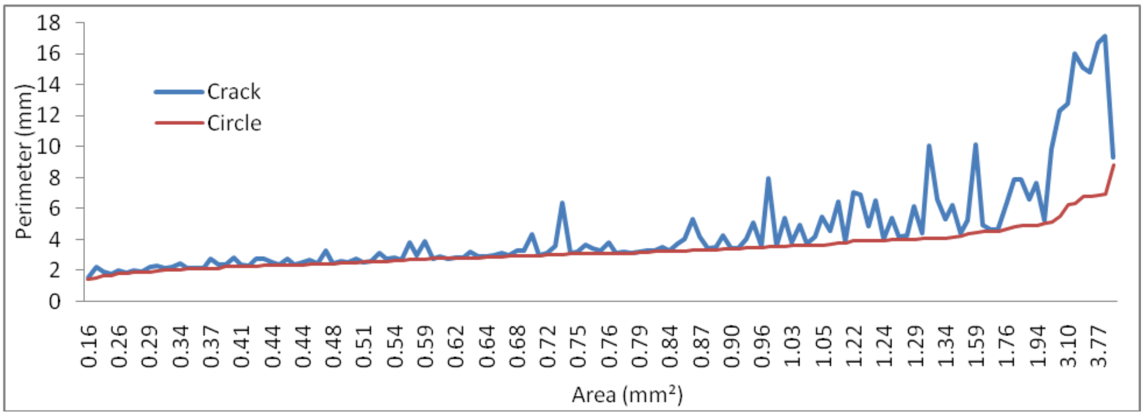

Figure 4.39. Sizes of Pores and Cracks of 0.45 w/c Control Specimens Before Loading.

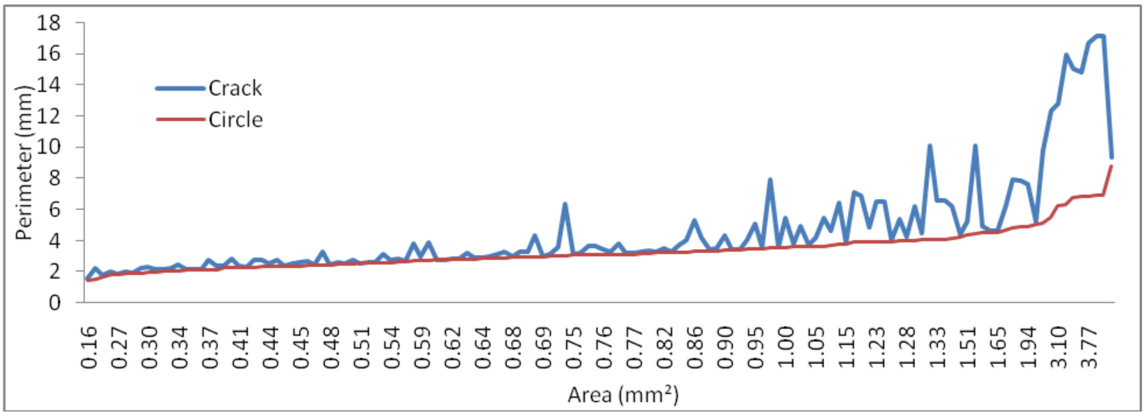

Figure 4.40. Sizes of Pores and Cracks of 0.45 w/c Control Specimens at 50%σc Loading Level.

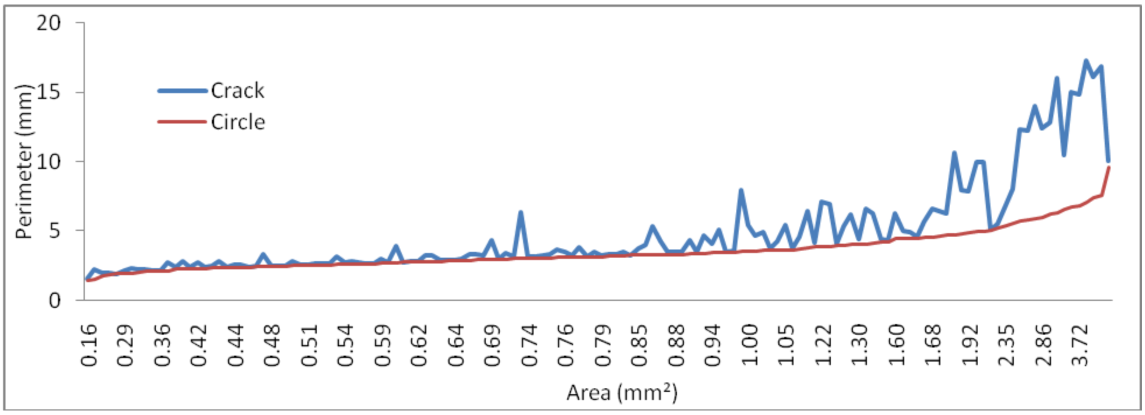

Figure 4.41. Sizes of Pores and Cracks of 0.45 w/c Control Specimens at 65%σc Loading Level.

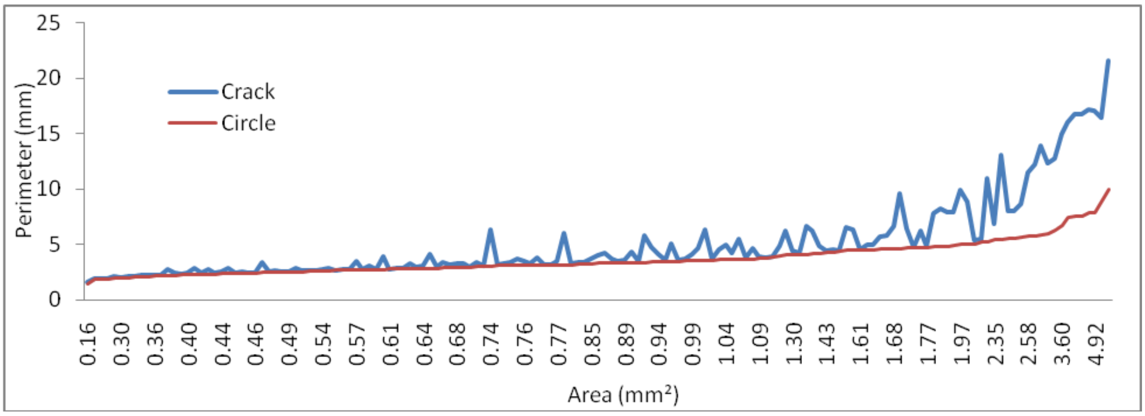

Figure 4.42. Sizes of Pores and Cracks of 0.45 w/c Control Specimens at 80%σc Loading Level.

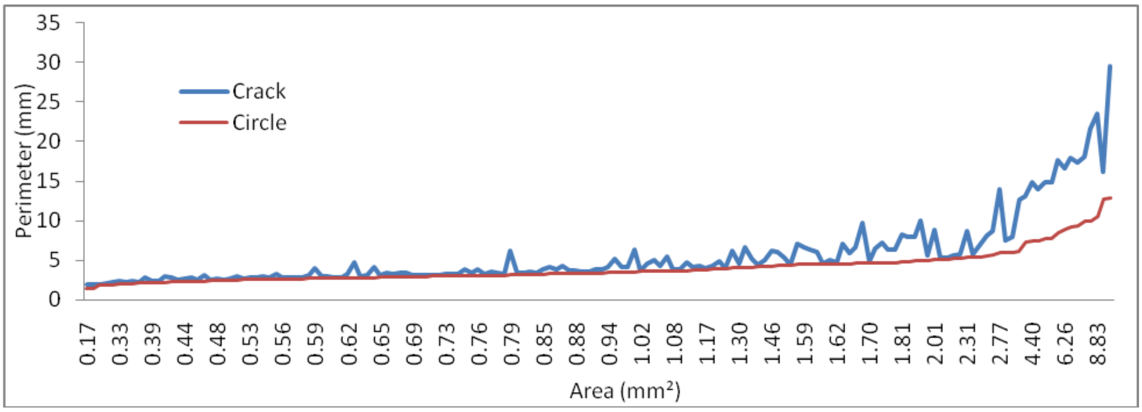

Figure 4.43. Sizes of Pores and Cracks of 0.45 w/c Control Specimens at 100%σc Loading Level.

4.6.1.1 Crack Size Detection from CT Scans and AutoCAD Images

Upon scanning the samples, these 2D CT images were transferred to AutoCAD software to identify the sizes of the black parts which represent porosities, cracks and air voids within the specimen. These measured areas and perimeters are available in a tabular form in below. The increasing the percentage of the crack area can be attributed to crack propagation.

Table 4.5. Cracks and Air Voids Data Table for 0.45 w/c Control Specimens.

Percentage of loading	Loading level (MPa)	Total cracks area (mm^2)	Percentage of cracks area	Total perimeter (mm)
0	0	134.03	3.03	603.65
50	15.40	136.56	3.09	546.80
65	20.01	159.00	3.60	682.59
80	24.63	188.59	4.27	781.41
100	30.79	251.57	5.69	879.91

Using the data provided in table 4.5, the following diagram was constructed, representing the loading levels and crack areas and/or perimeter lengths.

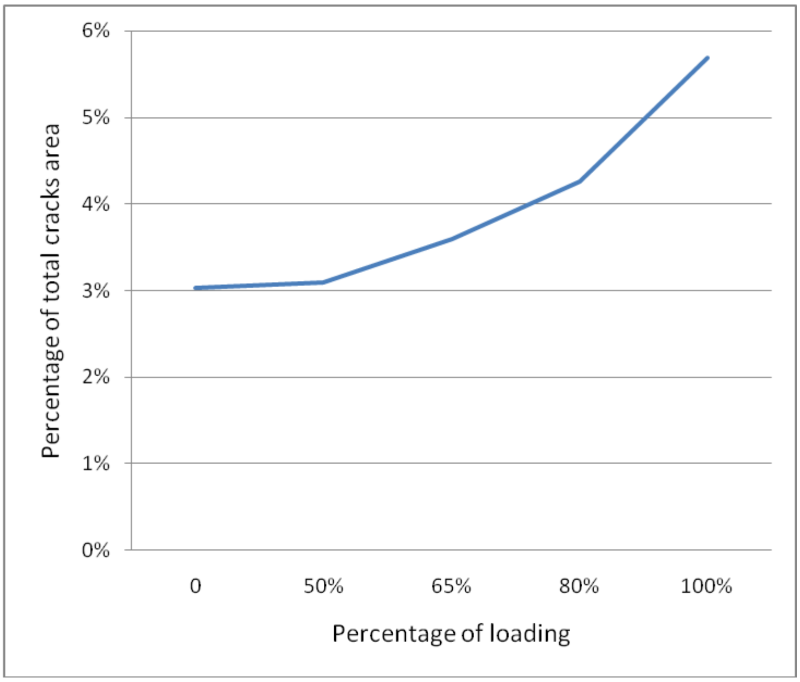

Figure 4.44. Cracks and Voids Area for 0.45 w/c Control Specimens under Different Loading Levels.

4.6.2 Analysis of 0.45 w/c Silica Fume Concrete Mixes

In Figure 4.45 the images obtained at various loading for the silica fume sample of 0.45 w/c ratio is demonstrated. According to the setting of this equipment (computed tomography) all porosities, cracks and air voids were shown with black (due to low density), and materials with high density were shown with white, and the color darkens as the density decreases.

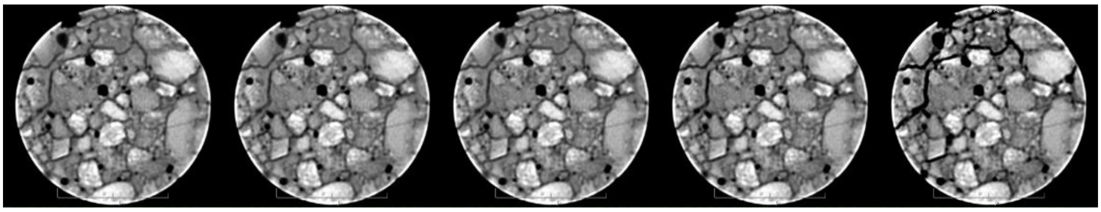

0% σ_c 50% σ_c 65% σ_c 80% σ_c 100% σ_c

Figure 4.45. CT scans for 0.45 w/c ratio, Silica Fume specimen at different loading levels.

Upon scanning all 0.45 w/c ratio samples, these 2D CT images were transferred to AutoCAD software to identify the sizes of porosities, cracks and air voids within the specimen. Figure 4.46 represents the AutoCAD models for 0.45 w/c ratio, control specimen.

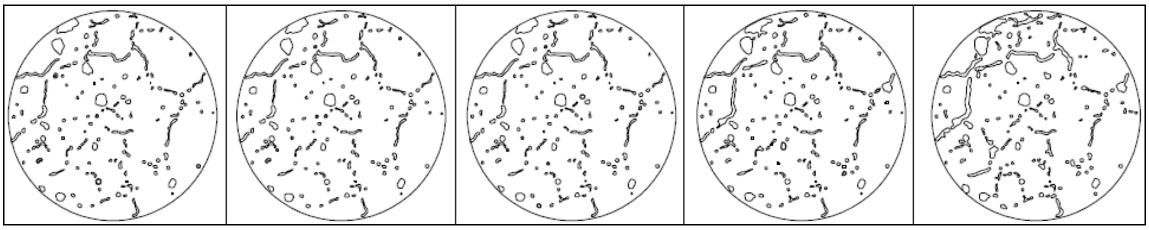

0% σ_c 50% σ_c 65% σ_c 80% σ_c 100% σ_c

Figure 4.46. AutoCAD models obtained from 2D CT Scans for 0.45 w/c ratio, Silica Fume Specimen at different loading levels.

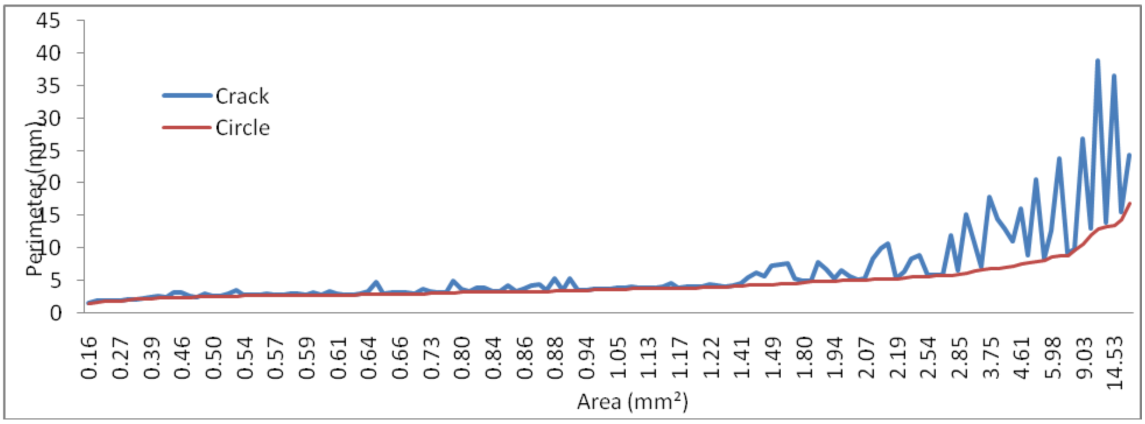

Figure 4.47. Sizes of Pores and Cracks of 0.45 w/c Silica fume Specimens Before Loading.

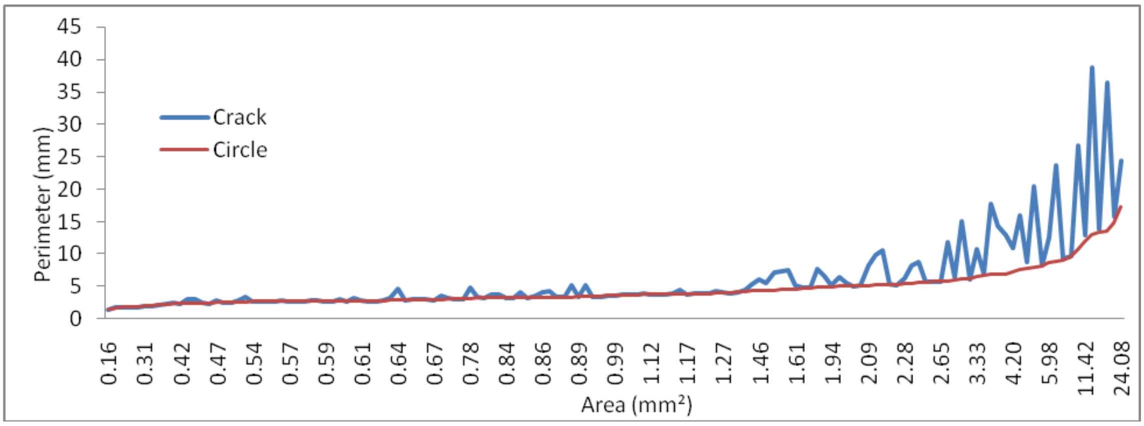

Figure 4.48. Sizes of Pores and Cracks of 0.45 w/c Silica fume Specimens at 50%σc Loading Level.

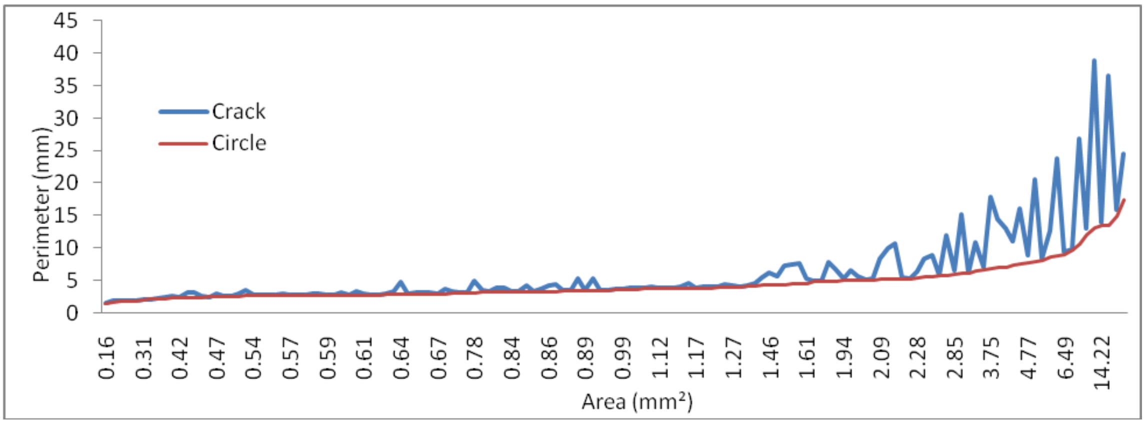

Figure 4.49. Sizes of Pores and Cracks of 0.45 w/c Silica Fume Specimens at 65%σc Loading Level.

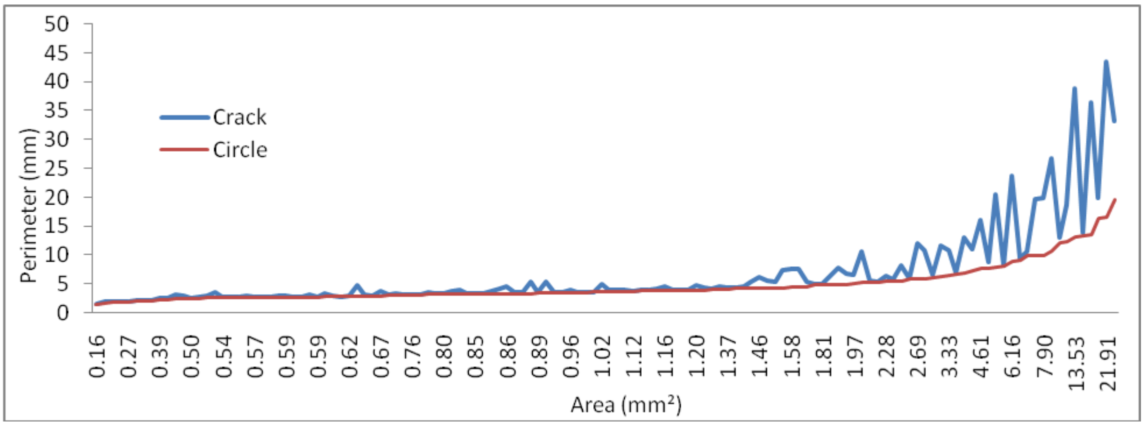

Figure 4. 50. Sizes of Pores and Cracks of 0.45 w/c Silica Fume Specimens at 80%σc Loading Level.

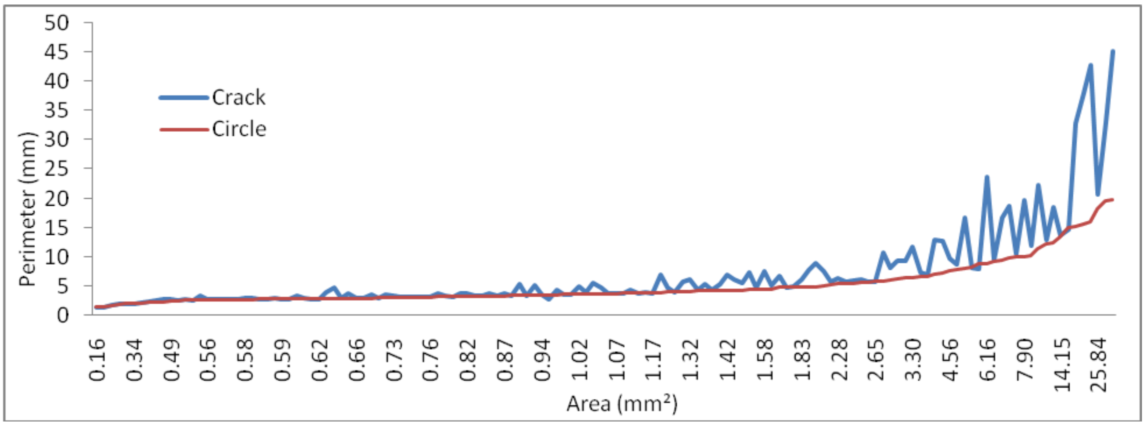

Figure 4.51. Sizes of Pores and Cracks of 0.45 w/c Silica Fume Specimens at 100%σc Loading Level.

4.6.2.1 Crack Size Detection from CT Scans and AutoCAD Images

Upon scanning the samples, these 2D CT images were transferred to AutoCAD software to identify the sizes of porosities, cracks and air voids within the specimen. These measured areas and perimeters are available in a tabular form in below. The increasing the percentage of the crack area can be attributed to crack propagation.

Table 4.6. Cracks and Air Voids Data Table for 0.45 w/c Silica Fume Specimens.

Percentage of loading	Loading level (MPa)	Total cracks area (mm^2)	Percentage of cracks area	Total perimeter (mm)
0	0	293.05	6.63	826.49
50	16.53	298.50	6.76	839.26
65	21.48	303.63	6.87	850.77
80	26.44	334.51	7.57	875.28
100	33.05	424.18	9.60	975.81

Using the data provided in table 4.5, the following diagram was constructed, representing the loading levels and crack areas and/or perimeter lengths.

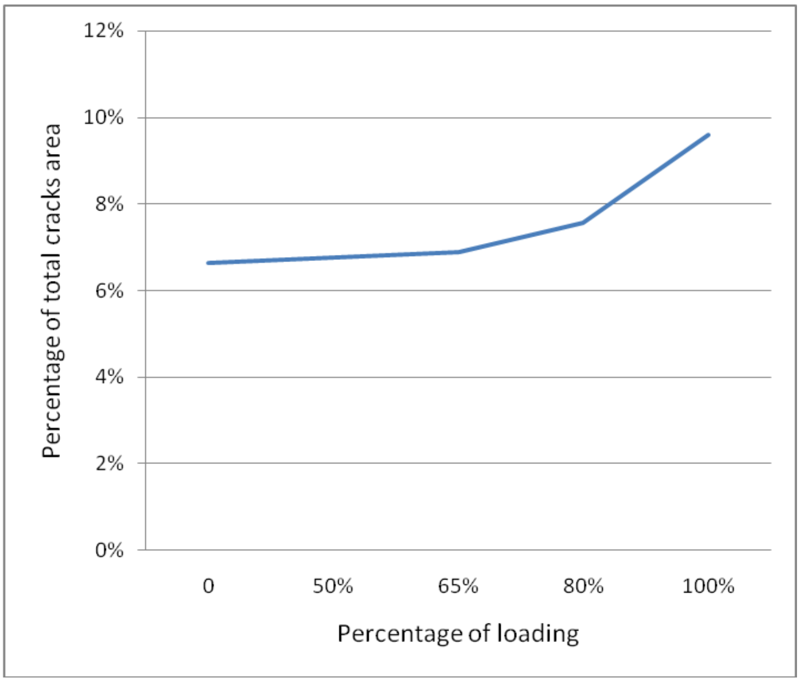

Figure 4.52. Cracks and Voids Area for 0.45 w/c Silica Fume Specimens under Different Loading Levels.

4.6.3 Analysis of 0.45 w/c Silica Fume Concrete Mixes

In Figure 4.51 the images obtained at various loading for the silica fume sample of 0.45 w/c ratio is demonstrated.

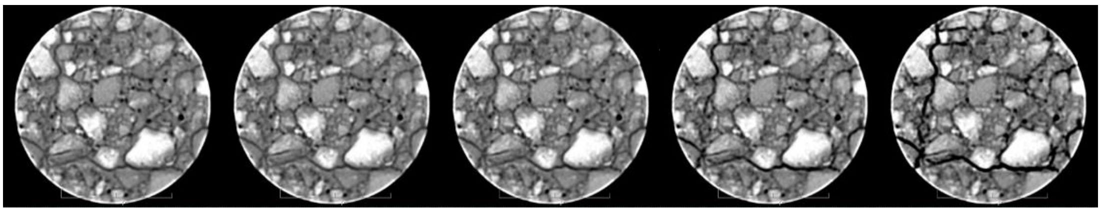

0% σ_c 50% σ_c 65% σ_c 80% σ_c 100% σ_c

Figure 4.53. CT scans for 0.45 w/c ratio, Metakaolin specimen at different loading levels.

Upon scanning all 0.45 w/c ratio samples, these 2D CT images were transferred to AutoCAD software to identify the sizes of porosities, cracks and air voids within the specimen. Figure 4.45 represents the AutoCAD models for 0.45 w/c ratio, Metakaolin specimen.

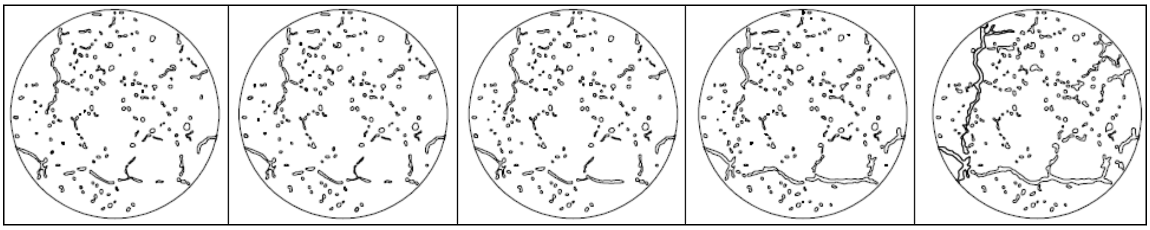

0% σ_c 50% σ_c 65% σ_c 80% σ_c 100% σ_c

Figure 4.54. AutoCAD models obtained from 2D CT Scans for 0.45 w/c ratio, Metakaolin Specimen at different loading levels.

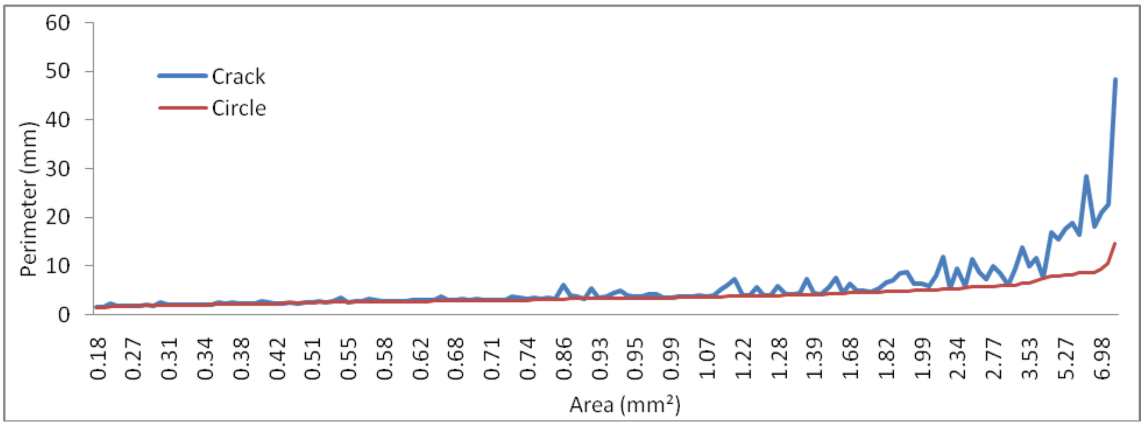

Figure 4.55. Sizes of Pores and Cracks of 0.45 w/c Metakaolin Specimens Before Loading.

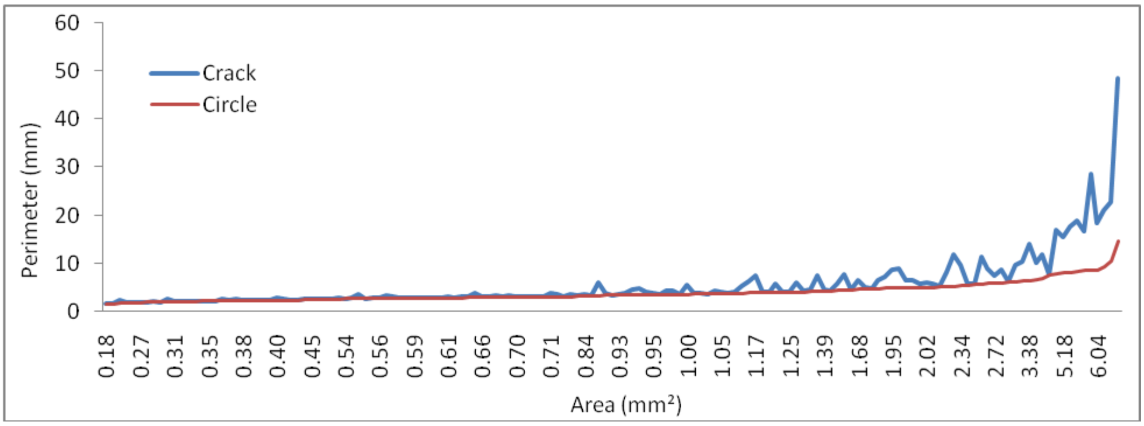

Figure 4.56. Sizes of Pores and Cracks of 0.45 w/c Metakaolin Specimens at 50%σc Loading Level.

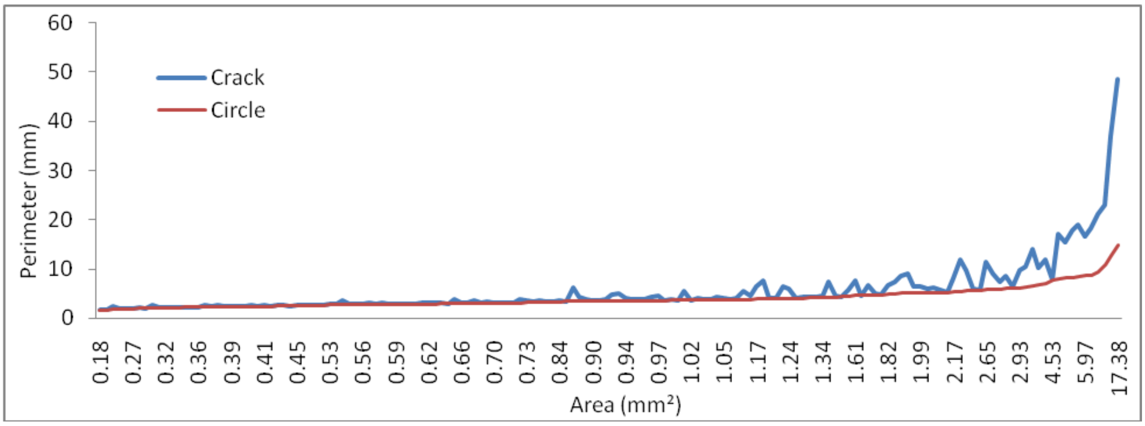

Figure 4.57. Sizes of Pores and Cracks of 0.45 w/c Metakaolin Specimens at 65%σc Loading Level.

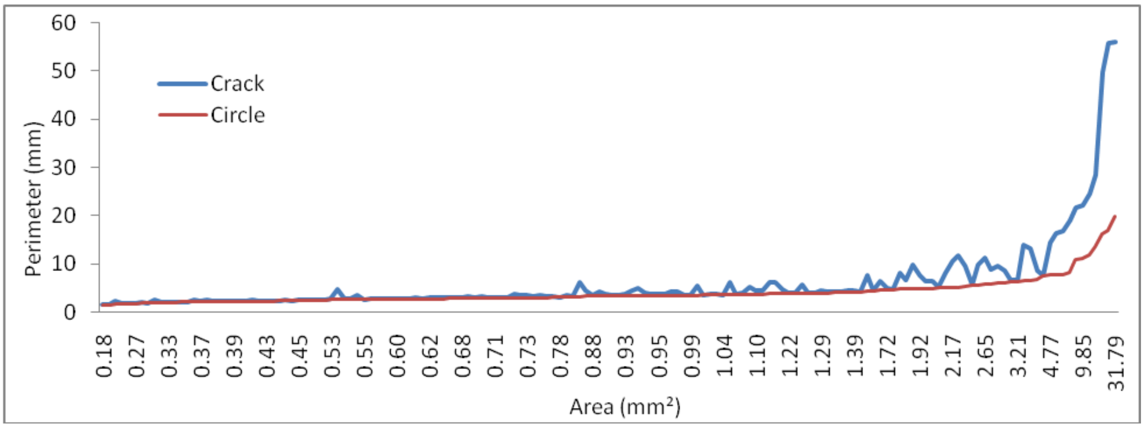

Figure 4.58. Sizes of Pores and Cracks of 0.45 w/c Metakaolin Specimens at 80%σc Loading Level.

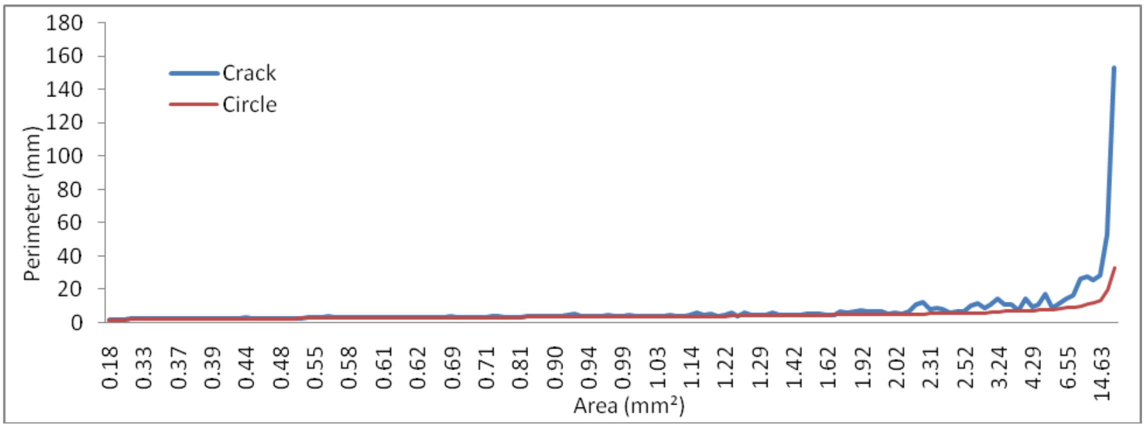

Figure 4.59. Sizes of Pores and Cracks of 0.45 w/c Metakaolin Specimens at 100%σc Loading Level.

4.6.3.1 Crack Size Detection from CT Scans and AutoCAD Images

Upon scanning the samples, these 2D CT images were transferred to AutoCAD software to identify the sizes of porosities, cracks and air voids within the specimen. These measured areas and perimeters are available in a tabular form in below. The increasing the percentage of the crack area can be attributed to crack propagation.

Table 4.7. Cracks and Air Voids Data Table for 0.45 w/c Metakaolin Specimens.

Percentage of loading	Loading level (MPa)	Total cracks area (mm^2)	Percentage of cracks area	Total perimeter (mm)
0	0	218.30	4.94	805.18
50	17.85	223.56	5.06	823.91
65	23.21	237.83	5.38	859.78
80	28.56	295.42	6.69	944.46
100	35.70	354.04	8.01	995.39

Using the data provided in table 4.7, the following diagram was constructed, representing the loading levels and crack areas and/or perimeter lengths.

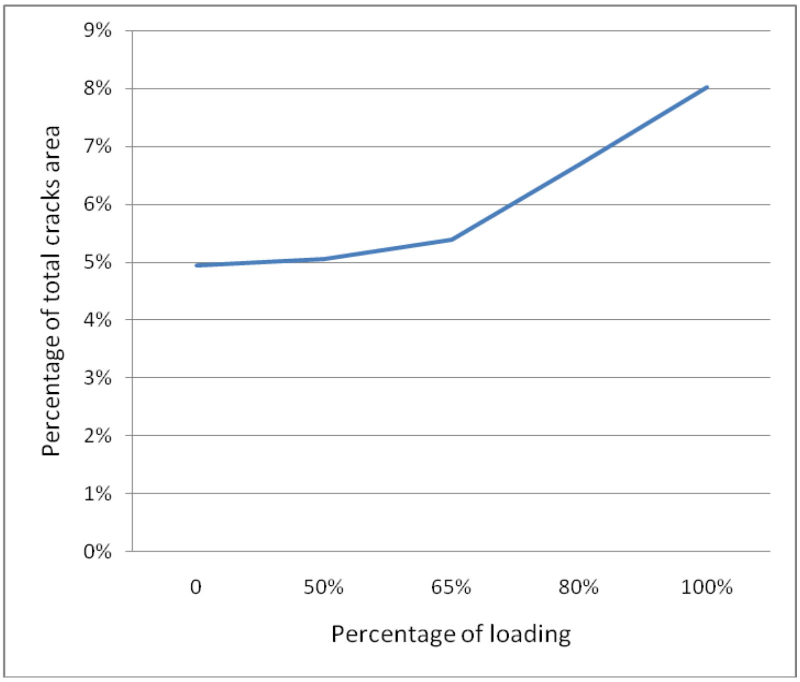

Figure 4.60. Cracks and Voids Area for 0.45 w/c Metakaolin Specimens under Different Loading Levels.

4.6.4 Results of 0.45 w/c Polypropylene Concrete Mixes

In Figure 4.61 the images obtained at various loading for the Polypropylene sample of 0.45 w/c ratio is demonstrated.

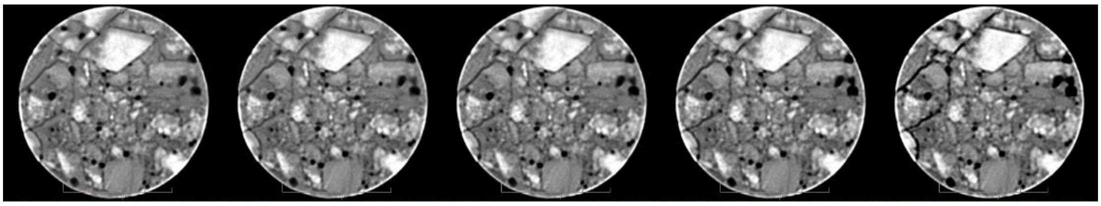

0% σ_c 50% σ_c 65% σ_c 80% σ_c 100% σ_c

Figure 4.61. CT scans for 0.45 w/c ratio, Polypropylene specimen at different loading levels.

Upon scanning all 0.45 w/c ratio samples, these 2D CT images were transferred to AutoCAD software to identify the sizes of porosities, cracks and air voids within the specimen. Figure 4.62 represents the AutoCAD models for 0.45 w/c ratio, Polypropylene specimen.

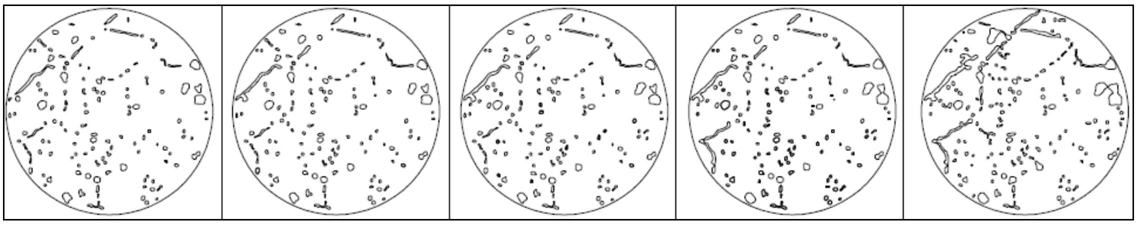

0% σ_c | 50% σ_c | 65% σ_c | 80% σ_c | 100% σ_c

Figure 4.62. AutoCAD models obtained from 2D CT Scans for 0.45 w/c ratio, Polypropylene Specimen at different loading levels.

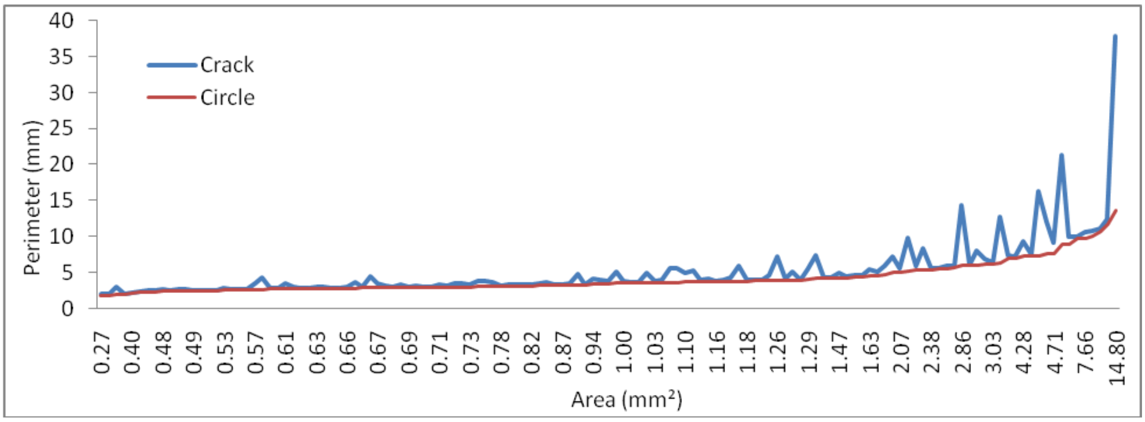

Figure 4.63. Sizes of Pores and Cracks of 0.45 w/c Polypropylene Specimens Before Loading.

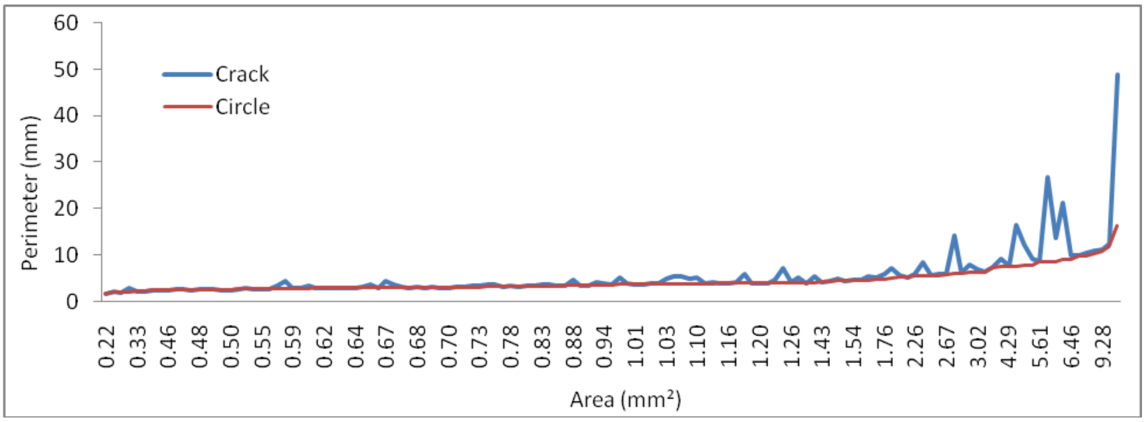

Figure 4.64. Sizes of Pores and Cracks of 0.45 w/c Poly-Propylene Specimens at 50%σc Loading Level.

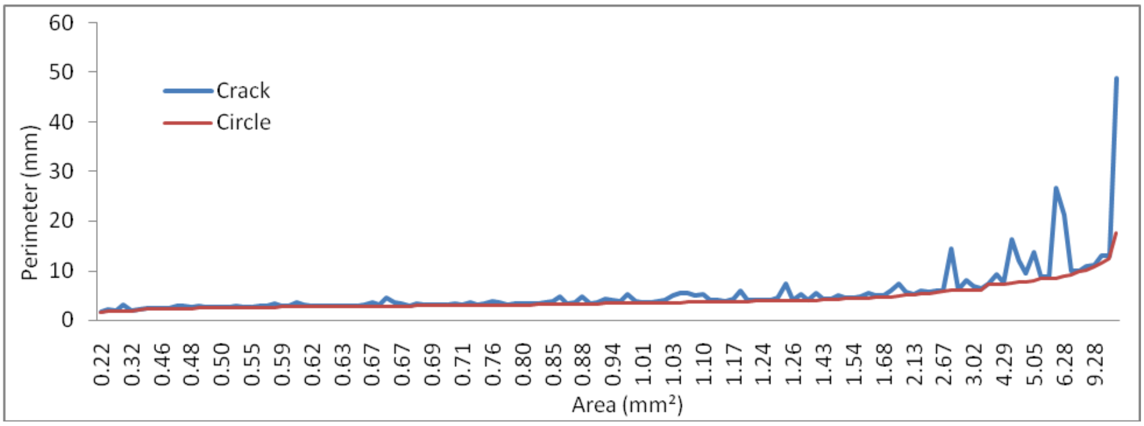

Figure 4.65. Sizes of Pores and Cracks of 0.45 w/c Polypropylene Specimens at 65%σc Loading Level.

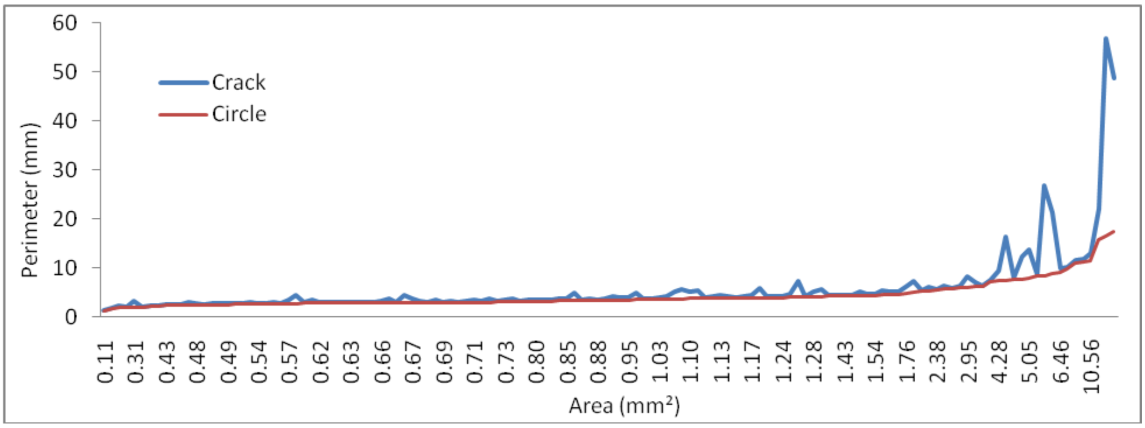

Figure 4.66. Sizes of Pores and Cracks of 0.45 w/c Polypropylene Specimens at 80%σc Loading Level.

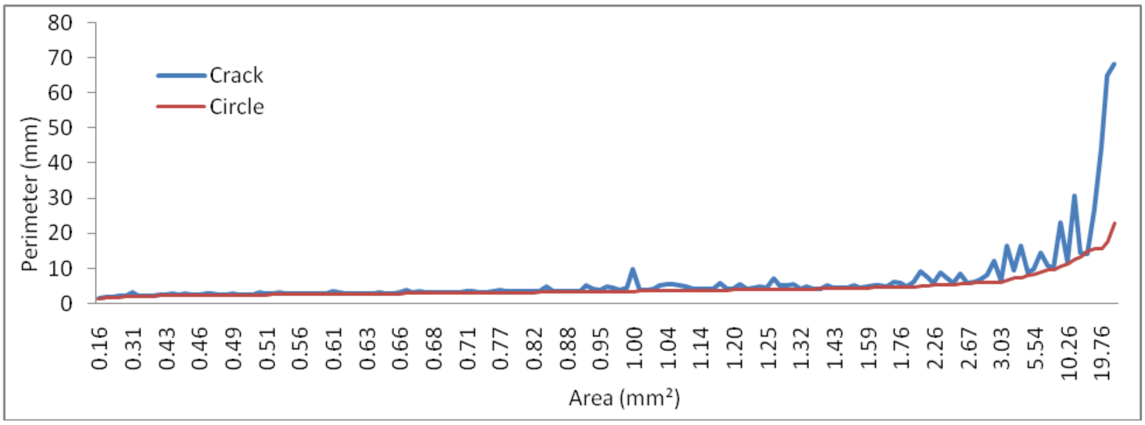

Figure 4.67. Sizes of Pores and Cracks of 0.45 w/c Polypropylene Specimens at 100%σc Loading Level.

4.6.4.1 Crack Size Detection from CT Scans and AutoCAD Images

Upon scanning the samples, these 2D CT images were transferred to AutoCAD software to identify the sizes of porosities, cracks and air voids within the specimen. These measured areas and perimeters are available in a tabular form in below. The increasing the percentage of the crack area can be attributed to crack propagation.

Table 4. 8. Cracks and Air Voids Data Table for 0.45 w/c Polypropylene Specimens.

Percentage of loading	Loading level (MPa)	Total cracks area (mm^2)	Percentage of cracks area	Total perimeter (mm)
0	0	227.83	5.16	687.38
50	16.38	239.03	5.41	704.54
65	21.29	253.91	5.75	725.27
80	26.20	269.22	6.09	747.22
100	32.75	352.94	7.99	945.04

Using the data provided in table 4.8, the following diagram was constructed, representing the loading levels and crack areas and/or perimeter lengths.

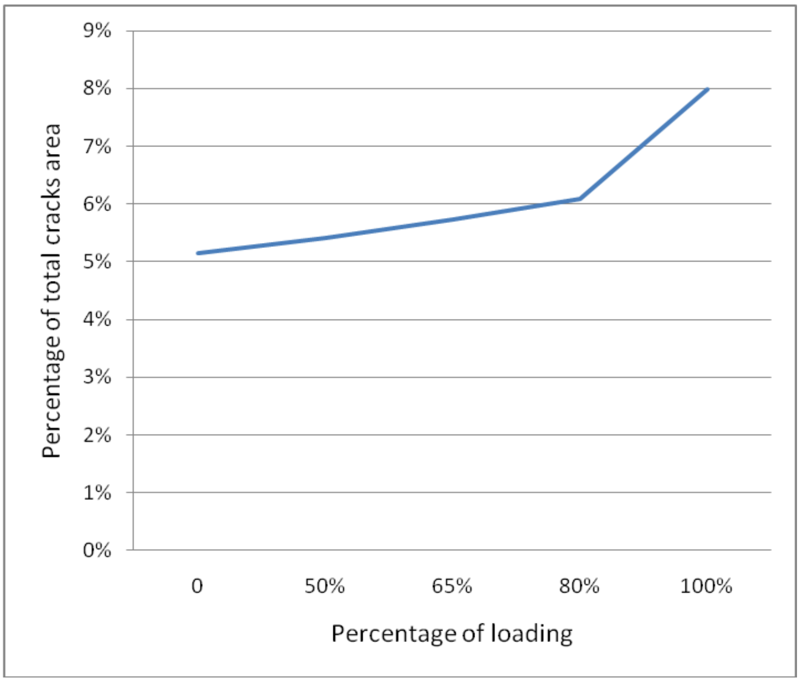

Figure 4.68. Cracks and Voids Area for 0.45 w/c Polypropylene Specimens under Different Loading Levels.

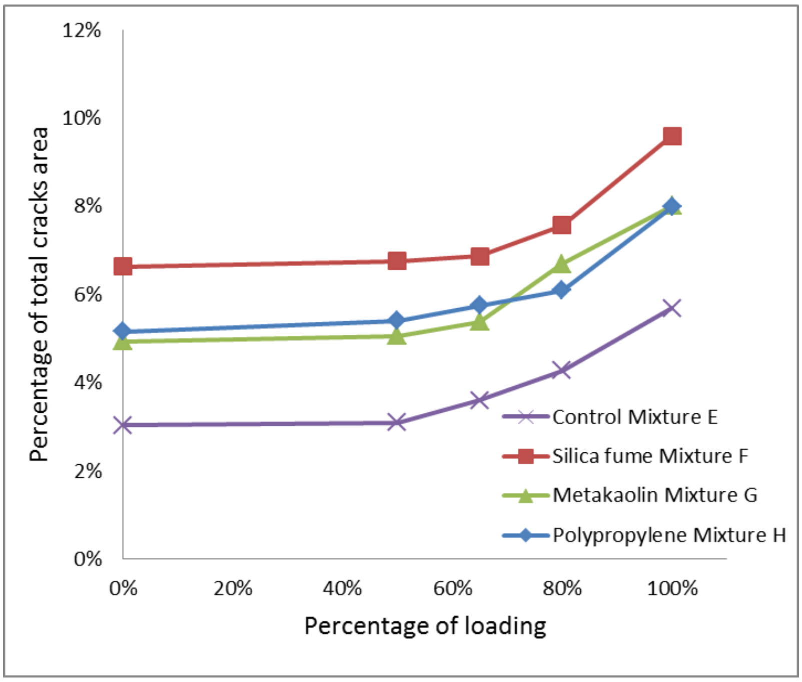

Figure 4.69. % Area of Cracks and Voids w.r.t total X-Sectional Area for 0.45 w/c Mixes under Different Loading Levels.

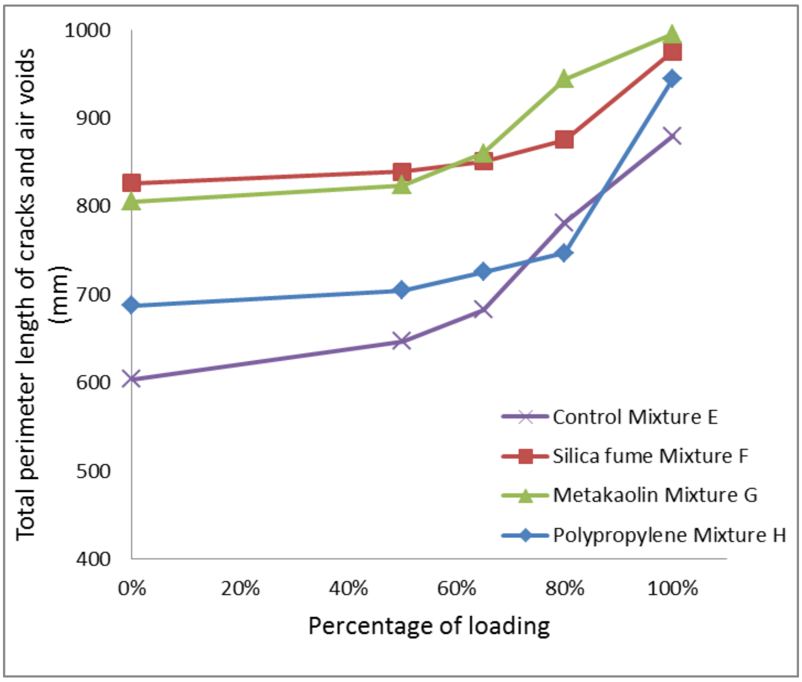

Figure 4.70. Total perimeter lengths of Cracks and Voids of 0.45 w/c Mixes under Different Loading Levels.

4.7 Analysis and Discussion of CT results for 0.45 W/C Ratio Mixes

The total percent voids and cracks with respect to the cross-sectional area relative to the percent of loading are represented in Figure 4.69. As it can be seen from the graph, at zero percent loading, silica fume yields the highest percentage of cracks with 7%, followed by polypropylene and metakaolin approximately 5% and control specimen with the smallest percentage of 3%. Control specimen also has its critical turning point earliest at 50% of loading, metakaolin at 70% and polypropylene and silica fume at 75%.

Beyond this point, cracks in all specimens increased in the same manner. Silica fume mixes showed approximately 10% crack area which is the highest among the others, followed by metakaolin and polypropylene at 8%, and finally control at 5% when the specimens are loaded at 100% of ultimate load.

From these results it can be inferred that for 0.45 w/c ratio, polypropylene has the most quality to prevent crack propagation, because the critical point of polypropylene is higher than that of metakaolin and due to lower total crack than the silica fume. This means that, polypropylene has a positive effect on critical points like interfacial transition zones (ITZ) which are known as the weak zones in materials. In addition, the sharp increment in metakaolin specimens indicates that rapid crack propagation starts earlier due to the accumulated initial cracks and defects in a narrower ITZ. The same situation can be observed for silica fume specimens. Silica fume has a positive effect on the thickness of ITZ. Higher density of defects in a narrower ITZ results in an accelerated crack propagation. This means that mineral additives increase the tensile strength capacity of the material, particularly at the interfacial transition zones.

When the total perimeter length for cracks and air voids are concerned (Figure 4.70), the largest crack perimeter belongs to the silica fume and metakaolin specimens, followed by polypropylene and control at 100% loading. When compared with the % area of cracks, the critical turning point for total perimeter is 80% for silica fume and polypropylene and, 65% for the control and metakaolin specimens. Polypropylene also shows lower perimeter of 700mm at no load point, while the other two (metakaolin and silica fume) start approximately at 820 mm length.

The data on cracks and air voids, related with the area and perimeter length given for each void or crack is tabulated on Figure 4.39 to 4.43, 4.47 to 4.51, 4.55 to 4.59 and 4.63 to 4.67. When we look at the change in perimeter length with changing pore or crack areas, it highly correlates with the conclusions made earlier in this section.

4.8.1 Analysis of 0.35 w/c Control Concrete Mixes

In Figure 4.71 the images obtained at various loading for the control sample (without any additives) of 0.35 w/c ratio is demonstrated. According to the setting of this equipment (computed tomography) all porosities, cracks and air voids were shown with black (due to low density), and materials with high density were shown with white, and the color darkens as the density decreases.

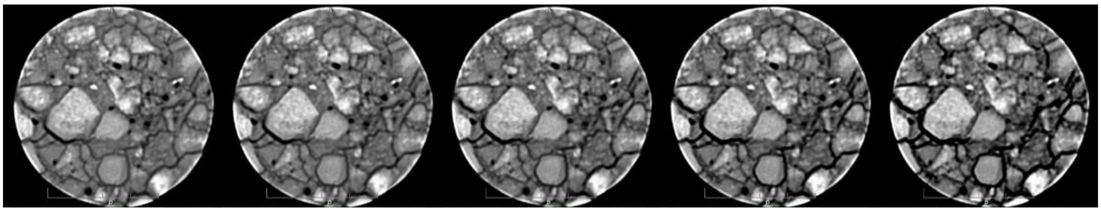

Figure 4.71. CT scans for 0.35 w/c ratio, control specimen at different loading levels.

Upon scanning all 0.35 w/c ratio samples, these 2D CT images were transferred to AutoCAD software to identify the sizes of porosities, cracks and air voids within the specimen (Appendix A). Figure 4.72 represents the AutoCAD models for 0.45 w/c ratio, control specimen.

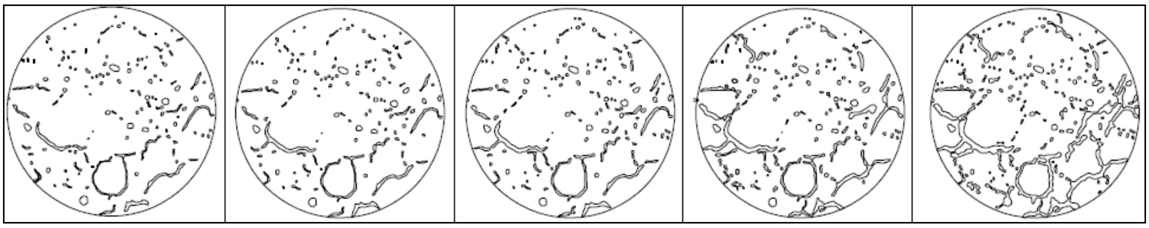

Figure 4.72. AutoCAD models obtained from 2D CT Scans for 0.35 w/c ratio, control specimen at different loading levels.

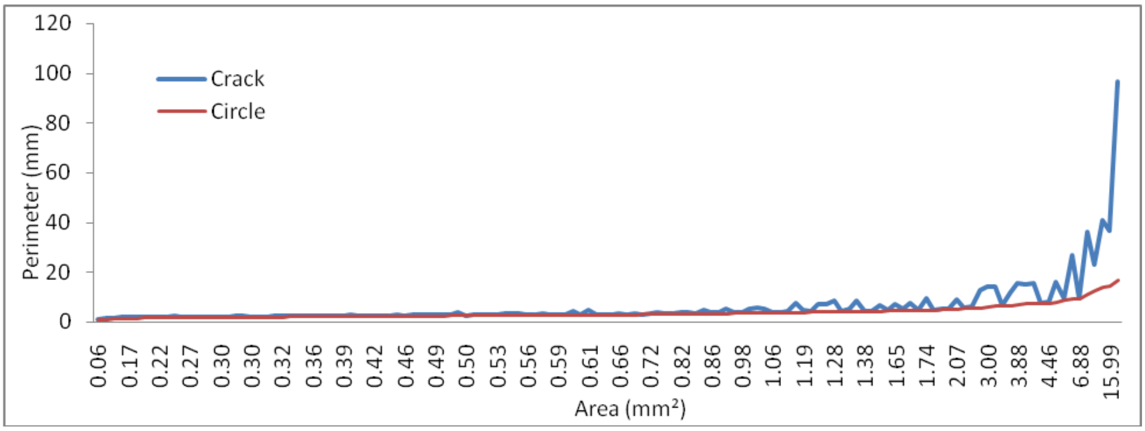

Figure 4.73. Sizes of Pores and Cracks of 0.35 w/c Control Specimens Before Loading.

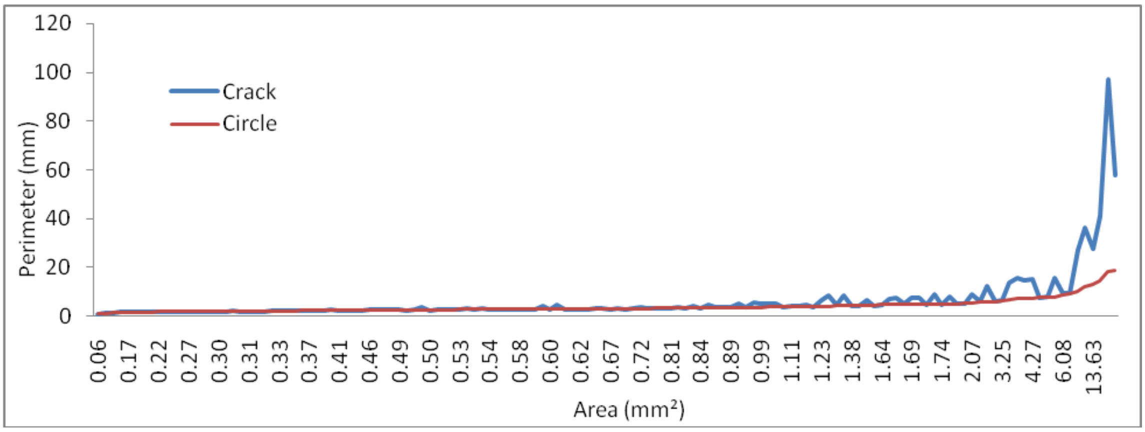

Figure 4.74. Sizes of Pores and Cracks of 0.35 w/c Control Specimens at 50%σc Loading Level.

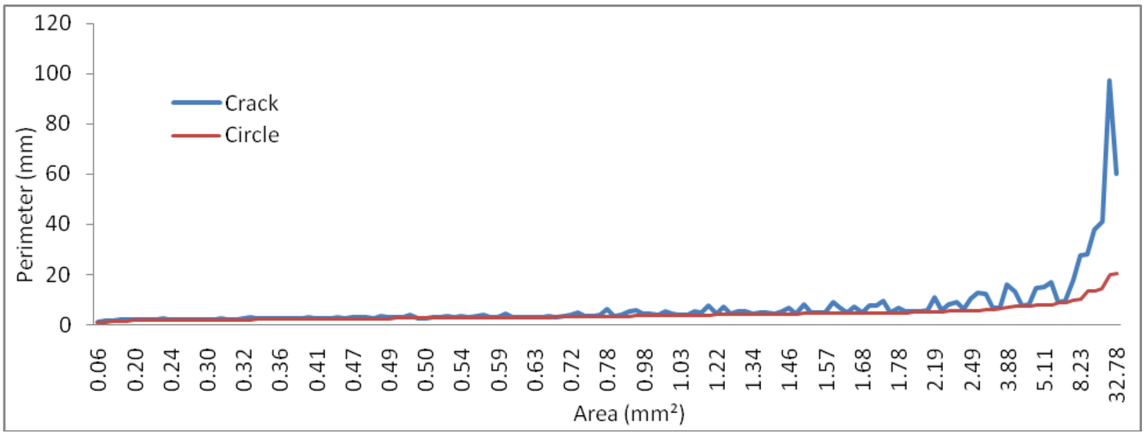

Figure 4. 75. Sizes of Pores and Cracks of 0.35 w/c Control Specimens at 65%σc Loading Level.

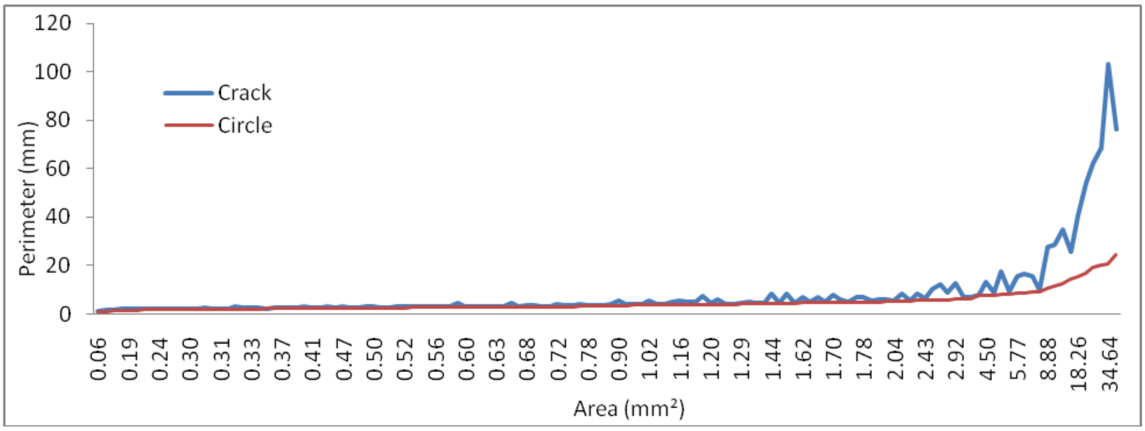

Figure 4. 76. Sizes of Pores and Cracks of 0.35 w/c Control Specimens at 80%σc Loading Level.

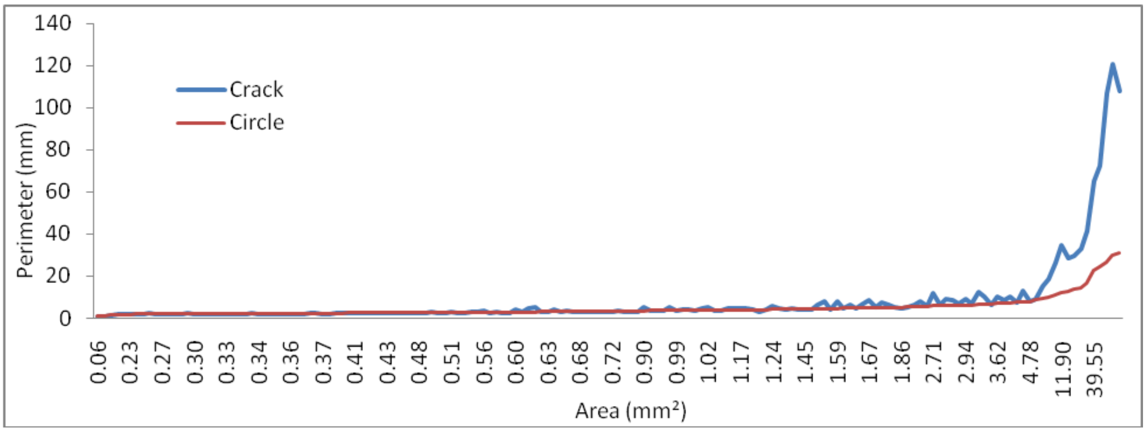

Figure 4.77. Sizes of Pores and Cracks of 0.35 w/c Control Specimens at 100%σc Loading Level.

4.8.1.1 Crack Size Detection from CT Scans and AutoCAD Images

Upon scanning the samples, these 2D CT images were transferred to AutoCAD software to identify the sizes of the black parts which represent porosities, cracks and air voids within the specimen. These measured areas and perimeters are available in a tabular form in below. The increment in the percentage of the crack area can be attributed to crack propagation.

Table 4.9. Cracks and Air Voids Data Table for 0.35 w/c Control Specimens.

Percentage of loading	Loading level (MPa)	Total cracks area (mm^2)	Percentage of cracks area	Total perimeter (mm)
0	0	219.78	4.97	811.82
50	16.82	244.42	5.53	839.97
65	21.87	286.71	6.49	921.34
80	26.91	392.45	8.88	1085.77
100	33.64	547.01	12.38	1310.40

Using the data provided in table 4.9, the following diagram was constructed, representing the loading levels and crack areas and/or perimeter lengths.

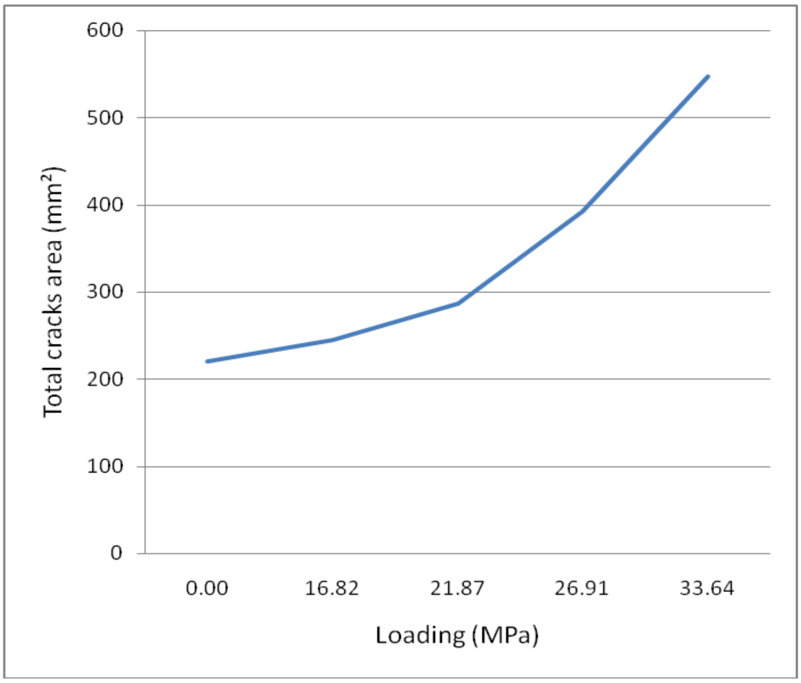

Figure 4.78. Cracks and Voids Area for 0.35 w/c Control Specimens under Different Loading Levels.

4.8.2 Analysis of 0.35 w/c Silica Fume Concrete Mixes

In Figure 4.79 the images obtained at various loading for the silica fume sample of 0.35 w/c ratio is demonstrated.

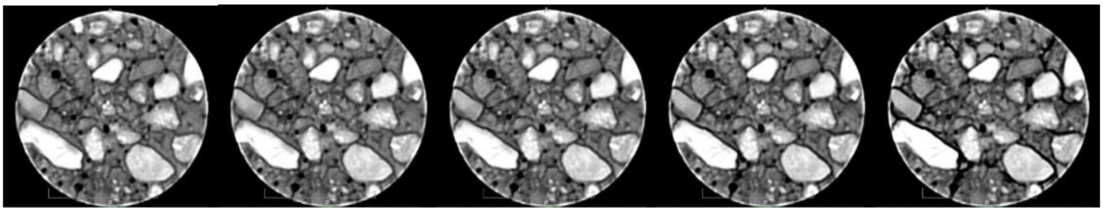

0% σ_c 50% σ_c 65% σ_c 80% σ_c 100% σ_c

Figure 4. 79. CT scans for 0.35 w/c ratio, silica fume specimen at different loading levels.

Upon scanning all 0.35 w/c ratio samples, these 2D CT images were transferred to AutoCAD software to identify the sizes of porosities, cracks and air voids within the specimen (Appendix A). Figure 4.80 represents the AutoCAD models for 0.35 w/c ratio, silica fume specimen.

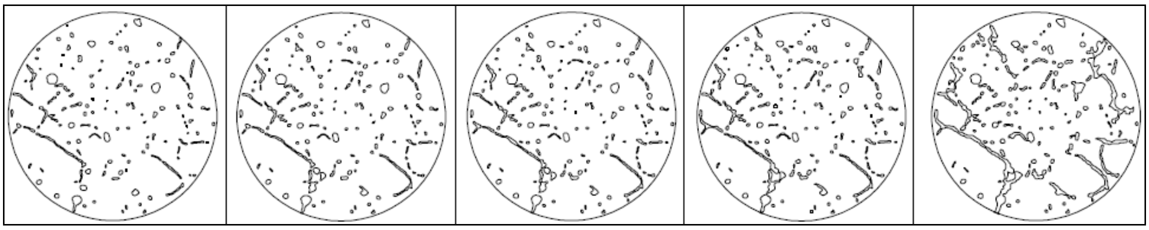

0% σ_c 50% σ_c 65% σ_c 80% σ_c 100% σ_c

Figure 4. 80. AutoCAD models obtained from 2D CT Scans for 0.35 w/c ratio, silica fume specimen at different loading levels.

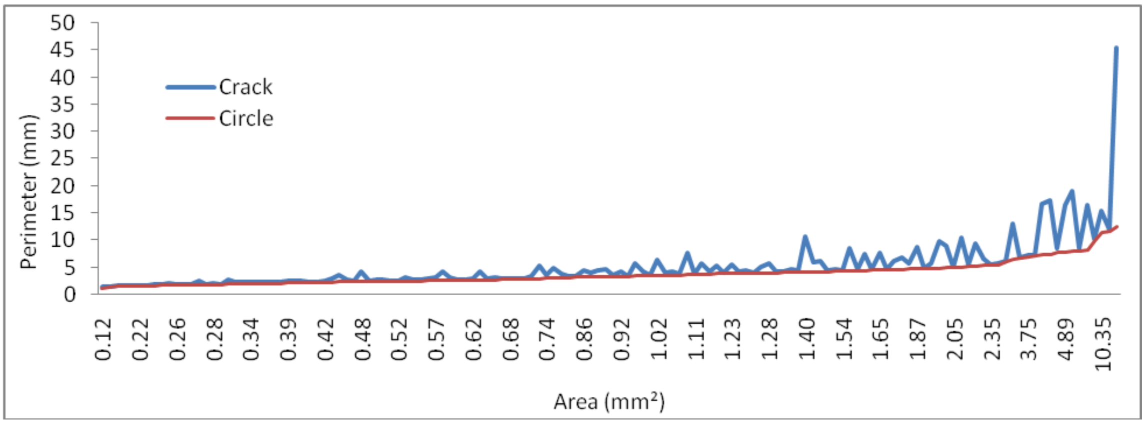

Figure 4.81. Sizes of Pores and Cracks of 0.35 w/c Silica fume Specimens Before Loading.

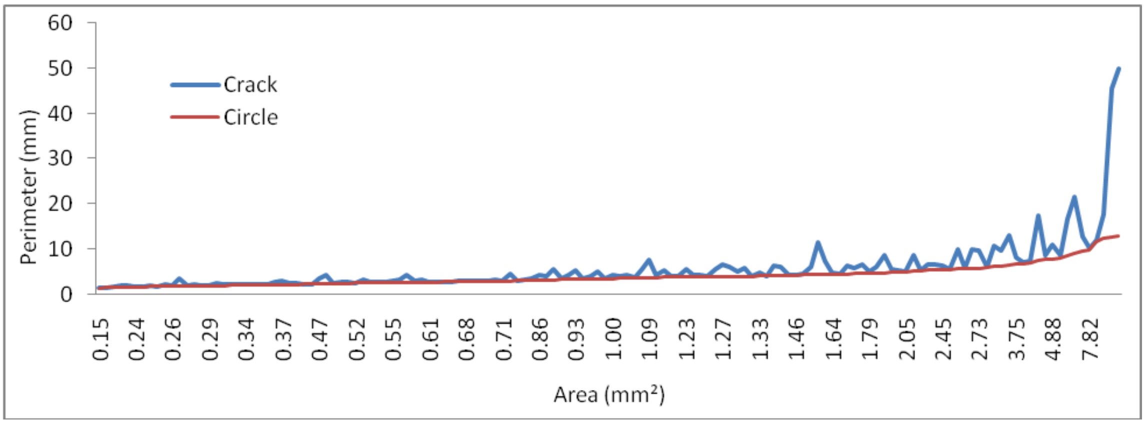

Figure 4.82. Sizes of Pores and Cracks of 0.35 w/c Silica Fume Specimens at 50%σc Loading Level.

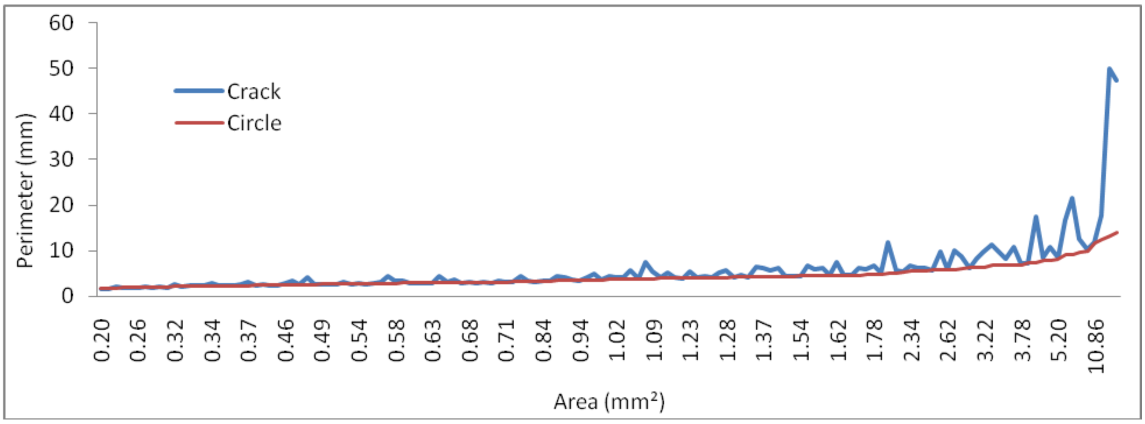

Figure 4.83. Sizes of Pores and Cracks of 0.35 w/c Silica Fume Specimens at 65%σc Loading Level.

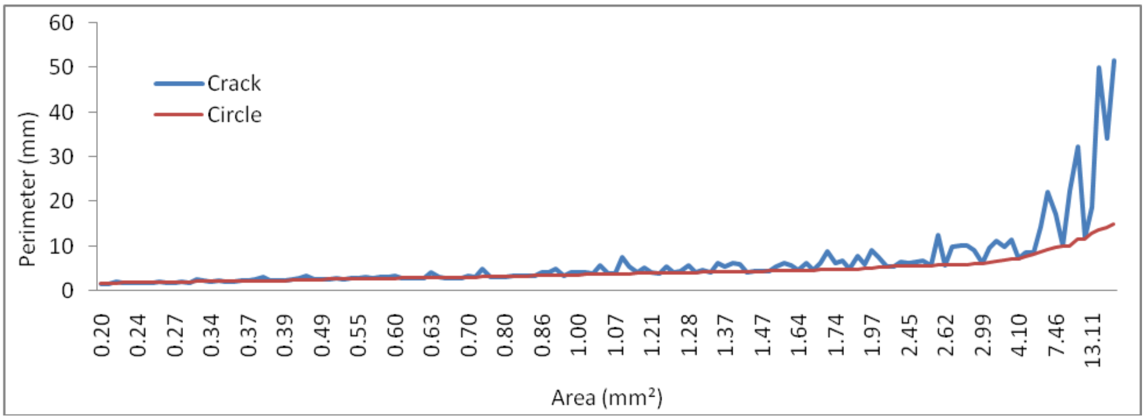

Figure 4.84. Sizes of Pores and Cracks of 0.35 w/c Silica Fume Specimens at 80%σc Loading Level.

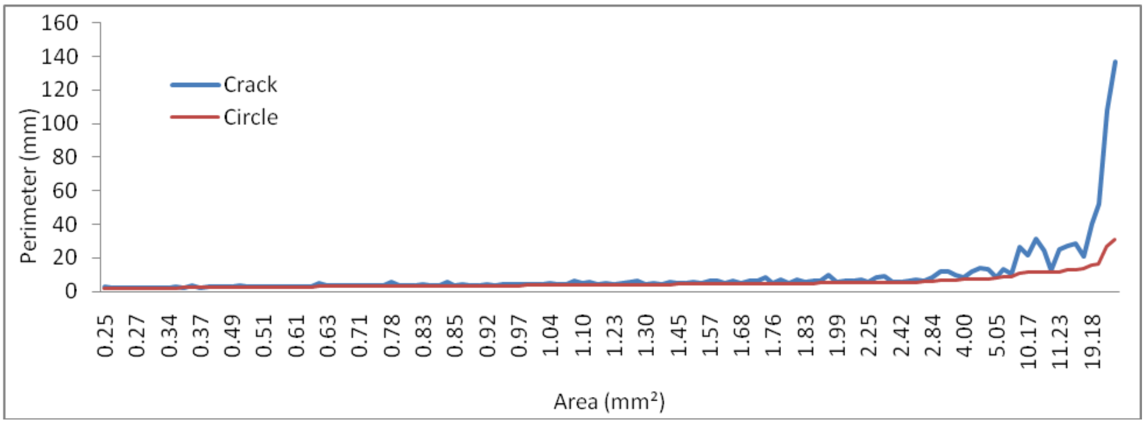

Figure 4.85. Sizes of Pores and Cracks of 0.35 w/c Silica Fume Specimens at 100%σc Loading Level.

4.8.2.1 Crack Size Detection from CT Scans and AutoCAD Images

Upon scanning the samples, these 2D CT images were transferred to AutoCAD software to identify the sizes of the black parts which represent porosities, cracks and air voids within the specimen. These measured areas and perimeters are available in a tabular form in below. The increment in the percentage of the crack area can be attributed to crack propagation.

Table 4.10. Cracks and Air Voids Data Table for 0.35 w/c Silica Fume Specimens.

Percentage of loading	Loading level (MPa)	Total cracks area (mm²)	Percentage of cracks area	Total perimeter (mm)
0	0	205.22	4.65	717.54
50	17.61	240.57	5.45	791.79
65	22.89	247.75	5.61	790.50
80	28.17	278.84	6.31	868.75
100	35.21	447.68	10.13	1105.43

Using the data provided in table 4.9, the following diagram was constructed, representing the loading levels and crack areas and/or perimeter lengths.

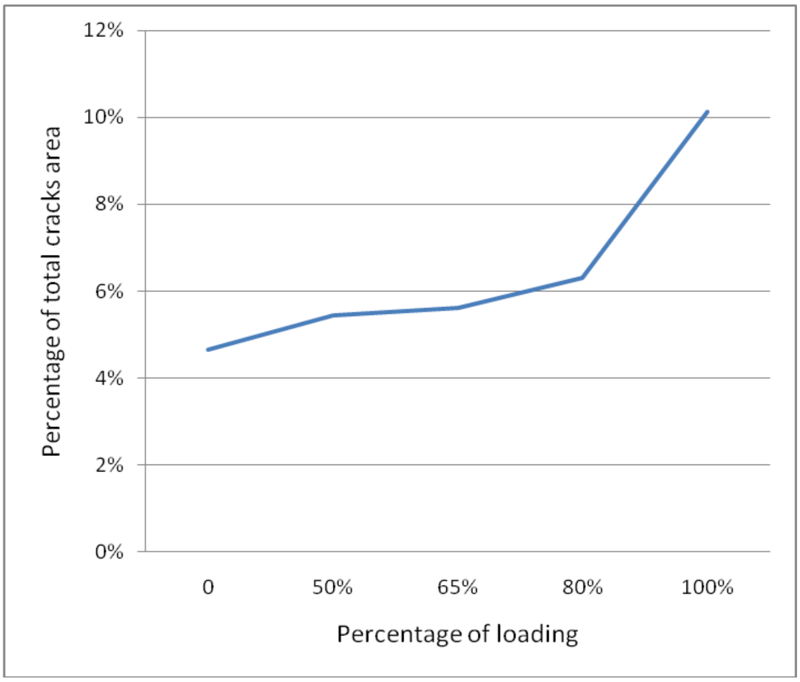

Figure 4.86. Cracks and Voids Area for 0.35 w/c Silica Fume Specimens under Different Loading Levels.

4.8.3 Analysis of 0.35 w/c Metakaolin Concrete Mixes

In Figure 4.87 the images obtained at various loading for the Metakaolin sample of 0.35 w/c ratio is demonstrated.

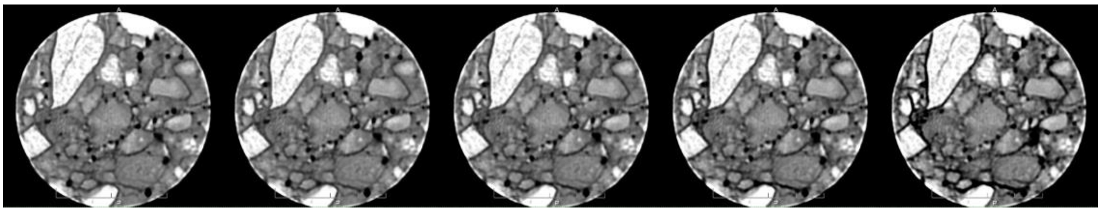

0% σ_c 50% σ_c 65% σ_c 80% σ_c 100% σ_c

Figure 4.87. CT scans for 0.35 w/c ratio, metakaolin specimen at different loading levels.

Upon scanning all 0.35 w/c ratio samples, these 2D CT images were transferred to AutoCAD software to identify the sizes of porosities, cracks and air voids within the specimen (Appendix A). Figure 4.88 represents the AutoCAD models for 0.35 w/c ratio, metakaolin specimen.

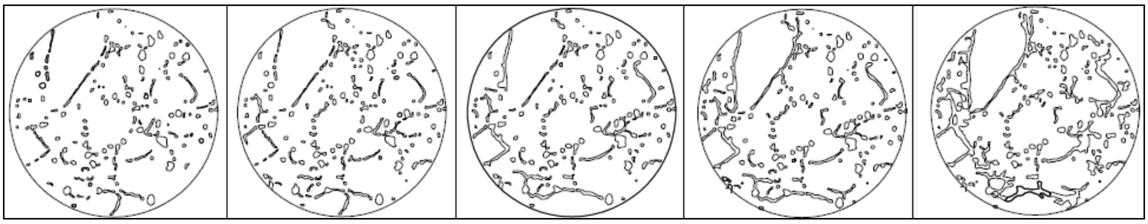

0% σ_c 50% σ_c 65% σ_c 80% σ_c 100% σ_c

Figure 4.88. AutoCAD models obtained from 2D CT Scans for 0.35 w/c ratio, metakaolin specimen at different loading levels.

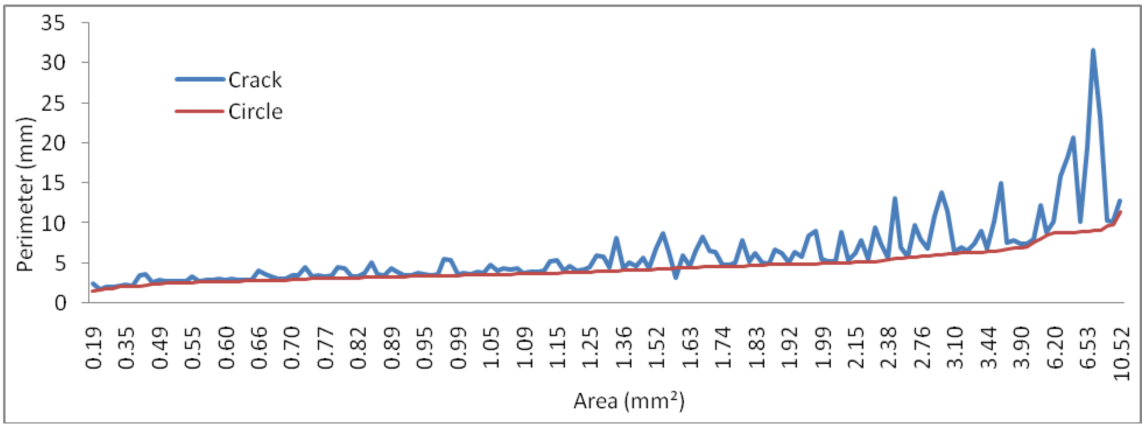

Figure 4.89. Sizes of Pores and Cracks of 0.35 w/c Metakaolin Specimens Before Loading.

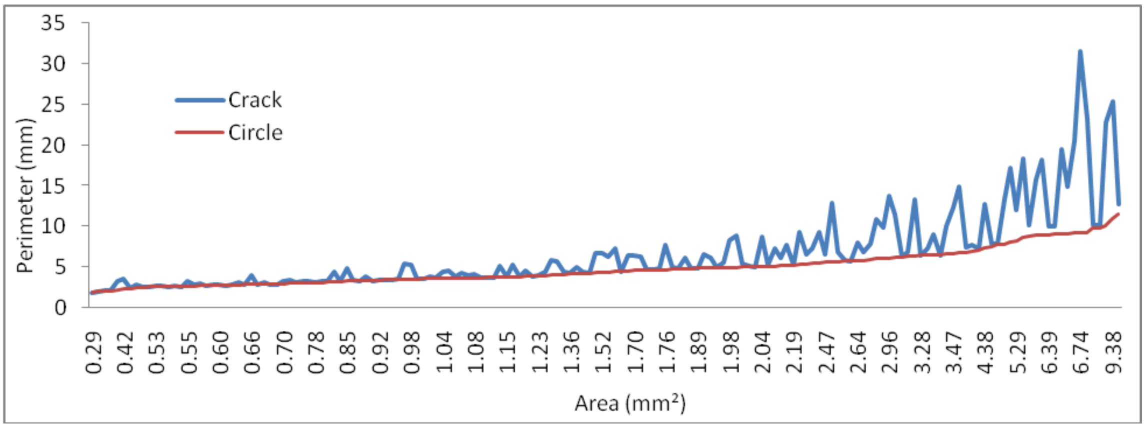

Figure 4.90. Sizes of Pores and Cracks of 0.35 w/c Metakaolin Specimens at 50%σc Loading Level.

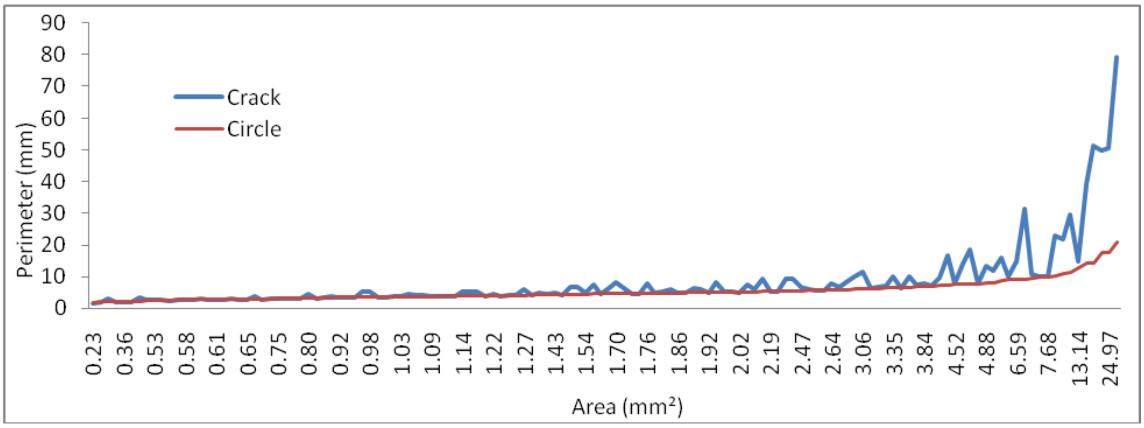

Figure 4.91. Sizes of Pores and Cracks of 0.35 w/c Metakaolin Specimens at 65%σc Loading Level.

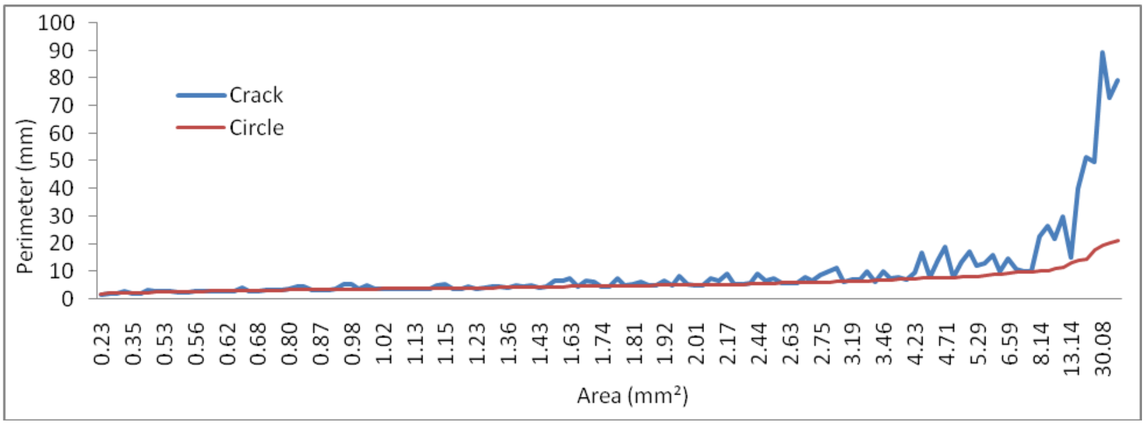

Figure 4.92. Sizes of Pores and Cracks of 0.35 w/c Metakaolin Specimens at 80%σc Loading Level.

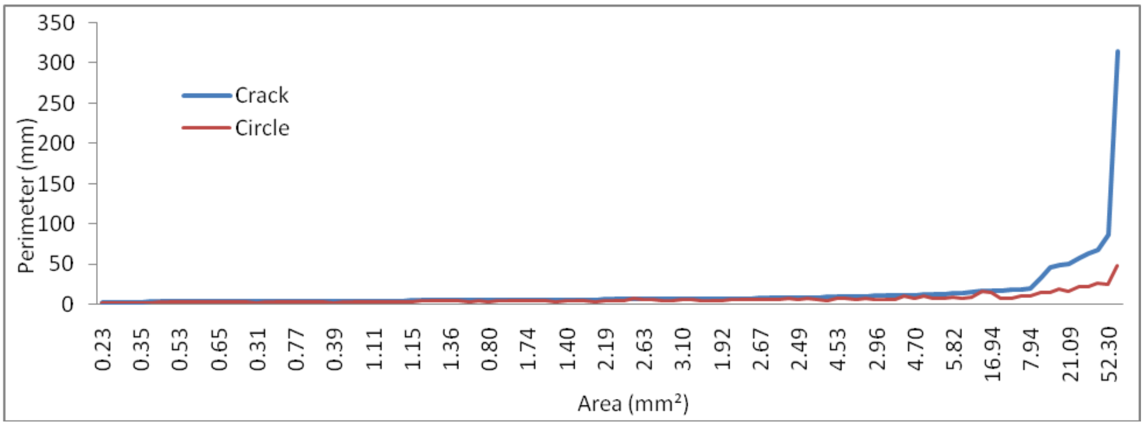

Figure 4.93. Sizes of Pores and Cracks of 0.35 w/c Metakaolin Specimens at 100%σc Loading Level.

4.8.3.1 Crack Size Detection from CT Scans and AutoCAD Images

Upon scanning the samples, these 2D CT images were transferred to AutoCAD software to identify the sizes of the black parts which represent porosities, cracks and air voids within the specimen. These measured areas and perimeters are available in a tabular form in below. The increment in the percentage of the crack area can be attributed to crack propagation.

Table 4.11. Cracks and Air Voids Data Table for 0.35 w/c Metakaolin Specimens.

Percentage of loading	Loading level (MPa)	Total cracks area (mm^2)	Percentage of cracks area	Total perimeter (mm)
0	0	299.96	6.79	936.33
50	19.81	356.06	8.06	1085.61
65	25.75	409.09	9.26	1119.60
80	31.70	454.32	10.28	1228.30
100	39.62	703.55	15.93	1381.06

Using the data provided in table 4.9, the following diagram was constructed, representing the loading levels and crack areas and/or perimeter lengths.

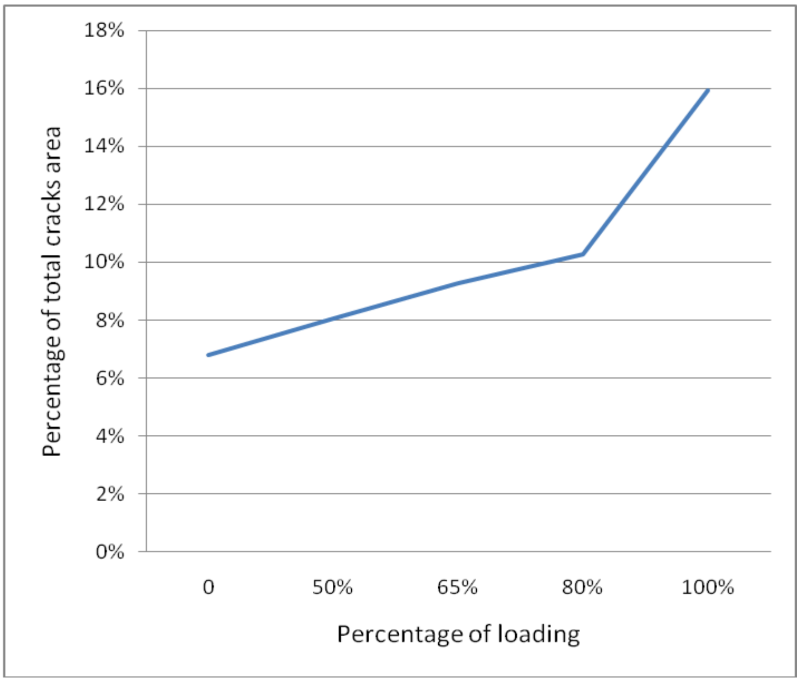

Figure 4.94. Cracks and Voids Area for 0.35 w/c Metakaolin Specimens under Different Loading Levels.

4.8.4 Results of 0.35 w/c Polypropylene Concrete Mixes

In Figure 4.95 the images obtained at various loading for the Polypropylene sample of 0.35 w/c ratio is demonstrated.

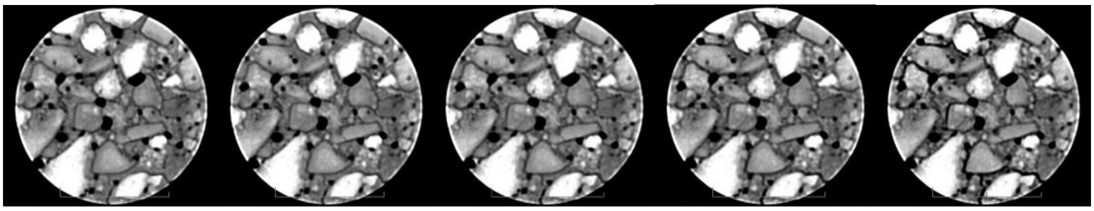

0% σ_c 50% σ_c 65% σ_c 80% σ_c 100% σ_c

Figure 4.95. CT scans for 0.35 w/c ratio, Polypropylene specimen at different loading levels.

Upon scanning all 0.35 w/c ratio samples, these 2D CT images were transferred to AutoCAD software to identify the sizes of porosities, cracks and air voids within the specimen (Appendix A). Figure 4.96 represents the AutoCAD models for 0.35 w/c ratio, polypropylene specimen.

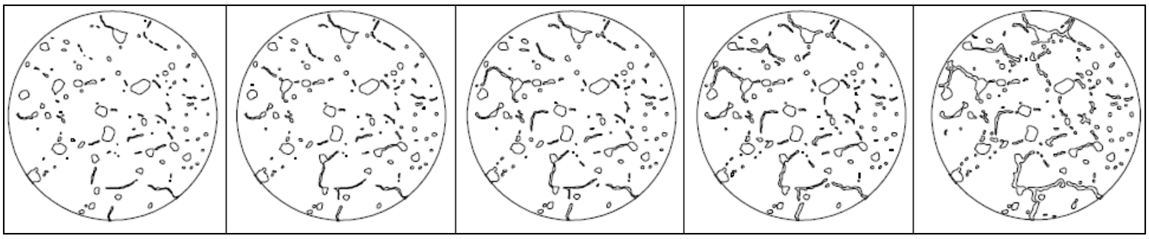

0% σ_c 50% σ_c 65% σ_c 80% σ_c 100% σ_c

Figure 4.96. AutoCAD models obtained from 2D CT Scans for 0.35 w/c ratio, Polypropylene specimen at different loading levels.

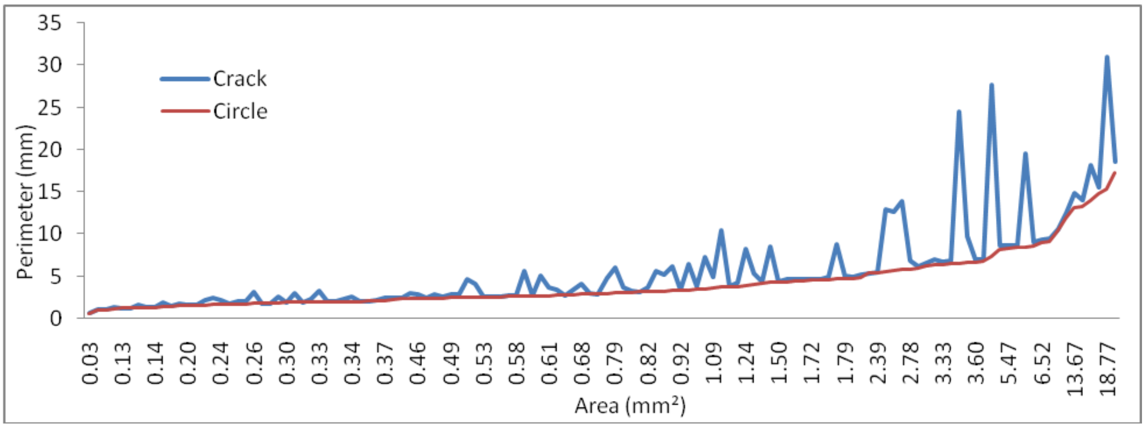

Figure 4.97. Sizes of Pores and Cracks of 0.35 w/c Polypropylene Specimens Before Loading.

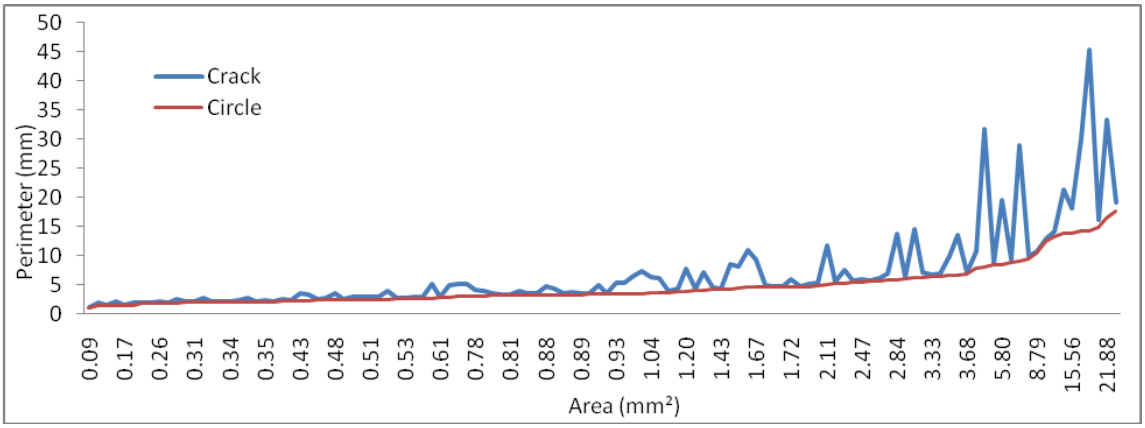

Figure 4.98. Sizes of Pores and Cracks of 0.35 w/c Polypropylene Specimens at 50%σc Loading Level.

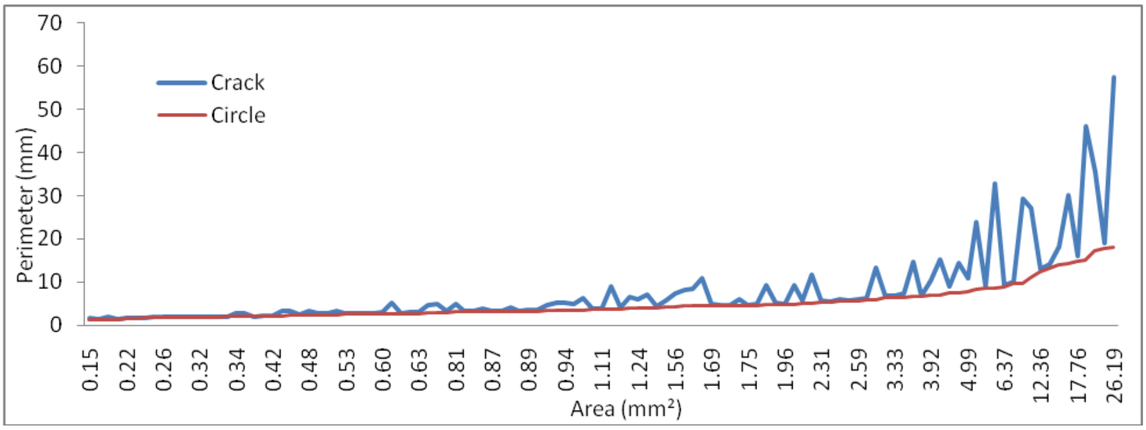

Figure 4.99. Sizes of Pores and Cracks of 0.35 w/c Polypropylene Specimens at 65%σc Loading Level.

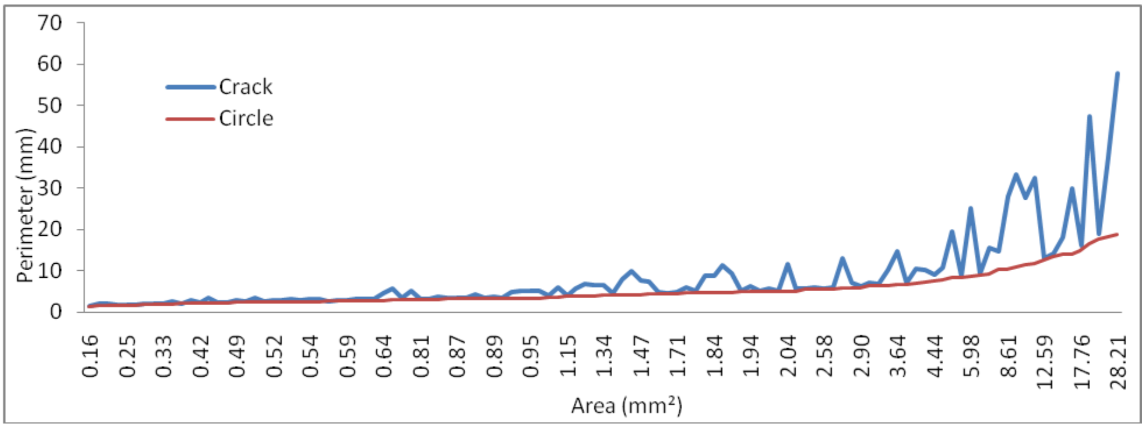

Figure 4.100. Sizes of Pores and Cracks of 0.35 w/c Polypropylene Specimens at 80%σc Loading Level.

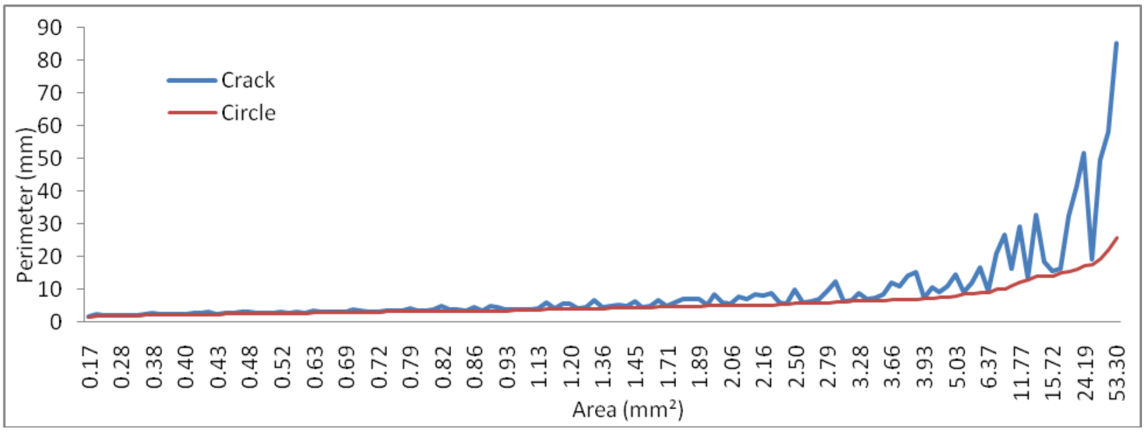

Figure 4.101. Sizes of Pores and Cracks of 0.35 w/c Polypropylene Specimens at 100%σc Loading Level.

4.8.4.1 Crack Size Detection from CT Scans and AutoCAD Images

Upon scanning the samples, these 2D CT images were transferred to AutoCAD software to identify the sizes of the black parts which represent porosities, cracks and air voids within the specimen. These measured areas and perimeters are available in a tabular form in below. The increment in the percentage of the crack area can be attributed to crack propagation.

Table 4.12. Cracks and Air Voids Data Table for 0.35 w/c Polypropylene pecimens.

Percentage of loading	Loading level (MPa)	Total cracks area (mm^2)	Percentage of cracks area	Total perimeter (mm)
0	0	277.41	6.28	704.04
50	17.36	318.82	7.22	800.02
65	22.57	345.49	7.82	872.58
80	27.78	384.00	8.69	945.66
100	34.72	511.81	11.59	1121.81

Using the data provided in table 4.12, the following diagram was constructed, representing the loading levels and crack areas and/or perimeter lengths.

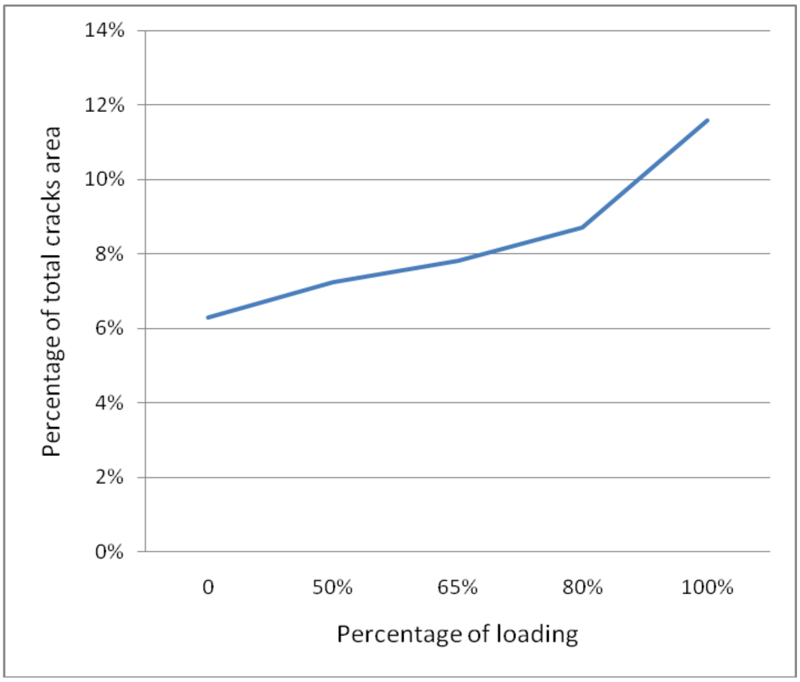

Figure 4.102. Cracks and Voids Area for 0.35 w/c Polypropylene Specimens under Different Loading Levels.

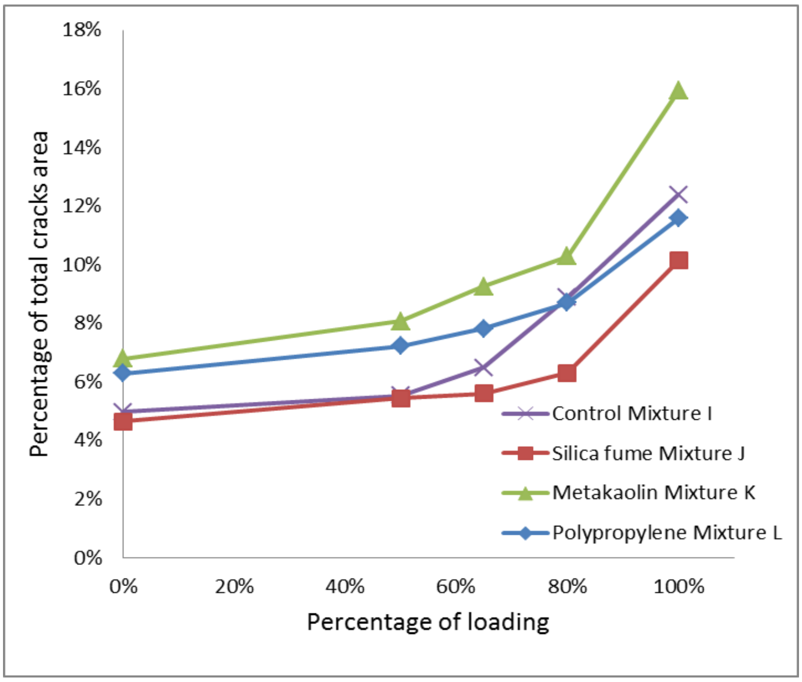

Figure 4.103. % Area of Cracks and Voids w.r.t total X-Sectional Area for 0.35 w/c Mixes under Different Loading Levels.

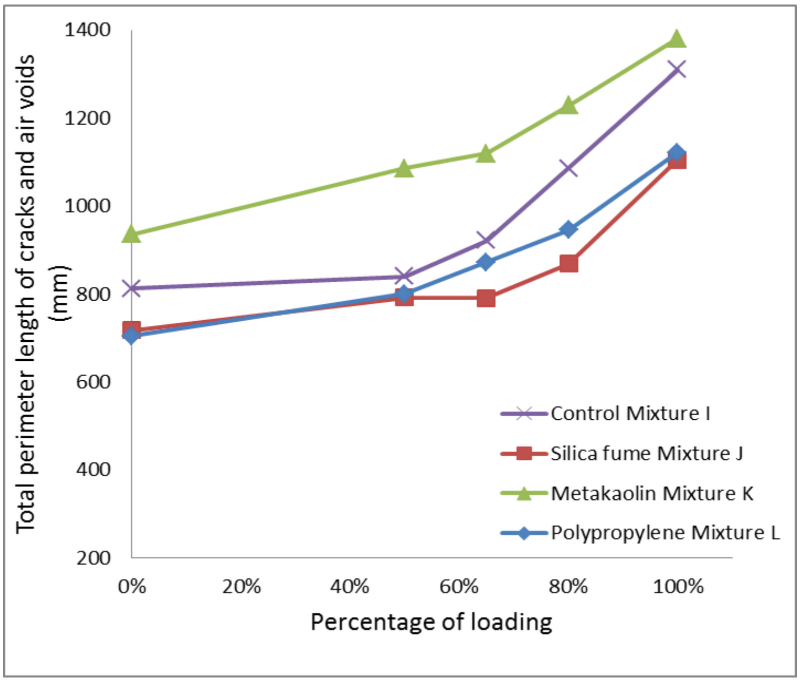

Figure 4.104. Total perimeter lengths of Cracks and Voids of 0.35 w/c Mixes under Different Loading Levels.

4.9 Analysis and Discussion of CT results for 0.35 W/C Ratio Mixes

The total percent voids and cracks with respect to the cross-sectional area relative to the percent of loading are represented in Figure 4.103. As it can be seen from the graph, at zero percent loading, metakaolin yields the highest percentage of cracks with 6.6%, followed by polypropylene at 6% and metakaolin and control specimen at approximately 4.4%. Similar to 0.45 w/c ratio, for 0.35 w/c ratio as well, the control specimen also has its critical turning point earliest at 50% of loading. Although metakaolin starts showing a significant increase in % crack area at around 50% to 80% of loading, the most steep increase begins at 80%, same as silica fume and polypropylene.

There is approximately 8% difference between crack areas of metakaolin added specimen and silica fume added specimens, indicating that silica fume is the most effective additive in preventing crack propagation while metakaolin shows the least effect.

This means that, for this w/c ratio, silica fume has a positive effect on critical points like interfacial transition zones (ITZ) which are known as the weak zones in materials. In addition, the sharp increment in metakaolin specimens indicates that rapid crack propagation starts earlier due to the accumulated initial cracks and defects in a narrower ITZ. The same situation can be observed for polypropylene specimens. Polypropylene has a positive effect both on the density of initial cracks and their propagations. This means that some mineral additives increase the tensile strength capacity of the material, particularly at the interfacial transition zones.

When the total perimeter length for cracks and air voids are concerned (Figure 4.104), the largest crack perimeter belongs to the metakaolin followed by silica fume and polypropylene. All three additive-including specimens showed the same critical turning point at 60% of the loading.

The data on cracks and air voids, related with the area and perimeter length given for each void or crack is tabulated on Figure 4.73 to 4.77, 4.81 to 4.83, 4.89 to 4.93 and 4.97 to 4.101. When we look at the change in perimeter length with changing pore or crack areas, it highly correlates with the conclusions made earlier in this section.

Chapter 5

CONCLUSION

In this thesis, concreted mixes were produced using three different admixtures at three different water/cement ratios. The effects of w/c ratio and mineral additives on compressive strength and microcracking behavior of concrete were investigated. Following, conclusions obtained from compressive strength test and CT method.

1. The compressive strength of the mixes with replacements and admixtures were slightly higher than that of the control specimen.

2. The positive effect of metakaolin was found to increase with decreasing w/c ratio. Although same conclusion can be made for all three admixtures, the highest rate of increase in strength was in metakaolin, and the polypropylene had the lowest increment rate.

3. When the w/c ratios are considered separately, 0.55 ratio stands out in terms of the additive-strength relationship. While in 0.45 and 0.35 w/c ratios the strength increases with the order of silica fume, polypropylene and metakaolin added mixtures, this order changes to metakaolin, polypropylene and silica fume in 0.55 w/c ratio specimens.

4. For 0.55 w/c ratio mixes, the critical turning point for rapid crack propagation is 60% of loading for the control specimen and 80% of loading for the other

mixes. Beyond this point, control shows a sharp increment and reaches approximately 14% crack area, followed by silica fume at 9%, metakaolin at 8% and finally polypropylene at 7% when the specimens are loaded at 100%.

5. Mineral additives increase the tensile strength capacity of the material, particularly at the interfacial transition zones. For 0.55 W/C ratio mixes, polypropylene was found to be the best of all three additives in preventing crack propagation

6. For 0.45 w/c ratio, at zero percent loading, silica fume yields the highest percentage of cracks with 7%, followed by polypropylene and metakaolin at approximately 5% and control specimen with the smallest percentage of 3%. Control specimen also has its critical turning point earliest at 50% of loading, metakaolin at 70% and polypropylene and silica fume at 75%.

7. Polypropylene was found to have the most quality to prevent crack propagation in 0.45 w/c ratio, because the critical point of polypropylene is higher than that of metakaolin and due to lower total crack than the silica fume. Polypropylene has a positive effect on critical points like interfacial transition zones (ITZ) which are known as the weak zones in materials. In addition, the sharp increment in metakaolin specimens indicates that rapid crack propagation starts earlier due to the accumulated initial cracks and defects in a narrower ITZ.

8. In 0.45 w/c ratio mixes, silica fume has a positive effect on the thickness of ITZ. Higher density of defects in a narrower ITZ results in an accelerated

crack propagation. This means that mineral additives increase the tensile strength capacity of the material, particularly at the interfacial transition zones.

9. For 0.35 w/c ratio mixes, at zero percent loading, metakaolin yields the highest percentage of cracks with 6.6%, followed by polypropylene at 6% and metakaolin and control specimen at approximately 4.4%. Similar to 0.45 w/c ratio, for 0.35 w/c ratio as well, the control specimen has its critical turning point earliest at 50% of loading.

10. For 0.35 w/c ratio mixes, silica fume has a positive effect on critical points like interfacial transition zones (ITZ) which are known as the weak zones in materials. In addition, the sharp increment in metakaolin specimens indicates that rapid crack propagation starts earlier due to the accumulated initial cracks and defects in a narrower ITZ.

11. Polypropylene was determined to have the steadiest behavior both on the presence of initial cracks and their propagations.

12. In general, it can be concluded that for 0.45 and 0.55 w/c cement ratios, the best additive in preventing crack propagation is polypropylene and for the lowest water w/c ratio (0.35) it is silica fume. However, silica fume was found to have the least positive effect in 0.45 w/c ratio mixes while for 0.35 and 0.55 w/c ratios, the least effect was caused from metakaolin, although it gave the highest compressive strength.

13. For normal w/c ratios polypropylene gives us the best results and for low w/c ratios best results are given from silica fume.

REFERENCES

[1] Akcaoglu, T., Tokyay, M., Celik, T, (2004); “Effect of Coarse Aggregate Size and Matrix Quality on ITZ and Failure Behaviour of Concrete Under Uniaxial Compression”, *Cement and Concrete Composites*, Vol. 26(6), pp. 633-638.

[2] Akcaoglu, T., Tokyay, M., Celik, T, (2005); “Assessing the ITZ Microcracking via Scanning Electron Microscope and Its Effect on the Failure Behaviour of Concrete”*Cement and Concrete Research*, Vol. 35, pp. 358-363.

[3] http://www.holcim.com.au/products-and-services/tools- faqs- and- resources/do-it- yourself- diy/cracks- in- concrete. Html.

[4] University of Memphis. Designing and Proportioning Normal Concrete Mixtures.

[5] D C Teychenne, J C Nicholls, R E Franklin, D W Hobbs. Design of normal concrete mixes.

[6] http://www.engineeringtoolbox.com/concrete-properties-d_1223.html.

[7] T. Suzuki, M. Aoki& M. Ohtsu .Damage identification of cracked concrete by X-Ray computed tomography method.

[8] Li, F., & Li, Z., (2000), Acoustic Emission Monitoring of Fracture of Fiber Reinforced Concrete in Tension, *ACI Materials Journal*, Vol.97, No.6, Nov.-Dec., pp.629- 636.

[9] Li, Z., Kulkarni, S.M., & Shah, S.P., (1993), New Test Method for Obtaining Softening Response of Unnotched Concrete Specimen under Uniaxil Tension, Experimental Mechanics, Vol. 33, No. 3, pp.181-188.

[10] Jenq, Y., Shah, S.P., (1991), Features of Mechanics of Quasi-Brittle Crack Propagation in Concrete, *International Journal of Fracture* 51: 103-120.

[11] Shum, K.M., & Hutchinson, J.W., (1990), On Toughening by Micro-Cracks, Mechanics of Materials, Vol. 9, pp.83-91.

[12] Shah, S. P., & Sankar, R., (1987), Internal Cracking and Strain Softening Response of Concrete under Uniaxial Compression, *Journal of American Concrete Institute*, pp.200-212.

[13] Ueda, M., Hasebe, N., Sato, M., & Okuda, H., (1994), Fracture Mechanism of Plain Concrete Under Uniaxial Tension, Concrete Library of JSCE, No. 24, Dec., pp.31-45.

[14] Hearn, H., (1999), Effect of Shrinkage and Load-Induced Cracking on Water Permeability of Concrete, *ACI Material Journal*, March-April, pp.234-240.

[15] Shah, S. P., & Sankar, R., (1987), Internal Cracking and Strain Softening Response of Concrete under Uniaxial Compression, *Journal of American Concrete Institute*, pp.200-212.

[16] Hsu, T.T.C., Slate, F., Sturman, G., & Winter, G., (1963), Microcracking of Plain Concrete and the Shape of the stress-Strain Curve, *Journal of American Concrete Institute*, 60, pp.209-224.

[17] Bascoul, A., (1996)., State of the art report – Part 2: Mechanical micro-cracking of concrete, *Materials and Structures,* Vol. 29, March, pp. 67-78.

[18] Alshibli, K. A., Batiste, S.N., Swanson, R. A., Sture, S., Costes, N. C., & Lankton, M. (2000a) "Quantifying Void Ratio Variation in Sand Using Computed Tomography", *Geotechnical Measurements: Lab and Field, Geotechnical Special Publication No. 106, Proceedings of Geo-Denver* 2000, pp. 30-43.

[19] Alshibli, K. A., Sture, S., Costes, N. C., Frank, M., Lankton, M., Batiste, S., & Swanson, R. (2000b) "Assessment of Localized Deformations in Sand Using x-ray Computed Tomography", *ASTM Geotechnical Testing Journal*, Vol. 23, No. 3, pp. 274-299.

[20] Pla-Rucki, G. & Eberhard, M. (1995). "Imaging of Reinforced Concrete: State of the Art Review". *Journal of Infrastructure Systems*. Vol. 1, No. 2, pp. 134-141.

[21] Braz, D., Da Motta, L. M. G. & Lopes, R. T. (1999). Computed tomography in the fatigue test analysis of an asphaltic mixture. Applied Radiation and Isotopes, Appl. Radiat. Isot., Vol. 50, No. 4, pp. 661-671.

[22] Masad, E., Jandhyala, V. K., Dasgupta, N., Somadevan, N., Shashidhar, N. (2002). "Characterization of Air Void Distribution in Asphalt Mixes Using X-Ray

Computed Tomography. *Journal of Materials in Civil Engineering*. Vol.14, No.2, pp 122-129.

[23] Wang, L. B. (2003). “Characterization of Asphalt Concrete using X-ray Tomography”. First International Workshop on X-ray CT for Geomaterials, Soils, Concrete and Rock. Edited by J. Otani and Y. Obara, Kumamoto, Japan.

[24] Al-Raoush, R. I. & Willson, C. S. (2004). “Extraction of Physically-Realistic Pore Network Properties from Three-Dimensional Synchrotron X-ray Microtomography Images of Unconsolidated Porous Media Systems”. *Journal of Hydrology* (accepted for publication).

[25] Al-Omari, A. & Masad, E. (2004). “Three Dimensional Simulation of Fluid Flow in Granular Material Material Microstructure”. *GeoJordan 2004*. Edited by K. Alshibli, A. Malkawi, & M. Alsaleh. July 12-13, 2004. Amman, Jordan. ASCE Press. Reston, VA. pp. 177-190.

[26] ACI Library , “Fiber Reinforced Concrete” , concrete international , V7 , No.3 , march , 1985 , pp . 64-65

[27] Neville, A, M., & Brooks, J.J., (1987), *Concrete Technology*, Revised Edition-2001 Standards Update, Prentice Hall, Longman Group UK Limited, 438pp.

[28] Gambhir, M.L., (1990), Concrete Technology, 2nd Reprint, Tata MeGrae-Hill Publishing Company Limited, New Delhi, 318 pp.

[29] Billmeyer, F. W., Jr., (1984), "Textbook of Polymer Science," John Wiley & Sons, Inc.

[30] Zollo, R. F., (1985), "Glass, Natural, and Synthetic Fiber Uses in Fiber Concrete," In Report SCM-10 (85): Design with Fiber Reinforced Concrete, *American Concrete Institute*, Chicago, IL, Pg. 376-396.

[31] Pawade Prashant.Y, Nagarnaik P.B, Pande A.M, (2011),Influence of Silica fume in enhancement of compressive strength, flexural strength of steel fibers concrete and their relationship, *International Journal of Civil and Structural Engineering* ,Volume 2, No 1.

[32] Silica Fume Association, (2005): Silica fume manual.38860 Sierra Lane, Lovettsville, VA 20180, USA.

[33] Sandvik, M., Gjorv, O.E. (1992): Prediction of strength development for silica fume concrete. Proceedings of 4th International Conference on the Use of Fly Ash, Silica Fume, Slag and Natural Pozzolans in Concrete, Istanbul, Turkey. ACI Special Publication 132, 987–996.

[34] Hooton, R.D., Titherington, M.P, (2004): Chloride resistance of high-performance concretes subjected to accelerated curing. Cem. Concr. Res. 34(9), 1561–1567.

[35] Yazıcı, H., (2008): The effect of silica fume and high-volume Class C fly ash on mechanical properties, chloride penetration and freeze–thaw resistance of self-compacting concrete. Construct. Build. Mater. 22(4), 456–462.

[36] Kostuch, J.A.: Walters, V.: & Jones, T.R., (1993), “High Performance Concretes Incorporating Metakaolin: A Review”, Concrete 2000: *Economic and Durable Concrete through Excellence*, R.K. Dhir: & M.R. Jones, eds., E & FN Spon, London, 1993, pp.1799-1811.

[37] Wild, S.: & Khatib, J.M., (1997), “Portlandite Consumption in Metakaolin Cement Pastes and Mortars”, *Cement and Concrete Research*, Vol. 27, 1997, pp.137-146.

[38] Boddy, A.: Hooton, R. D.: & Gruber, K. A., (2001), "Long-Term Testing of the Chloride Penetration Resistance of Concrete Containing High-Reactivity Metakaolin," *Cement and Concrete Research*, V. 31, 2001, pp. 759-765.

[39] Ding, J., & Li, Z., (2002),"Effects of Metakaolin and Silica Fume on Properties of Concrete," ACI Materials Journal, V. 99, No. 4, July-Aug. pp. 393-398.

[40] Hela, R. Marsalova, J., (2009),” Study of Meta Kaolin Influence on Rheological Properties of Cement Mortars”, *Annual Transaction of the Nordic Rheology Society*, VOL. 17.

[41] Vikas Srivastava et al., (2012),” Metakaolin inclusion: Effect on mechanical properties of concrete”, J. Acad. Indus. Res. Vol. 1(5) October 2012.

[42] Santamarina, J.C. & Fratta, D. (1998). Introduction to Signals and Inverse Problems in Civil Engineering. ASCE Press. Reston, VA. 327 pages

[44] Daigle, M., Fratta, D., & Wang, L. B. (2005). "Ultrasonic and X-ray Tomographic Imaging of Highly Contrasting Inclusions in Concrete Specimens". Geo frontier 2005 conference. Austin, TX.

[45] Garboczi, E. J. (2002). "Three-dimensional Mathematical Analysis of Particle Shape Using X-ray Tomography and Spherical Harmonics: Application to Aggregates Used in Concrete". *Cement and Concrete Research*, Vol. 32, No. 10, pp. 1621-1638.

[46] Jonsson, M., Partl, M.N. & Flisch, A. (2002), "Comparison of Different Compaction Methods Using X-ray Computer Tomography", EMPA Report. 47 Massad et al. 2002

[47] Wang, L. B., Frost, J. D. & Mohammad, L. (2002a), "Three-Dimensional Aggregate Evaluation Using X-ray Tomography Imaging", TRB 2002.

[48] Wang, L. B., Frost, J. D., Voyiadjis, G. & Harman, T. P. (2002b), "Quantification of Damage Parameters Using X-ray Tomography Images". *Journal of Mechanics of Materials*, Vol. 35, pp. 777-790.

[49] Ehrig, K et al, (2011)." Comparison of Crack Detection Methods for Analyzing Damage Processes in Concrete with Computed Tomography". International

Symposium on Digital Industrial Radiology and Computed Tomography, Poster 2.

[50] ASTM C 143/C-143 M, (2000), Standard Test Method for Slump of Hydraulic-Cement Concrete.

[51] American Concrete Institute (ACI).

[52] American Society for Testing and Materials (ASTM).

APPENDICES

Appendix A: Results of AutoCAD models of computed tomography images

(IN ATTACHED CD)

Appendix B: Concrete cores analysis with computed tomography method

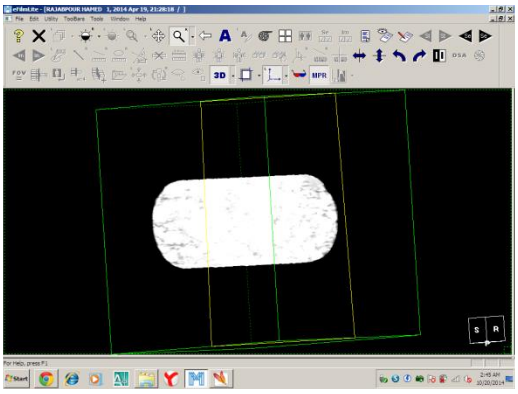
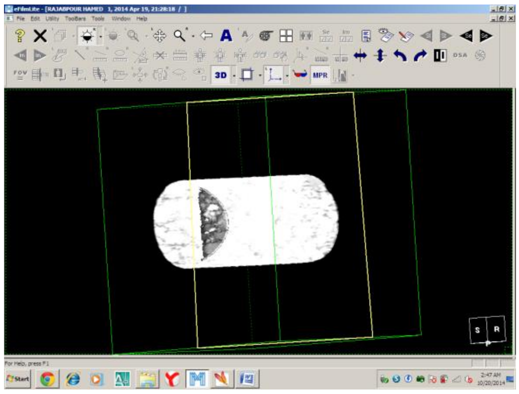
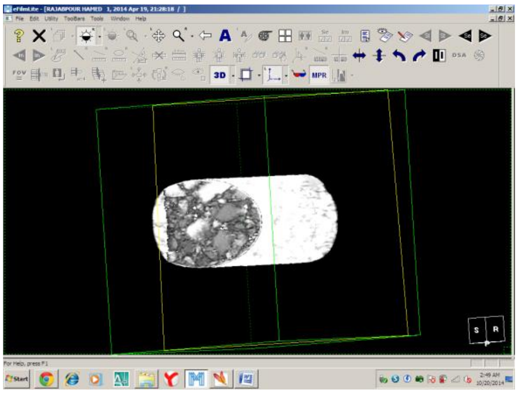
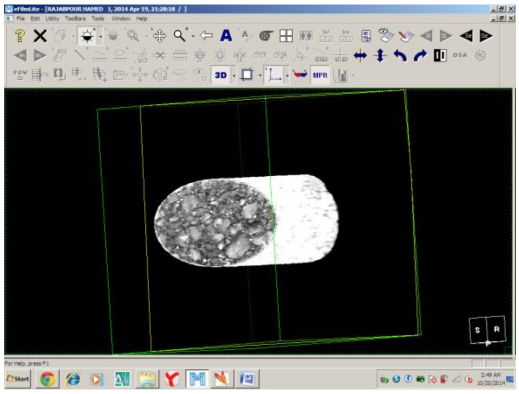
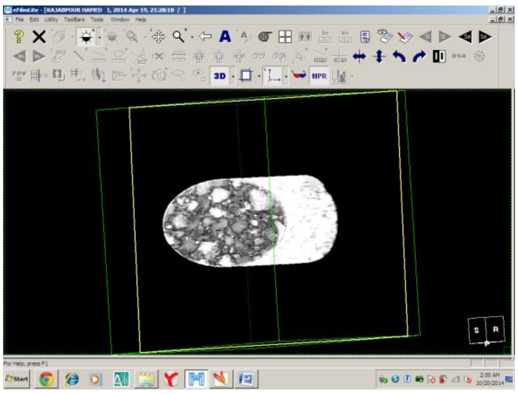
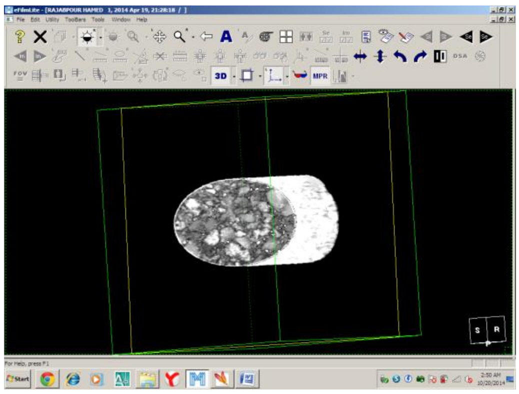
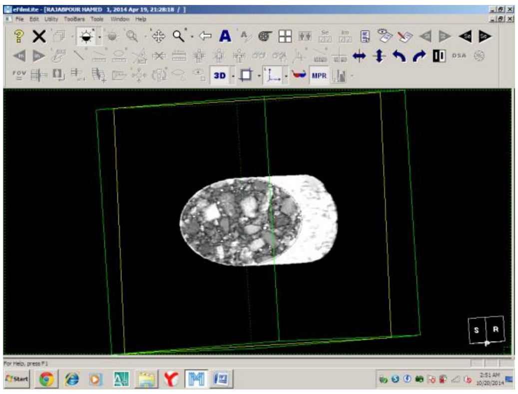
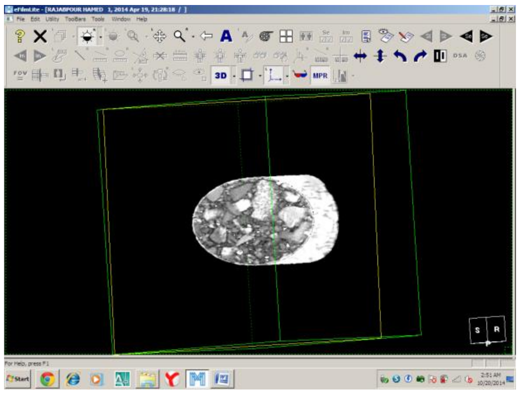

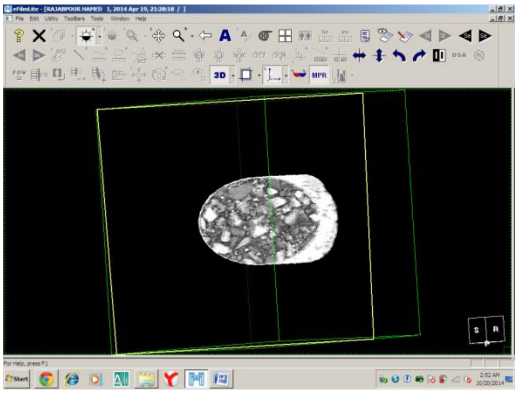

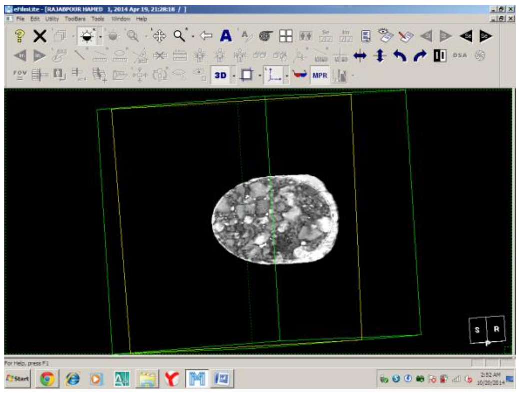

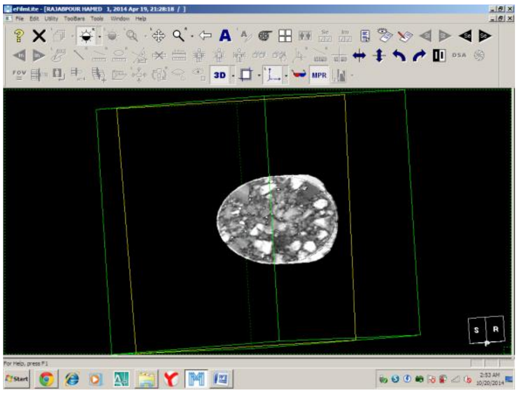

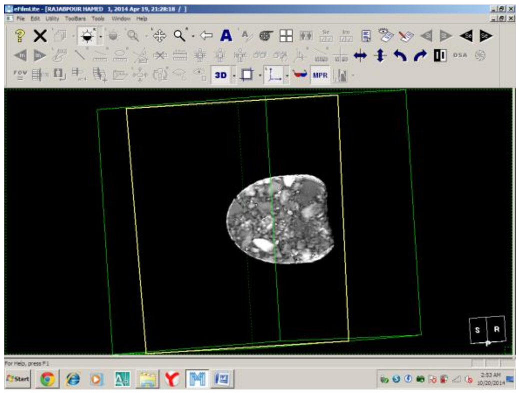

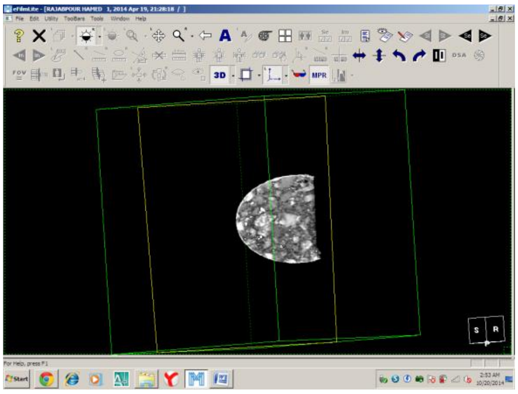

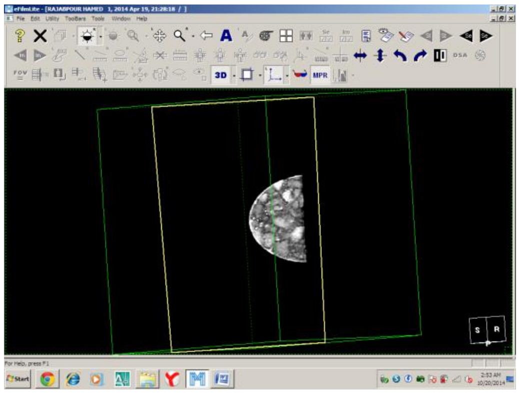

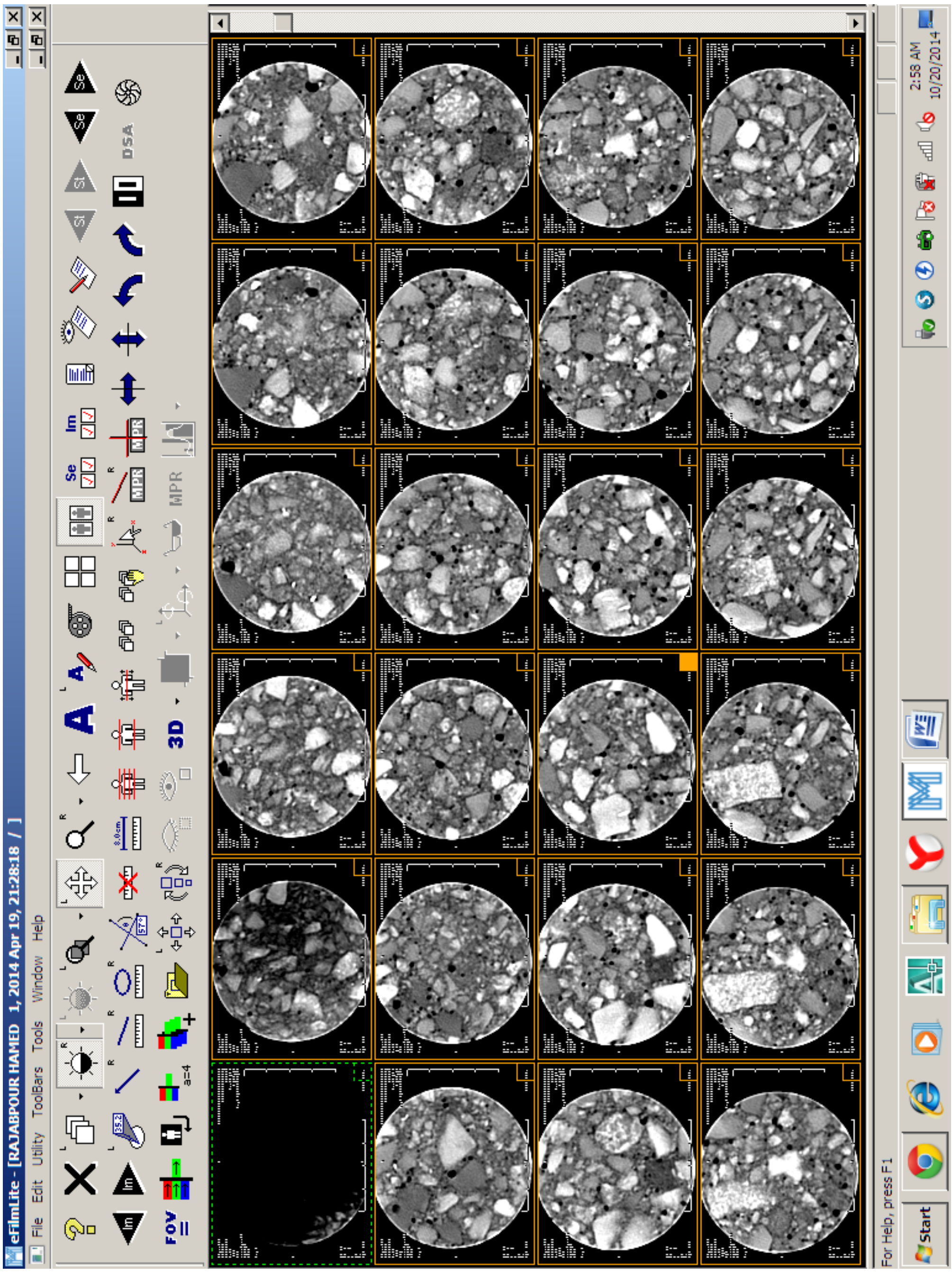
eFilmLite - [RAJABPOUR HAMED 1, 2014 Apr 19, 21:28:18 /]
File Edit Utility ToolBars Tools Window Help
For Help, press F1
Start
2:58 AM
10/20/2014

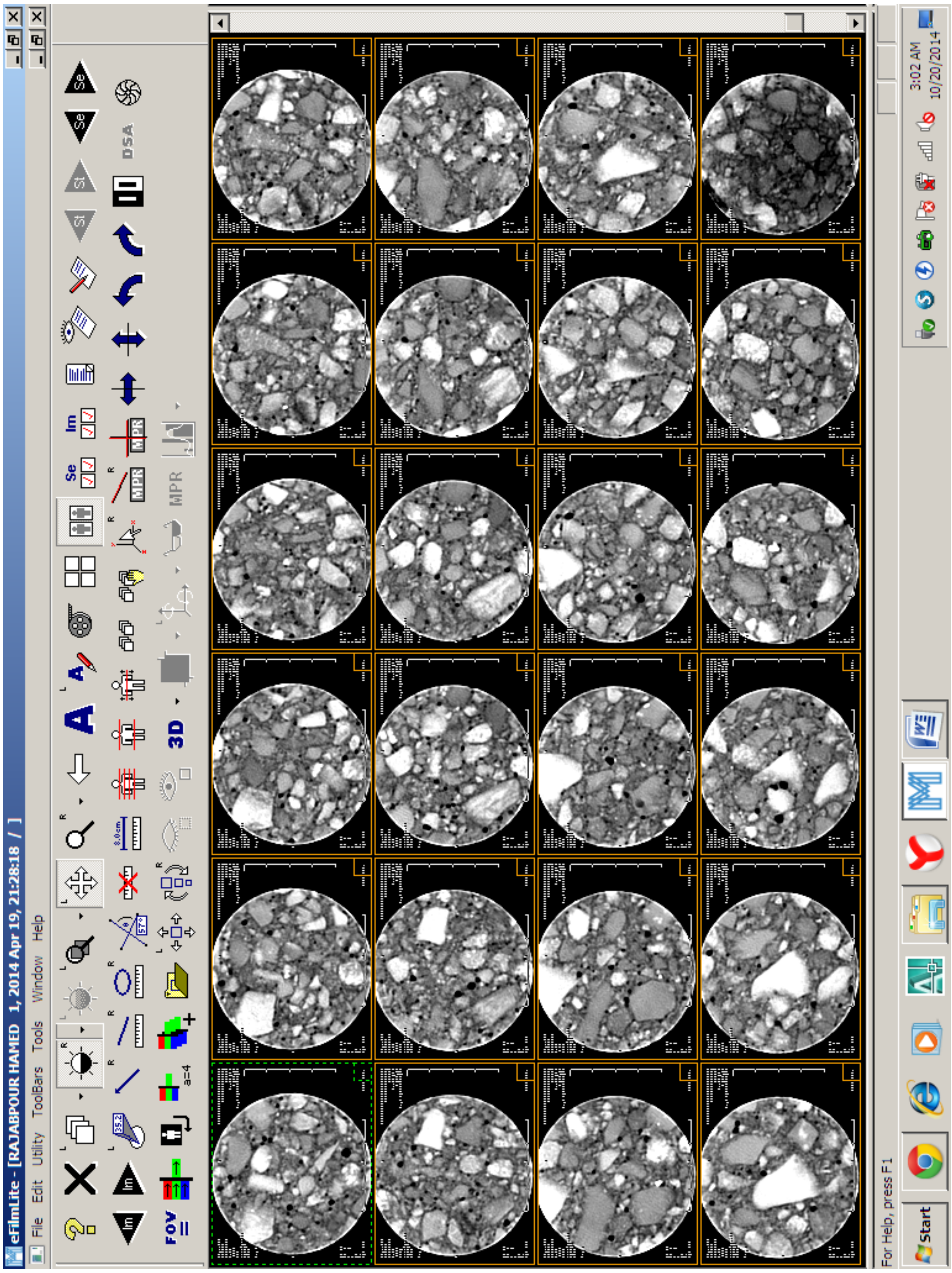
eFilmLite - [RAJABPOUR HAMED 1, 2014 Apr 19, 21:28:18 /]
File Edit Utility ToolBars Tools Window Help
For Help, press F1
Start
3:02 AM
10/20/2014

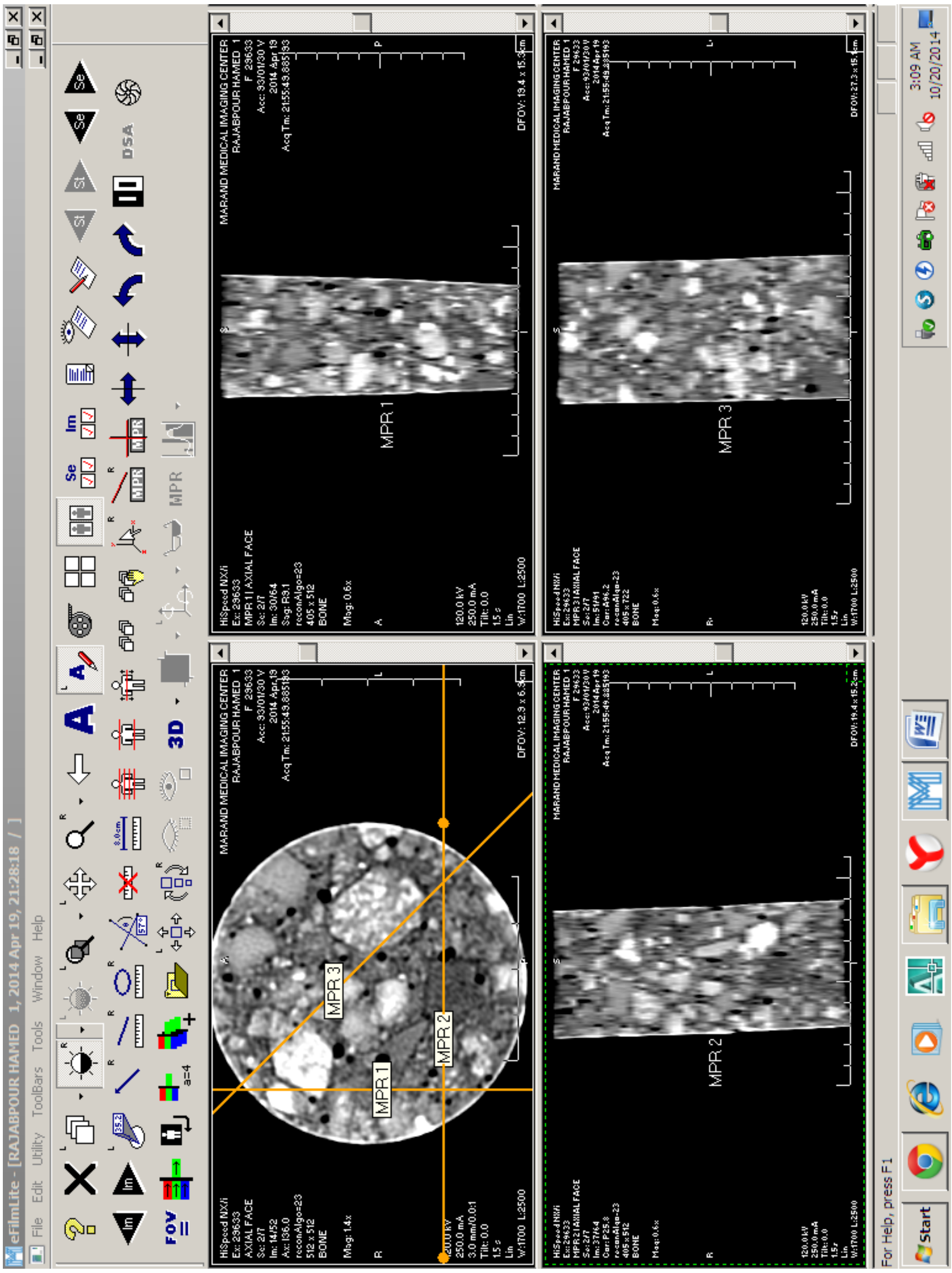
MARAND MEDICAL IMAGING CENTER
RAJABPOUR HAMED 1
MPR 1
MPR 2
MPR 3

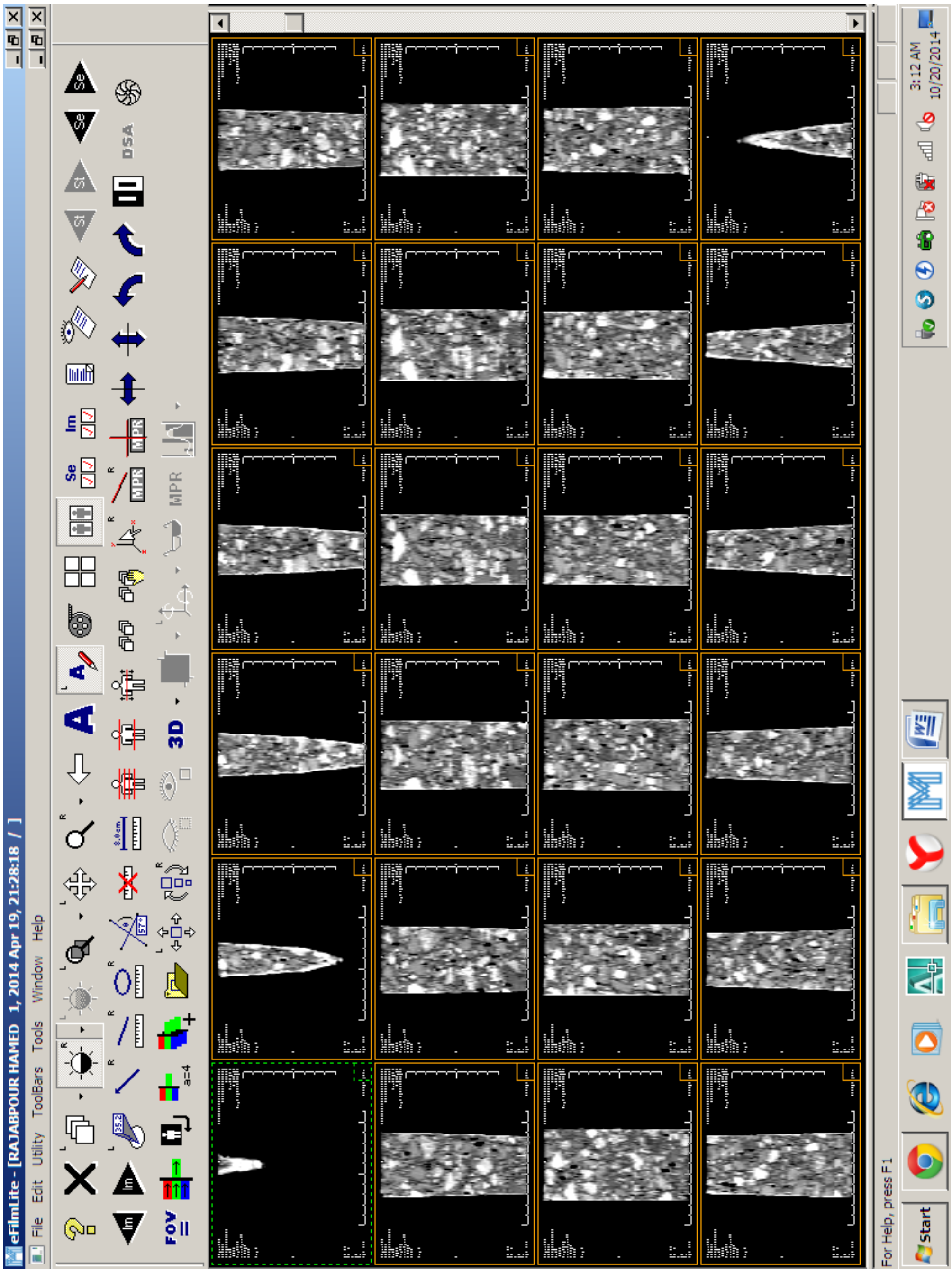
eFilmLite - [RAJABPOUR HAMED 1, 2014 Apr 19, 21:28:18 /]
File Edit Utility ToolBars Tools Window Help
For Help, press F1
Start
3:12 AM
10/20/2014